5-2012

A Study on Small Scale Intermittency Using Direct Numerical Simulation of Turbulence

Saba Almalkie
University of Massachusetts Amherst, salmalki@engin.umass.edu

A STUDY ON SMALL SCALE INTERMITTENCY USING DIRECT NUMERICAL SIMULATION OF TURBULENCE

A Dissertation Presented

by

SABA ALMALKIE

Submitted to the Graduate School of the
University of Massachusetts Amherst in partial fulfillment
of the requirements for the degree of

DOCTOR OF PHILOSOPHY

May 2012

Mechanical and Industrial Engineering

A STUDY ON SMALL SCALE INTERMITTENCY USING DIRECT NUMERICAL SIMULATION OF TURBULENCE

A Dissertation Presented

by

SABA ALMALKIE

Approved as to style and content by:

Stephen M. de Bruyn Kops, Chair

J. Blair Perot, Member

Bruce E. Turkington, Member

Donald L. Fisher, Department Chair
Mechanical and Industrial Engineering

To my parents Azar and Hossein

ACKNOWLEDGMENTS

I would like to express my gratitude to those who directly or indirectly made this work possible. Foremost, I would like to thank my advisor Prof. Stephen de Bruyn Kops for the opportunity to work with and learn from him. I am especially grateful to him for providing a solid foundation for critical thinking, allowing me to explore aspects of my own interest, and for providing me with the support I needed. I would also like to thank Prof. Blair Perot for sharing his knowledge and expertise on the subject and for providing fresh ideas. Thanks to Prof. Bruce Turkington for taking the time to be on my dissertation committee.

I would also like to acknowledge my mentor Prof. William George, who is a fantastic source of inspiration and a role model for deep and fresh thinking. Furthermore, I would like to thank all my colleagues at the CFD lab as well as all my close friends from far and near for their help and friendship. Without their support things would certainly have been more difficult. A special thank you to my labmate Kaustubh Rao for wonderful times in Marston 213 and brilliant discussions.

I am eternally indebted to my fantastic parents and sister for their unconditional love, encouragement, and support. I would like to deeply thank them for being there at each step of my life and for supporting me in every decision that I have made. And finally, thanks to Patrick for his continued love, patience, and support during the writing of this dissertation, for being with me through rough times and sharing with me the good times.

The high performance computer time for this work was provided, in part, by the Office of Naval Research Grant No. N00014-08-1-0236, the U.S. Department of Defense High Performance Computing Modernization Program by the Arctic Region Supercomputing Center, the Army Engineer Research and Development Center, and the Army Research Laboratory.

ABSTRACT

A STUDY ON SMALL SCALE INTERMITTENCY USING DIRECT NUMERICAL SIMULATION OF TURBULENCE

MAY 2012

SABA ALMALKIE

B. Sc., UNIVERSITY OF TEHRAN

M. Sc., CHALMERS UNIVERSITY OF TECHNOLOGY

Ph.D., UNIVERSITY OF MASSACHUSETTS AMHERST

Directed by: Professor Stephen M. de Bruyn Kops

Theory of turbulence at small scales plays a fundamental role in modeling turbulence and in retrieving information from physical measurements of turbulent flows. A systematic methodology based on direct numerical simulations of turbulent flows is developed to investigate universality of small scale turbulence. Understanding characteristics of the small scale intermittency in turbulent flows and the accuracy of the models, measurements, and theories in predicting it are the main objectives. The research is designed to address two central questions; 1) possible effects of large scale anisotropies on the small scale turbulence and 2) potential biases in characterizing small scale turbulence due to the nature of the quantities used to extract the information, known as surrogates. Direct numerical simulations of forced, isotropic homogeneous turbulence with extraordinarily fine spatial resolution on a periodic box

up to $4096 \times 4096 \times 4096$ grid points are analyzed first, to provide a clear insight to the small scale turbulence in the absence of large scale anisotropy. Direct numerical simulations of forced, homogeneous and axisymmetric density stratified flows on a periodic box up to $4096 \times 4096 \times 2048$ grid points with the buoyancy Reynolds number ranging from 10 to 220 are considered next. Different levels of density stratification in the vertical direction cause different levels of large scale anisotropy in the flows. These unique simulations provide a clear picture of turbulent structures over an extensive range of scales. The dissipation rate of turbulent kinetic energy is chosen as the main descriptor of small scale structures. A comprehensive study on surrogates of energy dissipation rate is conducted to identify the best descriptor of the small scale turbulence based on easily measured quantities in physical experiments. In particular, the one-dimensional longitudinal and transverse surrogates, as well as a surrogate based on the asymmetric part of the strain rate tensor, are considered.

The statistical analysis of local and locally averaged energy dissipation rate indicates that the small scale intermittency manifested in the energy dissipation rate is universal with intermittency exponent of $\mu = 0.25 \pm 0.05$, independent of flow conditions and measurement methods. In contrary, the general shape of the probability density functions of energy dissipation rate is strongly skewed to reflect all the existing dynamics in the flow. The surrogates are fundamentally different than the energy dissipation rate. The longitudinal and transverse surrogates overestimate the intermittency exponent by factors of 1.5 and 2.2, respectively. The scale dependency of the moments of locally averaged energy dissipation rate is proposed as a powerful technique to identify the dominant dynamics of the complex flows for a specific range of scales in physical space. Specifically, for the stratified turbulence, this method suggests a superposition of patches of three-dimensional turbulence superimposed on the background semi two-dimensional stratified flow.

TABLE OF CONTENTS

LIST OF TABLES

Table **Page**

LIST OF FIGURES

Figure **Page**

CHAPTER 1

INTRODUCTION

In the words of the legendary physicist Richard Feynman, "Turbulence is the last great unsolved problem of classical physics". In fact similar quotations variously attribute to Horace Lamb, Arnold Sommerfeld, Werner Heisenberg, Albert Einstein, Theodore von Karman or Ludwig Prandtl. The understanding of turbulence is essential in a range of scientific disciplines, from atmospheric and oceanic flows to engineering applications including flows in pipelines, car engines, plane turbines, around ships and air-crafts, to even the human body and the air flow in the lungs. The entire universe appears to be in a state of turbulent motion. A large class of nonlinear dynamic systems including social networking, financial markets, transportation, and Internet can also be viewed as analogous to turbulent flow. Despite all the history and application of turbulent flows in science and technology, a deep understanding of turbulence remains a challenging problem.

Turbulence is an attractive research subject for engineers as well as physicists. The engineering approach focuses on the technological improvements, including modeling and controlling of turbulence, while for the physicists a proper understanding of physics and developing theories to explain turbulence is the main interest. Advancements in turbulence theory mostly rely on the knowledge of the small scale structures, since if there is any "universal" or "quasi-universal" theory for turbulence, it should be related to the small scales. Small scale turbulence has also a significant effect on every day engineering problems and modeling. A deeper knowledge of small scales

improves predictions of large eddy simulations (LES) by developing more realistic sub-grid scale models.

A distinct characteristic of small scale turbulence is its intermittent nature. Note that the term intermittency here refers to the small scale or internal intermittency, which is different than the external intermittency. The external or large scale intermittency usually refers to the patchy nature of turbulent flows that occurs at large scales and is flow specific. Internal intermittency in turbulence, similar to many other nonlinear dynamic systems, generates extreme events that are hundreds to thousands times of the averaged values. The extreme events, e.g., intense hurricanes, huge floods and earthquakes, and big crashes in the stock market, have a drastic and often dominant effect on the system, despite their very low probability of occurrence. The reacting flows, mixing and dispersion problems are the examples of engineering applications where the extreme events have the dominant effect. It is substantial to understand the nature of intermittency and to predict the occurrence of extreme events and the related time scales.

The focus of modern turbulence theory research is on the universality of small scales and intermittency. The classical turbulence theory has been developed assuming statistically isotropic and universal small scale turbulence. It is assumed that the information about the large scales, including anisotropy, is gradually lost as energy moves into smaller scales. Due to the intermittent nature of turbulence, however, the energy transfer to the smaller scales and decay of the large scale anisotropies depend on the geometry of turbulence. As a result, residual anisotropy may persist at small scales contradicting the classical expectations of recovery of isotropy.

The classical agreement on the universal small scale similarity theory has been questioned while a rigorous understanding of small scale turbulence is still undetermined. The recent turbulence theory research (over the past ten years) suggests a possible relationship between the intermittency and residual anisotropy at small

scales. To obtain a better understanding of the small scale turbulence theory and to develop more realistic modeling approaches, it is essential to determine if the residual anisotropy has a dominant effect on small scale turbulence, or if it is just a slight deviation from the isotropic state. Also, it is critical to know if small scale intermittency is universal and if all of the turbulent flows exhibit the same small scale characteristics regardless of flow type, boundary and initial conditions. To approach these questions, we have to quantify small scale intermittency.

The research on small scale turbulence is challenging mainly due to the lack of reliable data at these scales. Generally experimental measurements at large Reynolds numbers, Re, do not provide flow information at sufficiently fine resolution required for the small scale studies. As a result in experimental measurements, the small scale characteristics of turbulence are estimated using easily measured quantities generally knows as surrogates. In other words, our classical knowledge of turbulence theory is built based on these estimations, not the direct measurements. Validity of the surrogates in different turbulent flows, reliability of the surrogates in capturing intermittent structures of turbulence, and consequently, accuracy of the intermittency estimations are still open questions.

The direct numerical simulation of turbulence (DNS) is a powerful tool in the studies of small scale theory. It is quite plausible to obtain information on the dynamics of intermittent events in turbulence compared with other non-linear dynamic systems, due to the availability of the governing equations and numerical solutions of these equations. When properly done, DNS provides a full description of the turbulent flow with very fine temporal and spatial resolution. As a result, direct measurements of the small scale intermittency and the estimations using surrogates are available. The caveats are that the DNS must be computed using an accurate numerical method, at high enough Re so that intermittency is pronounced, and with a sufficiently fine numerical grid so that the intermittency is resolved.

In this dissertation, we apply DNS of turbulent flows to address universality of small scale turbulence. The objectives of this dissertation can be summarized in three main questions:

- What are the characteristics of small scale turbulence?
- Are these characteristics universal or flow dependent?
- How one can retrieve and model small scale information using commonly measurable quantities?

We designed a systematic methodology to address these questions comprehensively using DNSs of turbulent flows. Energy dissipation rate is applied as the main descriptor of the small scale turbulence structures. The DNSs are developed specifically for small scale studies with very high small scale resolutions and with very large dynamic ranges. The DNSs of two flow regimes, isotropic homogeneous turbulence and stably stratified turbulence, are chosen. Density stratified turbulence is selected as a simple flow with dominant large scale anisotropies. The unique data sets, which are among the world's largest available simulations, are analyzed throughly to investigate the quality of the simulated data and validity of the classical models. To examine fundamental characteristics of small scale turbulence, we start our analysis with the DNS of isotropic homogeneous turbulence. The DNSs over a range of Re are applied to investigate qualitative and quantitative characteristics of small scale turbulence, scale dependency, and intermittency in the absence of the large scale anisotropies. The capability of the surrogates in estimating small scale characteristics, and consequently effects of turbulence geometry on the small scale statistics, are also considered. Finally to address universality of the small scale turbulence and to investigate the effects of large scale anisotropies on the small scale turbulence, the DNS of density stratified turbulence with different levels of stratification is analyzed. The small scale statistics

including intermittency and their scale dependency are extracted from the DNS data and compared with those of isotropic homogeneous turbulence.

The dissertation is organized as follows. A review on turbulence theory with the emphasis on small scale intermittency is presented in the next chapter. It begins with a brief review on the classical turbulence theory based on Kolmogorov's 1941 similarity hypothesis (K41) and its shortcomings in explaining intermittency. It continues with qualitative and quantitative description of intermittency and Kolmogorov's 1962 refined similarity hypothesis (K62). The third chapter provides a theoretical framework on small scale measurements in turbulent flows. The potential issues in intermittency measurements are identified, a comprehensive approach and a systematic methodology to address them are discussed. The high resolution DNSs and general characteristics of homogeneous isotropic turbulence is discussed in chapter four. The detailed results and discussions of the small scale intermittency in homogeneous isotropic flows and reliability of the surrogates in estimating these statistics are covered in chapter five. The DNSs of strongly stratified turbulence are introduced in chapter six, followed by the small scale statistic and intermittency measurements in chapter seven. The last chapter provides a summary of the research work and presents some of the important conclusions.

CHAPTER 2

THEORETICAL BACKGROUND ON SMALL-SCALE TURBULENCE AND INTERMITTENCY

2.1 Classical Turbulence Theory: Kolmogorov's Similarity Hypothesis

Kolmogorov's similarity hypothesis, inspired by Richardson's energy cascade idea [Richardson, 1922], is a milestone of the classical turbulence theory. The idea of energy cascade indicates that turbulent kinetic energy is produced at the largest scales of motion and is transferred to the smaller and smaller scales, and finally is dissipated at the smallest scales of motion by the viscous effects. In this approach, it is assumed that the energy dissipation rate is determined by the transfer rate of energy from the largest eddies. Kolmogorov further assumed that at sufficiently high Re, small scale turbulence is statistically isotropic and has a universal form. In other words, he assumed all the information about the large scales including anisotropy is gradually lost as energy moves into the smaller scales.

Kolmogorov [1941] developed the similarity hypothesis by defining different length and time scales for the turbulent motion at sufficiently high Re. The length range is divided into two main subranges. The large scale motion or the energy containing range is a strong function of boundary and initial conditions. On the other hand, the so-called equilibrium range, which consists of the dissipation (small length scales) and the inertial ranges (the length scales in between small and large scales), is assumed to be universal and only a function of kinematic viscosity and energy dissipation rate. In the inertial range, the turbulent motion further assumed to be a function of energy

dissipation rate only. K41, through dimensional analysis, implies universal power law scaling for the velocity structure functions and energy spectra in the equilibrium range. We discuss the scaling laws briefly in this section. For more detailed discussion on Kolmogorov's similarity theory see e.g. Frisch [1995], Monin and Yaglom [1975], Pope [2000], Tennekes and Lumley [1972].

The nth-order structure function of the velocity increment, $\Delta_r u_i = u_i(\boldsymbol{x} + \boldsymbol{r}) - u_i(\boldsymbol{x})$, is defined as:

$$\begin{aligned} D_i^n(r) &\equiv \langle \Delta_r^n u_i \rangle \\ &= \int_{-\infty}^{\infty} \mathcal{P}(\Delta_r u_i) \Delta_r^n u_i \, d(\Delta_r u), \end{aligned} \tag{2.1}$$

where $\mathcal{P}(\Delta_r u)$ is the probability density function of velocity increment, $\boldsymbol{x}$ is the position vector, and $\boldsymbol{r}$ is the separation vector with magnitude r. The structure functions with separation vector, $\boldsymbol{r}$, coinciding with the direction of velocity component, u_i, is known as longitudinal while the structure functions with $\boldsymbol{r}$ perpendicular to u_i known as transverse structure functions. We denote the longitudinal and transverse components by the subscripts L and N, respectively. Hence, our notation, e.g., for the third-order longitudinal velocity structure function is $D_L^3(r)$. K41 implies statistical isotropy and consequently similar inertial range scaling for the transverse and longitudinal structure functions as below:

$$D_i^n(r) = C_i^n (\bar{\epsilon} r)^{n/3}, \tag{2.2}$$

where C_i^n is a universal constant and $\bar{\epsilon} = \langle \epsilon_0 \rangle$ is the averaged turbulent kinetic energy dissipation rate. Note that instantaneous energy dissipation rate ϵ_0, is defined as bellow:

$$\begin{aligned} \epsilon_0 &\equiv 2\nu s_{ij} s_{ij} \\ &= \frac{\nu}{2}\left(\frac{\partial u_i}{\partial x_j} + \frac{\partial u_j}{\partial x_i}\right)^2, \end{aligned} \tag{2.3}$$

with ν being the kinematic viscosity. Among the structure functions, the second- and third-order longitudinal structure functions are the commonly used tools for the data analysis in turbulent flows. Kolmogorov's scaling for the third-order longitudinal structure function, known as 4/5 law, has a simple linear form:

$$D_L^3(r) = \frac{4}{5}\bar{\epsilon} r. \tag{2.4}$$

Consistent with the second-order longitudinal and transverse structure functions, one can define the longitudinal, $E_{11}(\kappa_1)$, and transverse, $E_{22}(\kappa_1)$, one-dimensional energy spectra. As is commonly done, we define one-dimensional spectra as one-sided such that the variance of the respective velocity component can be written as an integral over wave numbers ranging from 0 to ∞. A more general form of spectra, the three-dimensional energy spectrum $E(\kappa)$, is defined by integrating the two point correlation tensor $\Phi_{ii}(\boldsymbol{\kappa})$, over a spherical shell of radius κ [Tennekes and Lumley, 1972] :

$$E(\kappa) = \frac{1}{2}\oint \Phi_{ii}(\boldsymbol{\kappa})\, d\sigma. \tag{2.5}$$

$d\sigma$ is the surface element of the shell and the spectrum tensor Φ_{ij}, the Fourier transform of the two point velocity correlation tensor, is given by:

$$\Phi_{ij}(\boldsymbol{\kappa}) = \int\int\int_{-\infty}^{\infty} e^{-i\boldsymbol{\kappa}\cdot\boldsymbol{r}} \langle u_i(\boldsymbol{x}+\boldsymbol{r}, t) u_j(\boldsymbol{x}, t)\rangle \, d\boldsymbol{r}. \tag{2.6}$$

$\boldsymbol{\kappa} = (\kappa_1, \kappa_2, \kappa_3)$ is the three-dimensional wave number vector with magnitude of κ. K41 implies universal inertial range scaling for the so-called Kolmogorov spectrum functions which are defined as:

$$\phi(\eta\kappa) = \frac{E(\kappa)}{u_\eta^2 \eta} \ , \tag{2.7a}$$

$$\phi_1(\eta\kappa_1) = \frac{E_{11}(\kappa_1)}{u_\eta^2 \eta} \ , \tag{2.7b}$$

$$\phi_2(\eta\kappa_1) = \frac{E_{22}(\kappa_1)}{u_\eta^2 \eta} \ . \tag{2.7c}$$

The inertial scaling for the above functions first obtained by Obukhov [1941a,b] are:

$$\phi(\eta\kappa) = \alpha(\eta\kappa)^{-5/3}, \tag{2.8a}$$

$$\phi_1(\eta\kappa_1) = \alpha_1(\eta\kappa_1)^{-5/3}, \tag{2.8b}$$

$$\phi_2(\eta\kappa_1) = \alpha_2(\eta\kappa_1)^{-5/3}. \tag{2.8c}$$

Provided that the turbulence is perfectly isotropic with infinitely large Re, α, α_1 and α_2 are related by [Monin and Yaglom, 1975, Volume II, p. 355]

$$\alpha = \frac{55}{18}\alpha_1 = \frac{55}{24}\alpha_2 \ . \tag{2.9}$$

There is a good agreement between the existing experimental data and the numerical simulations that Kolmogorov's universal constant in the inertial range of high Re flows, is a constant with value $\alpha \approx 1.5 \pm 15\%$, hence, $\alpha_1 = 0.5 \pm 15\%$, $\alpha_2 = 0.67 \pm 15\%$. Thus, Kolmogorov's constant in terms of the second-order longitudinal structure function is $C_L^2 = \alpha/0.76 = 2.0 \pm 0.15\%$ [Sreenivasan, 1995]. Note that η and u_η in the above definitions are the Kolmogorov length and velocity scales characterizing small or dissipative scales of turbulence and are defined by:

$$\eta \equiv \left(\frac{\nu^3}{\bar{\epsilon}}\right)^{1/4}, \tag{2.10}$$

and

$$u_\eta \equiv (\bar{\epsilon}\nu)^{1/4}. \tag{2.11}$$

The characteristic length scales for the energy containing scales, integral length scale ℓ, and for the inertial scales, Taylor micro-scale λ, are defined as:

$$\ell \equiv \frac{3\pi}{4\bar{k}} \int_0^\infty \frac{E(\kappa)}{\kappa}\, d\kappa, \tag{2.12}$$

and,

$$\lambda \equiv \left(\frac{10\nu\bar{k}}{\bar{\epsilon}} \right)^{1/2}. \tag{2.13}$$

$\bar{k} = \langle u_i u_i \rangle / 2$ represents total kinetic energy.

2.2 Small Scale Intermittency: Criticism to Similarity Hypothesis

Kolmogorov's hypothesis suggests a self-similar behavior for the turbulence at equilibrium scales. The term "self-similar" is often ambiguous, confusing, and misleading. Here it refers to the "statistical self-similarity", where the self similarity is not visually obvious but there are statistical measures that are preserved across the scales. Figure 2.1 is an example for a self-similar random signal where the statistical properties of the signal is constant as one zooms in. As a result, some statistics, including normalized centered moments, are constant over the scales of similarity. On the contrary, studies show that statistical properties of the small scale turbulence strongly depend on the flow type and the scales for which the statistics were calculated.

Violation of similarity theory is studied in terms of turbulence intermittency. The small scale intermittency studies were originated from Landau's objection to the Kolmogorov's theory [see e.g. Frisch, 1995, Kraichnan, 1974] by pointing out the large scale dependency of the averaged small scale quantities (energy dissipation rate). The first experimental result exhibiting small scale intermittency was reported by Batchelor and Townsend [1949]. They showed that the derivative of a turbulent signal

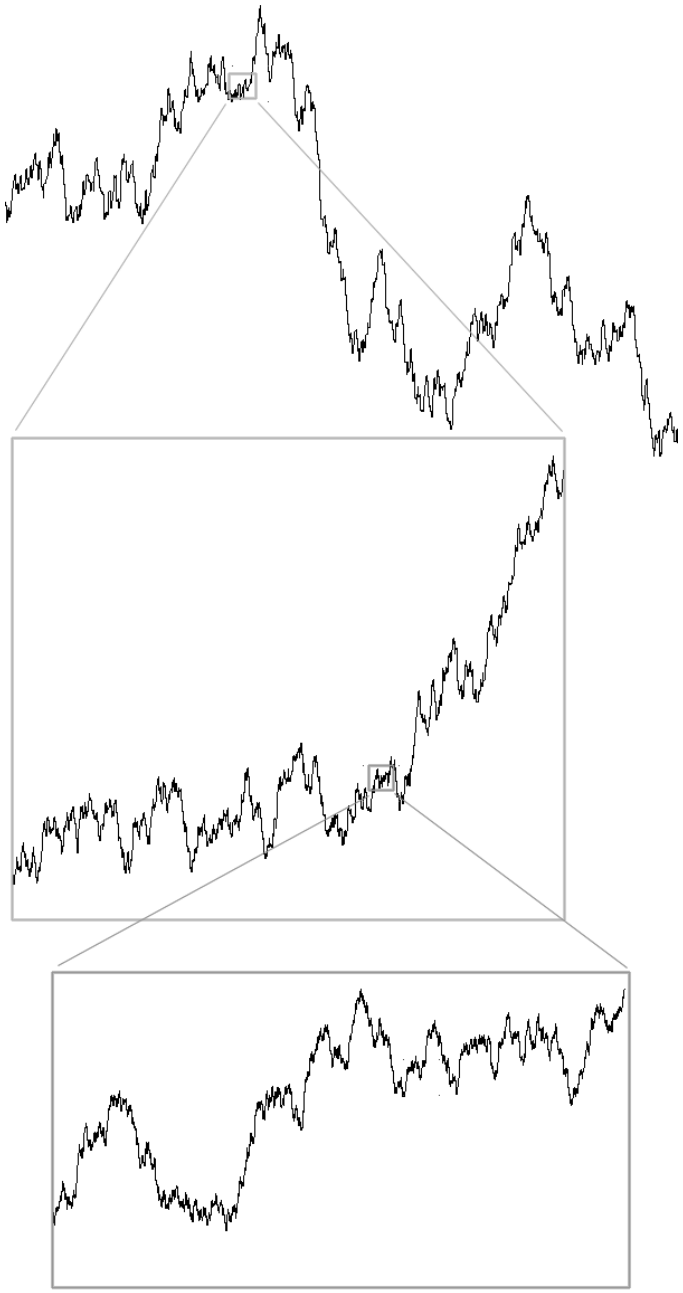

Figure 2.1: A sample of statistically self-similar random variable. The pattern of the fluctuation are similar within insets.

is rather a bursty and intermittent signal and the degree of intermittency increases by increasing the order of differentiation. Kuo and Corrsin [1971] obtained similar results by band-pass filtering a turbulent signal.

The first analytical explanation for the small scale intermittency was made by Kraichnan [1967] by showing that in turbulent flows independent of Re, a very small subset of flow (corresponding to the intermittent events) represents the majority of the small scale energy. Following this method, Frisch and Morf [1981] developed the first systematic explanation of small scale intermittency by discussing the intermittent nature of different nonlinear dynamic systems and relating the intermittent regions to the singularities of the system. In the case of the Navier-Stokes equations, obtaining information about the nature and location of the singularities is the main issue. The above discussion suggests that the small scale intermittency is not limited to the turbulence and fluid mechanics. It occurs in a large class of nonlinear dynamical systems including social networking, economics, transportation, and the Internet.

The significant progress in investigating the kinematics and dynamics of the intermittent turbulent structures was made by developing the numerical simulations of turbulent flow and the advancement in available computational power. The numerical studies of the small scales reveal a picture of the coherent structures down to the Kolmogorov scale. The most accepted geometrical structure is the so-called vortex filaments also known as worms [Frisch, 1995, Saffman, 1992, Sreenivasan and Antonia, 1997].

Vortex filaments are very slender regions of high vorticity and low dissipation and thus regions of low pressure. The filaments are tubes with an approximately circular cross-section with a diameter in the scales of Kolmogorov length scale and with the length between the Taylor micro scale and the integral scale [Brachet, 1991, Brachet et al., 1983, Douady et al., 1991, She et al., 1990, Siggia, 1981a]. The formation of these structures has not been understood completely. It is mostly believed that these

structures are formed whenever shearing and stretching of a thin layer happens by the large scales or near solid boundaries. In other words, these structures are generated as a result of small scale anisotropy in the flow. Vortex filaments connect large eddies of much weaker vorticity and are strongly effected by the stresses and strains generated by these large eddies. It is commonly believed that intermittency occurs as a result of stretching and compressing of vortex filaments. Similarly, Mahrt [1989], Holzer and Siggia [1994] and Warhaft [2000] suggested that intermittency occurs in a very narrow zone of concentrated shear or the so-called micro-fronts, which are considered as the edges of the large coherent structure vortex sheets, hence related to the large turbulent eddies.

2.3 Quantifying Intermittency

Existence of the small scale intermittency has been accepted widely by the turbulence community, but there are still uncertainties and conflicts in defining and quantifying intermittency. Flow properties do not fluctuate uniformly in intermittent flows. Therefore, the average of the flow properties on small volumes are random functions of time and space. Fluctuations of the locally averaged properties increase drastically by diminishing the size of the averaging volume. The scale dependency of these quantities deviates from the dimensional scaling suggested by K41. This deviation, generally known as anomalous scaling, is the common method of quantifying intermittency. Some studies [e.g. Boettcher et al., 2003, Sreenivasan, 1999] choose to apply scale dependency of the probability density functions of the locally averaged variables to quantify intermittency. Nevertheless, anomalous scaling of higher order statistics like energy dissipation rate and velocity structure functions are generally preferred. Among the scaling exponents, the so-called intermittency exponent, characterizing the second-order behavior of the locally averaged energy dissipation rate, is the most basic and popular variable.

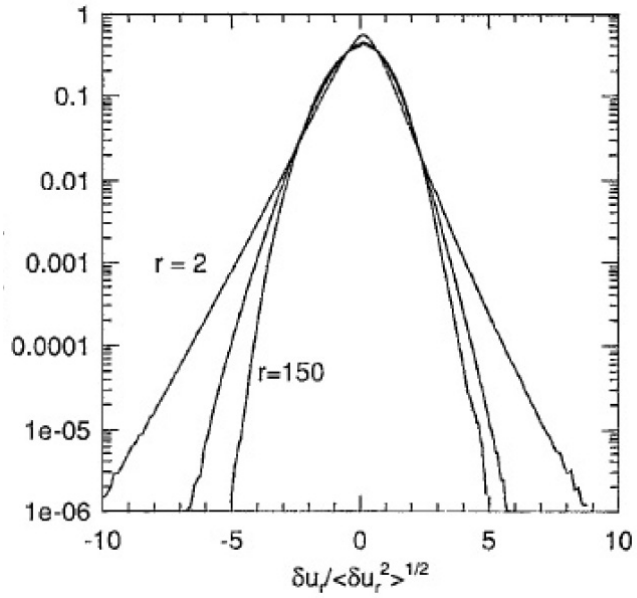

Figure 2.2: Probability density function of normalized velocity increments $\Delta_r u$ for different separation distances r with $\ell = 512$ as the integral length scale (taken from Chen et al. [1993]).

Turbulence intermittency occurs in the inertial range as well as dissipation range. Figure 2.2 shows the probability density function of the velocity increment for a range of separation distances r. The tails of the curves are heavier for smaller r but even for the r in the inertial range, the probability density function deviates from the Gaussian distribution, considerably. The anomalous scaling method can be used for quantifying intermittency in both dissipation and inertial ranges. The dissipation range intermittency is usually quantified in terms of velocity derivatives or energy dissipation rate while for the inertial range, the high-order structure functions of the velocity increments are preferred. In complex flows, where turbulence is generated as a result of non-isotropic mechanisms, for example shear, stratification, and rotation, the scales of intermittency affects structure functions. In such cases the normalized centered or dimensionless structure functions are the better options for studying intermittency.

2.4 Refined Similarity Hypothesis

Kolmogorov's refined similarity hypothesis (K62) is the first and most well-established mathematical model for intermittency [Kolmogorov, 1962, Obukhov, 1962]. This hypothesis links the anomalous scaling of the energy dissipation rate to the structure functions. According to K62, the statistics of the longitudinal velocity increments, $\Delta_r u$, conditioned on the locally averaged energy dissipation rate, ϵ_r, are universal. Thus, the structure function, which is the unconditional mean, can be obtained as [Pope, 2000, Sreenivasan and Antonia, 1997]:

$$\begin{aligned} D_L^n(r) &\equiv \langle \Delta_r^n u \rangle \\ &= \langle \langle \Delta_r^n u | \epsilon_r \rangle \rangle \\ &= C_R^n \langle \epsilon_r^{n/3} \rangle r^{n/3}, \end{aligned} \tag{2.14}$$

where C_R^n is a universal constant. The so-called locally averaged energy dissipation rate, ϵ_r, is defined as the average of instantaneous energy dissipation rate on a volume with linear dimension r ($\eta \ll r \ll \ell$):

$$\epsilon_r(\boldsymbol{x}, t) = \frac{1}{V} \int\int\int_{V(r)} \epsilon_0(\boldsymbol{x} + \boldsymbol{r}, t)\, d\boldsymbol{r}. \tag{2.15}$$

ϵ_r is a fluctuating quantity and it's statistics depend on the averaging volume size r. Kolmogorov [1962], and more specifically Novikov and Stewart [1964], postulated a scaling form as below for the higher-order moments of ϵ_r in the inertial range:

$$\langle \epsilon_r^n \rangle \sim r^{\tau(n)}, \tag{2.16}$$

where $\tau(n)$ is a universal function. $\tau(2) = \mu$ is defined as the intermittency exponent. Similar to K41, a power law can be obtained for the higher-order moments of the longitudinal velocity increments in the inertial range as below:

$$D_L^n(r) = A_n r^{\zeta_n}, \tag{2.17}$$

where A_n is a non-universal coefficient, which is a function of large scales and ζ_n is a universal exponent. By substituting Eqs.(2.16) and (2.17) in Eq.(2.14) we can write ζ_n in terms of τ as below:

$$\zeta(n) = \frac{n}{3} + \tau\left(\frac{n}{3}\right). \tag{2.18}$$

Kolmogorov [1962] and Obukhov [1962] explicitly suggested a lognormal distribution for ϵ_r, *i.e.,* a normal distribution for $\log(\epsilon_r/\bar{\epsilon})$. Under this assumption, the inertial range scaling of the higher-order moments of ϵ_r is as below:

$$\langle \epsilon_r^n \rangle \sim r^{n(1-n)\mu/2}. \tag{2.19}$$

This model further implies that the variance of the logarithm of locally averaged energy dissipation rate, $\sigma^2_{\log \epsilon_r}$, decreases linearly with logarithm of averaging volume size:

$$\sigma^2_{\log \epsilon_r} = A - \mu \log r. \tag{2.20}$$

Similar to Eq.(2.18), the scaling exponent for the nth-order structure function can be linked to the intermittency exponent assuming lognormal model as below:

$$\zeta_n = \frac{1}{3}n - \frac{1}{18}\mu n(n-3). \tag{2.21}$$

The validity of the refined similarity hypothesis in predicting intermittency of turbulent flow is still an open question. This model is reviewed by Frisch [1995] and its shortcomings have been discussed [Kraichnan, 1974, Mandelbrot, 1974, Schertzer et al., 1997].The degree of intermittency predicted by this model often underestimates the experimental measurements, especially at smaller scales. The so-called multifractal models (e.g. β-model) predict better matching results with the experiments for

the dissipation range intermittency [Frisch, 1995, Frisch et al., 1987, Meneveau and Sreenivasan, 1991]. Note that obtaining reliable measurements of intermittency is the main challenge in evaluating intermittency models, which is discussed in the following section.

CHAPTER 3

METHODICAL APPROACHES TO ISSUES IN QUANTIFYING SMALL-SCALE INTERMITTENCY

This chapter provides a theoretical framework on the issues in quantifying small scale characteristics of turbulence including intermittency, and presents a methodology to approach these issues. The focus is on estimation of small scale characteristics using surrogates of energy dissipation rate, and the dependency of these estimations on the geometry of turbulence and large scale anisotropies. It starts with an overview on energy dissipation measurements. In section two, precise definitions of commonly used surrogates are presented and underlying assumptions and simplifications are investigated. Various methods of extracting the intermittency exponent are discussed in section three. The potential effects of large scale anisotropy on intermittent small scales are covered in section four. In the last section, the DNS of turbulence is suggested as a powerful tool for small scale studies. The quality of DNS data required for such studies is discussed.

3.1 Energy Dissipation Rate and Quantifying Intermittency

The brief review of small scale turbulence theory in the previous chapter introduces the energy dissipation rate as the key descriptor of structures of small scale turbulence. Intermittency, a fundamental characteristics of small scale turbulence, is also manifested in the energy dissipation rate. One of the major advantages of the energy dissipation rate in small scale studies, is its volumetric nature. The direction independency of energy dissipation rate, minimizes its dependency to the turbulence

geometry and consequently to the small scale anisotropies. Note that energy dissipation rate is defined as a summation of multiple directional components and has a comprehensive effect. The scale dependency of small scale characteristics, including intermittency, can be investigated in terms of locally averaged energy dissipation rate over a range of scales from deep in the dissipation range up to outer inertial range. The two main theoretical models for the small scale turbulence, *i.e.,* refined similarity and multi-fractal models are both developed based on the locally averaged energy dissipation rate. These models suggest universal characteristics for small scale turbulence including intermittency.

Universality of the small scale intermittency manifested in the anomalous scaling exponents of the energy dissipation rate is an ongoing research topic. There have been many attempts to obtain the universal numerical values for the scaling exponents using numerical and physical experiments. The reported results exhibit some qualitative agreement while significant quantitative differences exist. For example, there is a considerable uncertainty in the numerical values reported for the intermittency exponent μ. This exponent is reported in a range between 0.1 to 0.7 depending on the flow type and measurement technique [see e.g. Cleve et al., 2004, Frehlich et al., 2004, Kurien et al., 2000, Monin and Yaglom, 1975, Muschinski et al., 2004, Praskovsky and Oncley, 1997, Sreenivasan and Kailasnath, 1993, Vindel et al., 2008]. Note that generally in small scale measurements, the sensitivity of the results to the measurement methods and to the initial conditions and large scale anisotropies are not considered. These two main issues in small scale measurements are discussed in this chapter.

Despite all the advantages of the energy dissipation rate in the small scale and intermittency studies, measuring energy dissipation rate is a challenging subject in physical experiments and requires simultaneous multi-point measurements of the flow field with a very high resolution. In the majority of the physical experiments including

geophysical flow measurements, the data gathering is made by stationary probes as time series over a long time period (long compared with the turbulence time scales). Thus, flow information is available only in one direction, *i.e.,* the mean velocity or stream-wise direction. Calculating energy dissipation rate and other intermittency related statistics from the time-series of experimental measurements creates several major issues.

Firstly, all the spatial statistics are estimated from the temporal data series. The most common assumption for inferring spatial statistics from the temporal data is Taylor's frozen turbulence hypothesis [Taylor, 1938] or the local version known as the random Taylor hypothesis [Hinze, 1975, Pope, 2000, Tennekes, 1975, Tennekes and Lumley, 1972]. It has been suggested that the turbulence time series are more intermittent compared with the spatial series. This is not the topic of interest in this dissertation and for a detailed discussion on this subject and the differences between the Lagrangian and Eulerian statistics the reader is referred to Benzi et al. [2010], Berg et al. [2009], Biferale et al. [2008a], Gulitski et al. [2007a], Ishihara et al. [2007], Tsinober et al. [2001], Yeung and Pope [1989], Yeung et al. [2006a], Yoshimatsu et al. [2009]. Additionally, since the three-dimensional data are not available, all three-dimensional statistics are replaced by the one-dimensional equivalents known as surrogates under some major assumptions and simplifications. In particular, understanding of energy dissipation rate is based largely on studies of longitudinal velocity gradients [e.g. Benzi et al., 1991, Biferale, 2008, Chen et al., 1993, 1995, Cleve et al., 2004, Meneveau and Sreenivasan, 1991, Schumacher, 2007, Stolovitzky and Sreenivasan, 1994, Stolovitzky et al., 1992, Vainshtein, 2000, Yakhot, 2006]. It is generally known that the surrogates and energy dissipation rate differ [e.g. Bershadskii and Tsinober, 1993, Cleve et al., 2003, Hao et al., 2008, Hosokawa, 1995, Hosokawa et al., 1996, Thoroddsen, 1995, Wang et al., 1996, Zhou and Antonia, 2000a, Zhou et al., 2006], but further study is needed to quantify these differences. In addition, since

intermittency is a fundamental characteristic of turbulence manifested in the dissipation rate, it is important to understand how using surrogates in place of energy dissipation rate may bias our understanding of intermittency.

Accuracy of the intermittency estimations relies on the efficiency of the surrogates in capturing turbulent structures as well as validity of the surrogates at different flow regimes. As discussed in §2.2, the structures responsible for the intermittent behavior of turbulence are 3-D structures known as worms. The surrogates are usually geometry dependent and have different efficiency in capturing these structures. The intermittency exponent is also extracted indirectly via various methods and surrogates depending on the data availability and measurement technique.

Another important factor on accuracy of the intermittency estimations is validity of the surrogates in the presence of anisotropy. Almost all of the practical high *Re* turbulent flows are driven by large scale anisotropies. It is believed that a weak anisotropy remains even at the smallest scales [Biferale and Procaccia, 2005, Biferale and Vergassola, 2001, Biferale et al., 2008b, Casciola et al., 2007, Toschi et al., 1999]. In such situation, the validity of the assumptions inherent in the definition of surrogates is dubious. These two issues are discussed in more detail in the following sections.

3.2 Surrogates of Energy Dissipation Rate

The averaged energy dissipation rate can be decomposed into the isotropic and anisotropic components as below:

$$\begin{aligned}\langle \epsilon_0 \rangle &= \frac{\nu}{2} \left\langle \left(\frac{\partial u_i}{\partial x_j} + \frac{\partial u_j}{\partial x_i} \right)^2 \right\rangle \\ &= \nu \left\langle \left(\frac{\partial u_i}{\partial x_j} \right)^2 \right\rangle + \nu \left\langle \frac{\partial u_i}{\partial x_j} \frac{\partial u_j}{\partial x_i} \right\rangle . \end{aligned} \tag{3.1}$$

The first term known as the pseudo-dissipation is the isotropic component, which consists of longitudinal and transverse velocity gradients. Note that the terms longitudinal and transverse refer to the velocity gradients parallel and orthogonal to the velocity component, respectively. In isotropic turbulence, the second term, which represents the anisotropic component, is zero. In almost all circumstances this term is very small compared with the isotropic term [Pope, 2000]. In addition to the longitudinal gradients, the anisotropic component includes an extra term known as asymmetric component. This component is a combination of non-equal transverse gradients and represents anisotropy effects. Therefore, the longitudinal, transverse, and asymmetric components are the three main building blocks of the energy dissipation rate. Instantaneous energy dissipation rate (Eq.2.3) can also be written in terms of the three main components as:

$$\epsilon_0 = \nu \left[2 \left(\frac{\partial u_i}{\partial x_i} \right)^2 + \left(\frac{\partial u_i}{\partial x_j} \right)^2 + \left(\frac{\partial u_i}{\partial x_j} \frac{\partial u_j}{\partial x_i} \right) \right] \quad , \quad i \neq j \ . \tag{3.2}$$

Direct Measurements of ϵ_0 requires the simultaneous acquisition of nine velocity derivatives resolved in spatial scales less than any dynamically-relevant length scale in the flow, and temporally resolved at a correspondingly small time scale. The challenge of making such measurements encourages the consideration of surrogates for ϵ_0 based on a subset of the nine components of the strain rate tensor.

A number of one-dimensional surrogates of instantaneous energy dissipation rate can be defined depending on the data availability. Our approach here is to define the surrogates based on the three main characteristic components of energy dissipation rate. As a result of statistical isotropy, the velocity gradients are independent of the velocity component. Therefore, to simplify the equations, we use $\partial u_1/\partial x_1$, $\partial u_1/\partial x_2$, and $\partial u_1/\partial x_2 \partial u_2/\partial x_1$ as representatives for the longitudinal, transverse, and asymmetric terms, respectively. One can estimate the unknown components of the velocity gradient tensor based on the known components assuming statistical isotropy. By

accounting for the continuity and homogeneity in the flow, one can derive a mathematical relationship between the transverse and asymmetric components and the longitudinal component as below:

$$\left\langle \left(\frac{\partial u_1}{\partial x_2} \right)^2 \right\rangle = 2 \left\langle \left(\frac{\partial u_1}{\partial x_1} \right)^2 \right\rangle, \tag{3.3}$$

and

$$\left\langle \frac{\partial u_1}{\partial x_2} \frac{\partial u_2}{\partial x_1} \right\rangle = -\frac{1}{2} \left\langle \left(\frac{\partial u_1}{\partial x_1} \right)^2 \right\rangle. \tag{3.4}$$

Using these relationships, we define three one-dimensional isotropic surrogates (denoted by the symbol tilde) as below:

$$\tilde{\epsilon}_{0,1} = 15\nu \left(\frac{\partial u_1}{\partial x_1} \right)^2, \tag{3.5}$$

$$\tilde{\epsilon}_{0,2} = \frac{15}{2}\nu \left(\frac{\partial u_1}{\partial x_2} \right)^2, \tag{3.6}$$

and

$$\tilde{\epsilon}_{0,3} = -30\nu \left(\frac{\partial u_1}{\partial x_2} \frac{\partial u_2}{\partial x_1} \right). \tag{3.7}$$

The first two surrogates are natural to consider in the context of measurements of real flows since they involve only one velocity derivative. The third surrogate would not likely be the one of choice when working with laboratory measurements, but it provides information about the effects of anisotropy.

In physical experiments, the energy dissipation rate is commonly substituted by the longitudinal surrogate $\epsilon_{0,1}$ and the majority of the theories and models are developed mainly for this variable [e.g. Benzi et al., 1991, Biferale, 2008, Chen et al., 1993, 1995, Cleve et al., 2004, Meneveau and Sreenivasan, 1991, Schumacher, 2007, Stolovitzky and Sreenivasan, 1994, Stolovitzky et al., 1992, Vainshtein, 2000, Yakhot, 2006]. We can rely on the theories and models only if the statistical characteristics

of the surrogates are identical to those of the energy dissipation rate. By definition, all the surrogates are exact in the mean for perfectly isotropic turbulence. Therefore, the models and theories that are based on the mean energy dissipation rate, for example Kolmogorov's scaling of the third-order structure function (4/5 law), are valid for the surrogates. However, the detailed knowledge of the higher-order statistics of the energy dissipation rate and the surrogates remains an open question, while the potential differences between the probability distributions of ϵ_0 and the longitudinal surrogate have been pointed out by previous studies [e.g. Bershadskii and Tsinober, 1993, Cleve et al., 2003, Hao et al., 2008, Hosokawa, 1995, Hosokawa et al., 1996, Thoroddsen, 1995, Wang et al., 1996, Zhou and Antonia, 2000a, Zhou et al., 2006]. The higher-order statistics of the energy dissipation rate and its surrogates are the key parameters in measuring and modeling intermittency. The surrogates are directional statistics and may reflect turbulence geometry differently. Therefore, estimations of the intermittency based on the surrogates are expected to depend on which surrogate is considered. Various studies have supported this conclusion [Cleve et al., 2003, Hao et al., 2008, Hosokawa et al., 1996, Wang et al., 1996, Zhou et al., 2006].

Intermittency has been quantified using many different approaches. For example, the intermittency exponent, μ, has been defined and measured via different methods in experiments depending on the data availability and measurement technique [Sreenivasan and Kailasnath, 1993]. In addition to the biases in the intermittency estimations due to the nature of the surrogates, the potential biases due to the measurement methods, should also be considered. In the next section some of these methods are discussed.

3.3 Intermittency Exponent

K62 postulated that higher-order moments of ϵ_r are universal in the inertial range($\eta \ll r \ll \ell$):

$$\langle \epsilon_r^n \rangle \sim r^{\tau(n)} \tag{3.8}$$

The second-order power $\tau(2) = \mu$ is known as the intermittency exponent and is the primary measure of intermittency in experimental measurements. The one dimensional surrogates of the energy dissipation rate are the most common variables in estimating the intermittency exponent. However, most of the geophysical measurement instruments have a much coarser resolution and are not suitable for measurements of the surrogates. As a result, the intermittency exponent can only be estimated indirectly. There are different methods for indirect estimations of μ, including scaling of sixth-order structure function, magnitude cumulant analysis, and local structure variables [see e.g. Anselmet et al., 1984, Basu et al., 2007, Chambers and Antonia, 1984, Muschinski, 2004]. The universality of small scale turbulence is the primary assumption in all indirect measurement methods. In this section, various definitions of direct measurements of the intermittency exponent are presented and the differences are discussed.

The original definition of the intermittency exponent is in terms of locally averaged energy dissipation rate as below:

$$\langle \epsilon_r^2 \rangle \sim r^{-\mu_1}. \tag{3.9}$$

This definition is generally used in theoretical models. For Homogeneous turbulence one can define the intermittency exponent in terms of autocorrelation of the dissipation rate as below:

$$\langle \epsilon_0(x)\epsilon_0(x+r) \rangle \sim r^{-\mu_2} \tag{3.10}$$

By assuming statistical homogeneity and isotropy of small scale turbulence, $\mu_1 = \mu_2$ [Monin and Yaglom, 1975, see e.g.]. The above equation can be written in Fourier space in terms of spectral density of the energy dissipation rate as below:

$$E_{\epsilon\epsilon}(\kappa) \sim \kappa^{\mu_3 - 1} \tag{3.11}$$

This definition is commonly used in physical experiments for determining μ despite its limitations in the flows with finite Re. The differences between the scaling range of the real space and wave number space could be the source of the difference between μ_2 and μ_3. The intermittency exponent also has been defined as below:

$$\langle [\epsilon_0(x) - \langle \epsilon_0(x) \rangle][\epsilon_0(x+r) - \langle \epsilon_0(x) \rangle] \rangle \sim r^{-\mu_4} \tag{3.12}$$

This definition is equivalent to Eq.(5.7) at very high Re. Thus, μ_3 and μ_4 are good approximations of μ only at very high Re. Finally assuming the validity of the lognormal hypothesis (K62), the intermittency exponent can be defined as:

$$\sigma^2_{\log \epsilon_r} = A - \mu_5 \log r. \tag{3.13}$$

Corresponding to each surrogate for ϵ_0 is an estimate for the intermittency exponent denoted by tilde symbol, e.g.,

$$\langle \tilde{\epsilon}^2_{r,1} \rangle \sim r^{-\tilde{\mu}_{1,1}} \ . \tag{3.14}$$

In this research work, the intermittency exponent refers to μ_1 unless it is mentioned otherwise. In high Re flows there is an agreement on the common value of 0.25 ± 0.05 for the intermittency exponent [Antonia et al., 1981, 1982, Chambers and Antonia, 1984, Sreenivasan and Antonia, 1997, Sreenivasan and Kailasnath, 1993]. Cleve et al. [2003] showed that the two-point correlation function of the energy dissipation surrogates provides an estimate of μ closer to the direct measurements based on the energy dissipation rate. The effects of surrogates on the other estimates of μ are significant. These effects are discussed in more detail in Cleve et al. [2003, 2004], Kurien et al. [2000].

3.4 Small-scale Intermittency in Complex Flows

Estimating small scale intermittency in flows dominated by the large scale anisotropies, known as complex flows, is a challenge. Our knowledge on intermittency mostly relies on the surrogates while the majority of the assumptions inherent in the surrogates are not valid in the complex flows. In general, small scale isotropy, which is the key assumption in the surrogates, is a dubious concept in the flows dominated by stratification, shear, and rotation. In classical intermittency analysis including geophysical flows, the small scale isotropy has been taken for granted and the conventional methods of intermittency estimations are applied despite the fact that the effects of large scale anisotropies are not negligible [see e.g. Klewicki et al., 1998, Lumley and Panofsky, 1964, Metzger and Klewicki, 2001, Wyngaard, 1992, Wyngaard et al., 2001].

The small scale anisotropy has been the focus of modern turbulence theory research in the past ten years [see e.g. Benzi et al., 2010, Biferale and Procaccia, 2005, Biferale et al., 2004, 2008b, Bos et al., 2007, Casciola et al., 2007, Kaneda and Yoshida, 2004, Kurien et al., 2000]. It is hypothesized that due to the intermittent nature of turbulence, the decay of large scale anisotropies is slower than the predictions of dimensional analysis. Therefore, anisotropy may persist even at the smallest scales of motion. The small scale anisotropy affects the local characteristics of turbulence strongly. It is hypothesized [Biferale and Procaccia, 2005, Biferale et al., 2002, 2008b] that the scaling exponents are superposition of isotropic and anisotropic effects and drift from the dimensional scaling laws by increasing the degree of anisotropy.

As a result of small scale intermittency, the approach to isotropy depends on the geometry of turbulence and is not the same for all directions. The directional statistics, like one-dimensional surrogates of energy dissipation rate, are weighted differently by anisotropy and consequently exhibit different scaling exponents. Thus, validity of the surrogates and their efficiency in estimating intermittency is doubtful in complex flows. To clarify the effects of large scale anisotropy on the small scale

characteristics of turbulence, and consequently on the intermittency, density stratified turbulence with different degrees of stratification is considered. The effects of stratification on the dynamics of the flow over a range of scales are covered in chapters 6 and 7.

3.5 Direct Numerical Simulations of Small-scale Turbulence

The foregoing discussion illustrates potential issues in predicting intermittency of turbulent flows. To obtain detailed knowledge on the small scale characteristics of turbulence and quantify the impact of the surrogates, direct and exact measurements of intermittency are required. The experimental measurements of intermittency related statistics are challenging and require sophisticated measurements techniques. As an alternative, the DNS of turbulence has been proved to be a powerful tool in evaluating theories and assumptions in fluid turbulence [see e.g. Eswaran and Pope, 1988, Hebert and de Bruyn Kops, 2006, Herring, 1974, Orszag and Patterson, 1972, Riley and Metcalfe, 1980, Riley et al., 1981, Vervisch and Poinsot, 1998]. The computational cost of DNS is very high and the number of operations grows rapidly with Re. Thus, such simulations can be carried out only for relatively low Re and simple geometries. When properly done, DNS provides a full description of the turbulent flow with very fine temporal and spatial resolution close to the Kolmogorov's scale. As a result, exact values of the instantaneous local energy dissipation rate and its surrogates are available and direct measurements of intermittency can be compared with the estimates based on the surrogates. The caveats are that the DNS must be computed using an accurate numerical method, at high enough Re so that intermittency is pronounced, and with a sufficiently fine numerical grid so that the intermittency is resolved.

A number of studies have considered the characteristics of DNS suitable for studying small scale turbulence and intermittency. In particular, the dependency of small

scale statistics on the Reynolds number is analyzed in several studies [see e.g. Gulitski et al., 2007a,b, Ishihara et al., 2007, 2009, Schumacher, 2007, Yeung et al., 2005, 2006a,b, Zhou and Antonia, 2000b] and the effects on intermittency of insufficient small scale resolution in DNS is investigated by Donzis et al. [2008], Schumacher et al. [2005, 2007], Wan et al. [2010], Watanabe and Gotoh [2007], Yakhot and Sreenivasan [2005]. From these studies, we conclude that the Reynolds number based on the Taylor microscale and the rms velocity must be 100 or more and that the grid spacing must be no more than a Kolmogorov length scale to capture intermittent structures of turbulence accurately. Note that the resolution criteria depends on the order of the statistics under consideration and that higher resolution is needed to accurately compute the statistics of energy dissipation rate than of velocity [Yakhot and Sreenivasan, 2005]. Additionally, we observe that the current generation of supercomputers is capable of simulating flows at high enough resolution that numerical roundoff error will effect higher-order statistics of ϵ_r unless careful attention is paid to the numerics, possibly including the use of 128-bit arithmetic to compute the statistics.

In the next chapters, we introduce and apply a methodology using DNS to study small scale turbulence, intermittency, and verify some of the related models and theories. The goal is to investigate universality of the small scale turbulence. The DNSs of two different turbulent flows, considering the numerical criteria discussed in the previous paragraph, are designed and developed for studying small scale turbulence. The highly resolved DNSs of isotropic homogeneous turbulence as well as density stratified turbulence are considered. The general characteristics of the flow fields in terms of classical turbulence models and theories are investigated.

The energy dissipation rate and its surrogates are analyzed using the DNS of isotropic homogeneous turbulence over a range of Reynolds numbers. The DNS of isotropic turbulence is the closest isotropic flow that one can achieve. Such flow is very rare in nature and physical experiments, nonetheless it is a hypothetical DNS

flow for evaluating models and theories. In the absence of the large scale anisotropies, local statistics are almost isotropic and the crucial assumption behind the energy dissipation surrogates is fulfilled. The general methodology is to compare the statistical characteristics and the scaling exponents of the energy dissipation surrogates with the direct measurements of energy dissipation rate. Note that in DNS the direct measurement of intermittency is possible without relying on any models and assumptions. The detailed description of the methodology and results of this simulation are provided in the next two chapters.

We are also interested in the characteristics of small scales in the flows dominated by large scale anisotropies. the DNS data of density stratified turbulence with different levels of stratification is employed. These unique data sets are highly resolves at small scale, while capture the anisotropic flow at larger scales due to extended dynamic range. The small scale statistics are extracted from the DNS of stratified turbulence and are compared with those of isotropic turbulence. The deviation of the statistics from the isotropic turbulence theory and classical models are discussed in term of stratification effects and large scale anisotropies.

CHAPTER 4

DIRECT NUMERICAL SIMULATIONS OF ISOTROPIC HOMOGENEOUS TURBULENCE

In this chapter, the DNS data set of isotropic homogeneous turbulence designed for studying small scale turbulence and intermittency is introduced. The details of the simulations and the related parameters are discussed in the first section. The second section, includes the results of primary analysis of data to investigate the data quality for the small scale studies. A special attention is paid to the Reynolds number and resolution dependency of the results. The small scale isotropy of the flow is investigated. Further investigation of this data set related to the small scale turbulence and intermttency are covered in the next chapter.

4.1 Numerical Simulations

4.1.1 Governing Equations and Numerical Method

The simulated flows are the solution to the Navier-Stokes equations in three spatial dimensions:

$$\nabla \cdot \boldsymbol{u} = 0 \tag{4.1a}$$

$$\frac{\partial \boldsymbol{u}}{\partial t} + \boldsymbol{u} \cdot \nabla \boldsymbol{u} = -\nabla p + \nu \nabla^2 \boldsymbol{u} + \boldsymbol{b} \; . \tag{4.1b}$$

The velocity vector is $\boldsymbol{u} = [u, v, w]$, p has been divided through by the (constant) density, and $\boldsymbol{b}$ is a time-varying force applied to maintain the flow statistically stationary. The equations are advanced in time using a third-order Adams-Bashforth accurate fractional step method for the non-linear and pressure gradient terms while the linear term is integrated exactly in Fourier space. A pseudo-spectral method is used to

compute the spatial derivatives. To eliminate aliasing errors, the non-linear term in the momentum equation is computed in rotational form and a spectral truncation filter is applied each time step to remove energy from wave numbers greater than 2/3 times the maximum wave number. The numerical domain has length $\mathcal{L} = 2\pi$ on each side.

The velocity fields are initialized with the turbulent fields reported by de Bruyn Kops and Riley [1998] and then forced so that $E(\kappa) \propto \kappa^{-5/3}$ at low wave numbers. In the simulations, $E(\kappa)$ is computed by averaging the energy for all points in a wave number 'shell', that is, for all points having $\kappa - \Delta\kappa/2 \leq \kappa < \kappa + \Delta\kappa/2$ with $\Delta\kappa$ the width of the shell. The force, $\boldsymbol{b}$, is applied simply by amplifying the magnitudes of the Fourier-space velocities belonging to the shell without altering their relative magnitudes or phases. The amplification factor is chosen so that the simulated spectrum converges to the target spectrum over some range of wave numbers. Specifically, the method of Overholt and Pope [1998] is applied for wave numbers $1 \leq \kappa/\kappa_0 \leq \kappa_f/\kappa_0$ where $\kappa_0 = 2\pi/\mathcal{L}$ is the smallest non-zero wave number represented in the simulations and $\kappa_f/\kappa_0 = 4$.

4.1.2 Preliminary Simulations and Stationarity

The forcing technique used to energize the large scales in the simulations is analogous to a spring-and-damper designed to bring the system to steady state quickly and with little oscillation. As reported by Overholt and Pope [1998], the method performs very well. Nevertheless, it does not yield velocity fields that are exactly stationary because of the chaotic nature of turbulence. The focus of this research, however, is on dissipation rate and intermittency in statistically stationary turbulence. Therefore, before proceeding further with descriptions of the simulations, the degree of stationarity that is achieved by the numerical simulation technique is con-

sidered in this section. Additionally, the response time of the flow fields to changes in the simulation parameters is investigated.

To consider stationarity, we investigate a preliminary simulation with 512 grid points in each direction. This simulation is denoted case R2a with parameters given in §4.1.3. It is a small enough simulation so that it can be run for a long time in order to ensure that it is statistically stationary. Nevertheless, it is adequately resolved spatially by the criterion of Eswaran and Pope [1988] for the study of average statistics and is useful for considering the question of stationarity. In this case, the ensemble used for computing the statistics of random variables includes the entire simulation domain sampled 10,000 times over the period of 10 turbulence time scales. So $\langle k \rangle$ and $\langle \epsilon \rangle$ are the expected values of the turbulence kinetic energy and its dissipation rate. No subscript is used with ϵ here because the simulation is not sufficiently resolved for the quantity to be considered ϵ_0. It is simply the dissipation rate computed at the resolution of the simulation. With these definitions, the turbulence time and length scales are $T = \langle k \rangle / \langle \epsilon \rangle$ and $L = \langle k \rangle^{3/2} / \langle \epsilon \rangle$.

The time series of the spatially averaged kinetic energy and dissipation rate are shown in Figure 4.1 where $\overline{k}$ and $\bar{\epsilon}$ are the instantaneous quantities averaged over the entire simulation domain at an instant in time. Both have been normalized by their expected values in order to investigate variation about the mean values with time. The instantaneous averages wander over a range of about $\pm 2\%$ of the mean value for the energy and about $\pm 7\%$ of the mean value for the dissipation rate with the standard deviations of $\overline{k}$ and $\bar{\epsilon}$ about their mean values being 0.012 and 0.046 respectively.

Next we examine the response of the simulation to changing the viscosity. This is of interest in general because it reveals information about how turbulence responds to changes at small length scales, but it is discussed here because the simulations presented in §4.1.3 with higher Re were developed from those with lower Re and it is

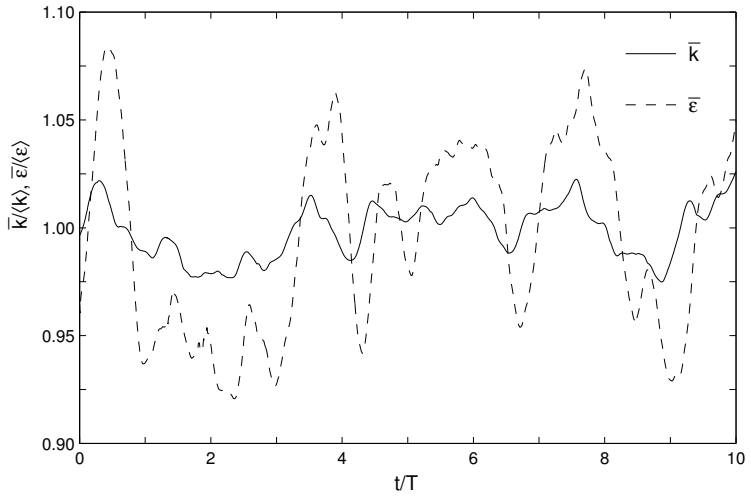

Figure 4.1: Spatially averaged turbulence kinetic energy and its dissipation rate for the preliminary simulation. The expected values are determined from time-space averages over the computational domain and the period shown in the figure.

important to know how long the simulations must be run for statistical stationarity to be expected. To accomplish this test, the preliminary simulation was run until it was stationary as discussed in conjunction with Figure 4.1. This time is defined as t_0 at which the kinematic viscosity was suddenly decreased by a factor of two. After some additional time, the viscosity was set back to its original value. The results of this test are shown in Figure 4.2 where $\bar{\epsilon}/\langle\epsilon\rangle$ can be seen to be approximately 0.5 at $t - t_0 = 0$ due to the prompt decrease in ν. The instantaneous spatially averaged dissipation rate, $\bar{\epsilon}/\langle\epsilon\rangle$, slowly increases toward unity, overshoots slightly, and is about unity by $(t - t_0)/T \approx 0.9$ when the viscosity is restored to its original value and a second transient begins. From the two transients, it can be deduced that it takes on the order of a turbulence time scale, T, for the flow to adjust to changes in ν. Thus, the dissipation rate responds at the time scale of the energy-containing motions in the flow as is typically assumed for isotropic homogeneous turbulence.

Also shown in Figure 4.2, are the mean kinetic energy scaled by $\langle k\rangle$ and the mean forcing power scaled by $\langle\epsilon\rangle$. Not surprisingly, $\overline{k}/\langle k\rangle$ is not noticeably affected

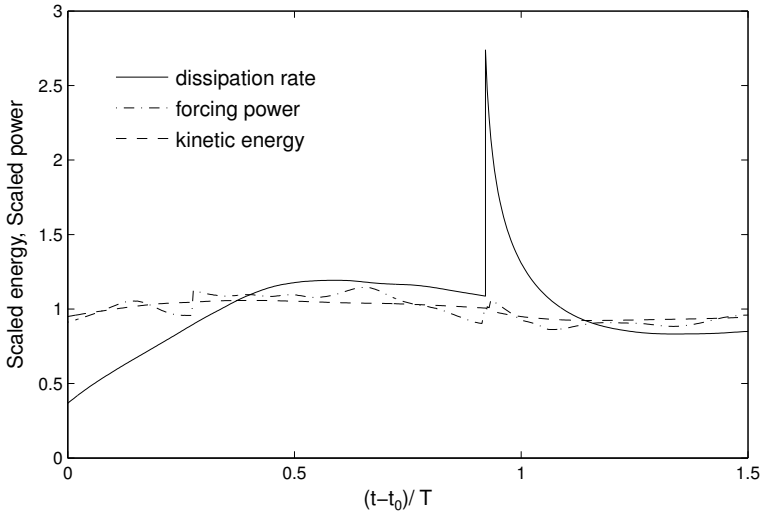

Figure 4.2: Kinetic energy, its dissipation rate, and forcing power versus time after the viscosity is suddenly changed.

by changes in ν and neither is the forcing power since only low wave numbers are amplified by the forcing scheme. The small jumps in the forcing power are due to the simulation being stopped and restarted without saving the time history of the solutions to the differential equations used in the forcing scheme.

4.1.3 Simulation Parameters

Based on the results from the preceding section, three simulation cases were developed from the preliminary simulation. The forced part of the spectrum for each is the same. The Re was varied by adjusting the kinematic viscosity with the objective of obtaining values of the Kolmogorov length scale that vary by factors of two. So case R2 was produced by increasing the resolution on case R2a, and then the viscosity was increased and decreased by factors of $2^{4/3}$ to produce the lower and higher Re cases, respectively. The resulting simulation parameters are shown in table 4.1. In contrast to the foregoing discussion on the preliminary simulations, the ensemble here and henceforth is defined as the entire spatial domain at an instant in time. Thus, all the statistics are Eulerian and there is no commingling of spatial and temporal statistics

Identifier	Re_L	Re_λ	N	$\eta\kappa_{\max}$	η/Δ	λ/η	ℓ/η	L/η	$L/\mathcal{L}$
R1	1546	102	1024	6.6	3.14	19.8	57.50	247	0.76
R2a	3197	146	512	1.6	0.75	23.8	106.2	425	0.62
R2	3426	151	2048	6.4	3.04	24.2	110.4	448	0.66
R3	8275	235	2048	3.1	1.50	30.2	216.4	868	0.64

Table 4.1: Simulation Parameters.

so that our definitions are consistent with K41 and K62. The length scales are defined in §2.1. The Reynolds numbers are defined by $Re_L = \bar{k}^2/\bar{\epsilon}\nu$ and $Re_\lambda = \left(20\bar{k}^2/3\bar{\epsilon}\nu\right)^{1/2}$. The number of grid points in each direction is denoted N and the small scale resolution is given in term of the grid spacing $\Delta = \mathcal{L}/N$ and the maximum wave number, $\kappa_{\max}$, the latter taking into account the dialiasing filter.

4.2 Overview of Simulated Flows

The parameters in Table 4.1, in conjunction with the literature cited in §3.5, lead us to expect the simulations to be well suited for studying small scale turbulence and intermittency. Note the extraordinary high resolution of the simulations compared with the standard resolution of DNS, $\eta = 0.5\Delta$. It is worthwhile, however, to verify general characteristics of the simulated flows before considering specifics about the surrogates for ϵ_0 and intermittency. We begin our analysis with an overview of the data quality with focus on the small scale resolution and isotropy of the flow field. Then we proceed to spectra and structure functions of the velocity fields. Note that the entire domain of the simulated flow at an instant in time is considered as the sampling volume and therefore, there is no commingling of spatial and temporal statistics.

4.2.1 Local Velocity

For a qualitative view of the range of length scales that exist in the simulations and the resolution of the small scales, consider contour plots of the instantaneous velocity in case R2. In Figure 4.3, the vertical velocity on a horizontal plane is shown at three different magnifications. The velocity is scaled by the rms velocity $u' = (2\bar{k}/3)^{1/2}$. From the top panel in the figure, which shows the entire extent of the simulation domain, it appears that there are regions correlated over about half the domain which is consistent with the values for $L/\mathcal{L}$ in Table 4.1. Since the boundary conditions are periodic this is the largest possible correlation length scale and is indicative of the trade-off made in favor of small scale resolution over large scale resolution and to use forcing to produce the effects of motions at length scales larger than the simulation domain. de Bruyn Kops and Riley [1998], in contrast, report a simulation of isotropic homogeneous turbulence specifically designed to have sufficient large scale resolution so that the simulated flow evolved comparably to a similar laboratory flow. In that paper, it is shown that the simulation domain should be 20 times the size of the energy containing eddies, compared with two times for the current simulations, for the simulation to have good large-scale resolution.

The lower two panels in Figure 4.3 are magnifications of the top panel with the region displayed being outlined with a black box in the panel immediately above. In the bottom panel, it is apparent that the velocity change is quite small on the length scale of the grid spacing. We can see graphically what it means that η is about three times the grid spacing.

In Figure 4.4, the probability density of the velocity fluctuations is shown for case R2. In the left panel the axes are linear while in the right panel logarithmic spacing is used on the abscissa. It is apparent that the fluctuations are very nearly Gaussian within several standard deviations of the mean value. The probability of very high fluctuation magnitudes is less than that predicted by the Gaussian function, which

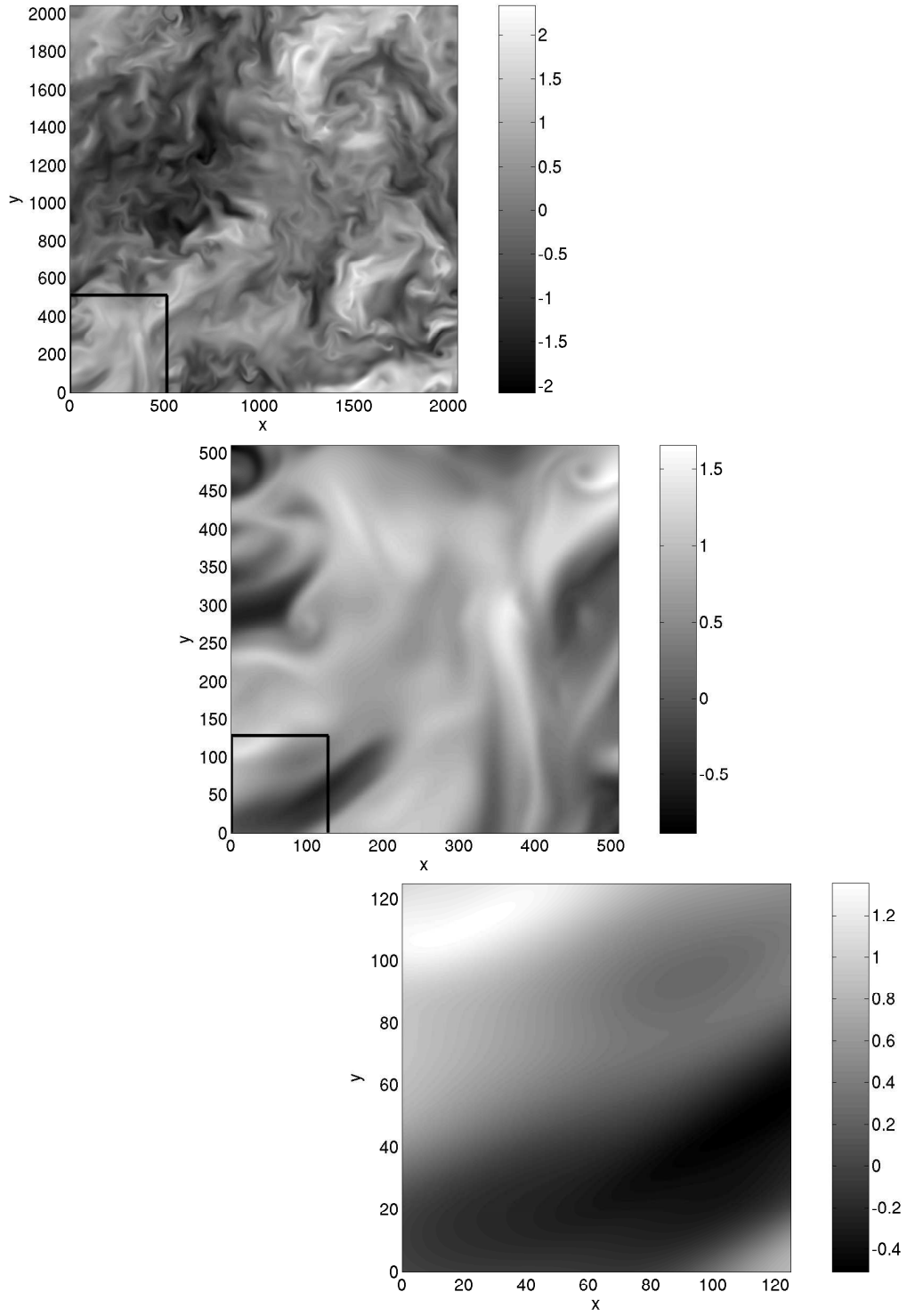

Figure 4.3: Scaled vertical velocity, w/u', from case R2 on a horizontal plane. Axes are labeled in units of grid points. In the lower two panels, the region plotted is that enclosed in the black box in the panel immediately above. Note that the color scale is different for each panel.

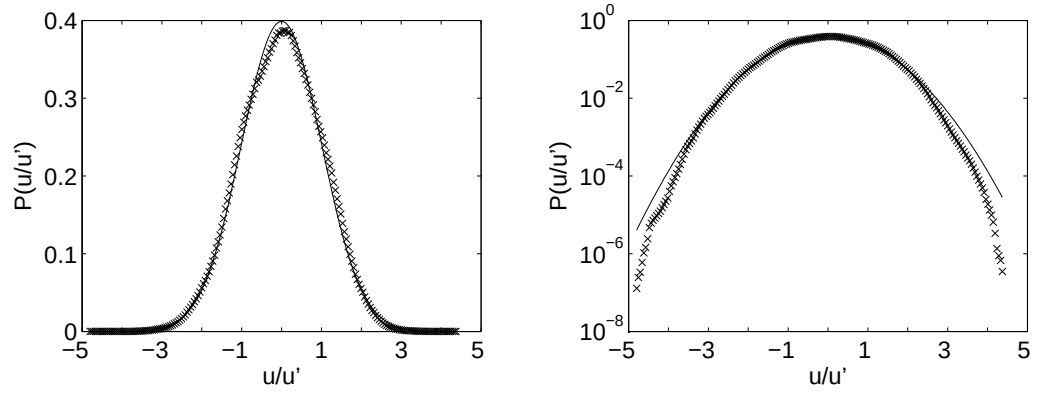

Figure 4.4: Probability density of the instantaneous velocity fluctuations for case R2. Symbols represent simulation data and the line is the Gaussian function computed from the mean and variance of the data.

is not surprising since the Gaussian model predicts finite probability of arbitrarily large fluctuations and, therefore, arbitrarily high kinetic energy. There are, however, a significant number of instances with $|u/u'| > 4$, which indicates that there are patches of very strong turbulence. The p.d.f.s in the larger simulations with higher Re have longer tails revealing more details about the rare events.

4.2.2 Velocity Gradients

Velocity gradients are the building blocks of the energy dissipation rate and its surrogates. The statistical characteristics of the velocity gradients have a direct effect on the statistics of energy dissipation and its surrogates. The p.d.f.s of two longitudinal gradients and two transverse gradients for case R3 are shown in the top panel of Figure 4.5. Only for very infrequent values of the gradients are differences between the two p.d.f.s in each pair apparent. In the bottom panel of Figure 4.5, the p.d.f.s of selected velocity derivatives are compared for R2 and R3. The general shape of p.d.f.s of longitudinal gradients are different than those of the transverse components. To quantify these differences we introduce the skewness and kurtosis for the variable X:

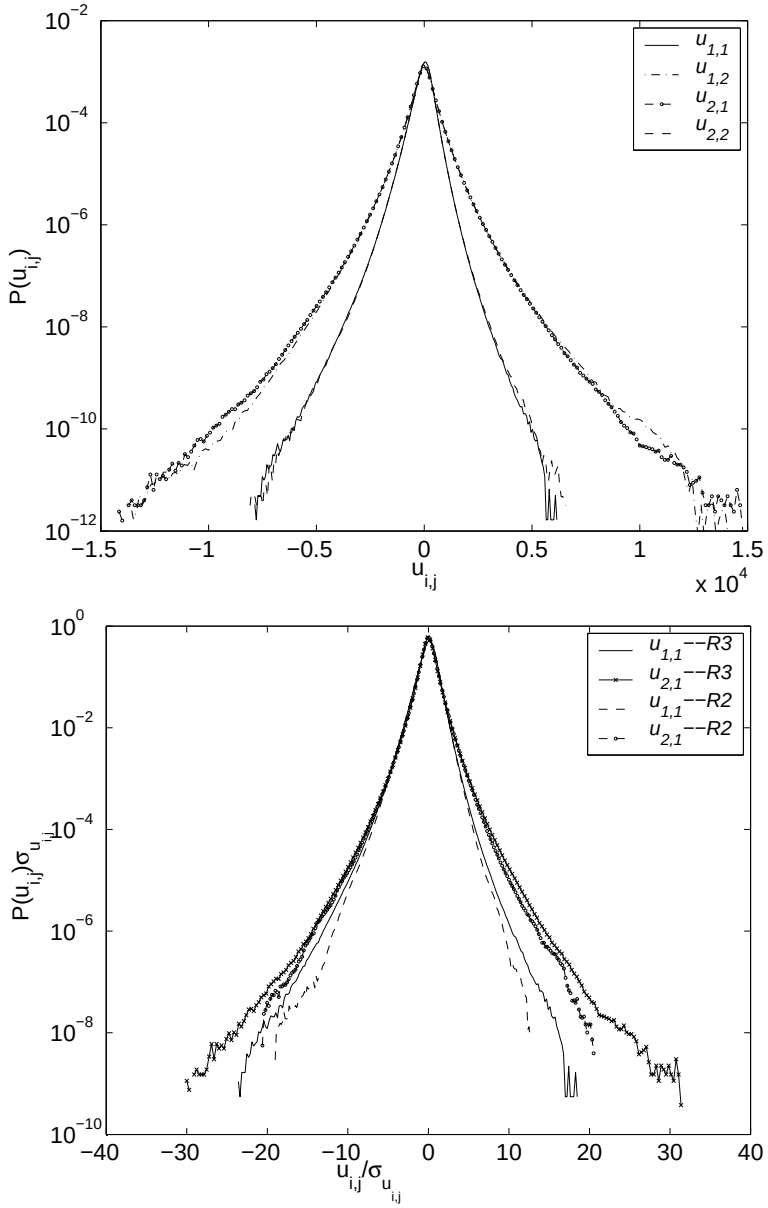

Figure 4.5: The p.d.f.s of the longitudinal and transverse velocity gradients. Top panel: verification of isotropy for case R3. Bottom panel: results for cases R2 and R3 show effect of Reynolds number.

$$S = \frac{\langle (X - \langle X \rangle)^3 \rangle}{\langle (X - \langle X \rangle)^2 \rangle^{3/2}}, \tag{4.2}$$

and,

$$K = \frac{\langle (X - \langle X \rangle)^4 \rangle}{\langle (X - \langle X \rangle)^2 \rangle^2}. \tag{4.3}$$

The skewness represents asymmetry in the field and the kurtosis represents the tails of pdf corresponding to the extreme events. The averaged skewness of the longitudinal derivatives are -0.50, -0.53 and -0.55 and the averaged kurtosis are 4.9, 5.9, and 6.6 for cases R1, R2, and R3, respectively. The Re dependency of skewness and kurtosis of the longitudinal velocity gradients fit well with power laws as $S_L \approx (0.30 \pm 0.01) Re_\lambda^{0.11 \pm 0.01}$ and $K_L \approx (1.00 \pm 0.20) Re_\lambda^{0.35 \pm 0.04}$, which are consistent with those of Ishihara et al. [2007] and the references there. The transverse gradients show a different numerical value of skewness and kurtosis as well as different Re dependency. The skewness of the transverse gradients for all the cases is very small and almost zero($\approx 10^{-2}$) while the kurtosis has much higher values (6.9, 8.7 and 9.9 for R1, R2, and R3) with the Reynolds dependency of $K_N \approx (1.00 \pm 0.30) Re_\lambda^{0.42 \pm 0.04}$. High kurtosis is an indication of intermittency being exhibited in the velocity derivatives and values greater than three result from distributions having higher probability densities for extreme events than in a Gaussian distribution. So the longitudinal derivatives are substantially more skewed but exhibit less intermittency than the transverse derivatives. This suggests that the p.d.f.s of $\tilde{\epsilon}_{0,1}$ and $\tilde{\epsilon}_{0,2}$, will provide significantly different approximations for the p.d.f. of ϵ_0.

4.2.3 Small-scale Resolution and Statistical Convergence

The notation ϵ_0 is used to represent energy dissipation rate at the grid resolution. Implicit is the assumption that the spatial resolution of the simulations is sufficient so that differences between ϵ_0 and the exact local dissipation rate are not significant. When ϵ_0^n is considered, differences between ϵ_0 and the exact local dissipation rate clearly become important for a sufficiently high value of n. Donzis et al. [2008]

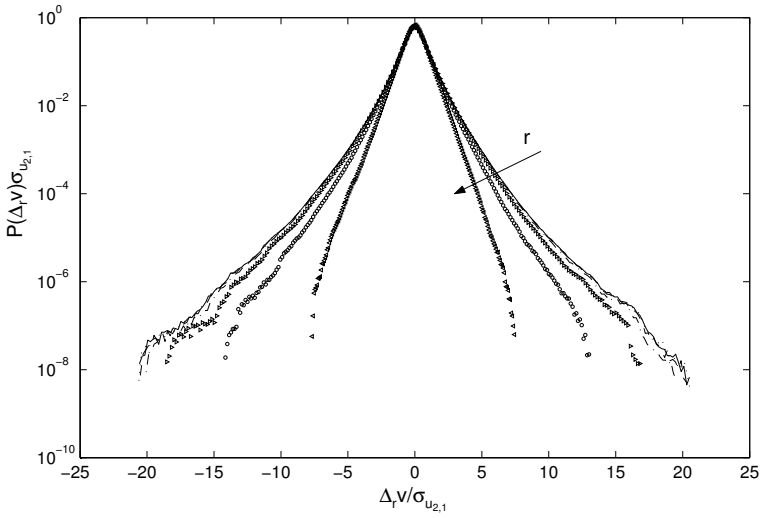

Figure 4.6: The p.d.f.s of the transverse velocity increment, $\Delta_r v$, normalized by the rms value of transverse velocity gradient $\sigma_{u_{2,1}}$ of R2. The plots are for separation distance $r/\eta = 0.3, 0.7, 1.3, 2.6, 5.3, 11$. The solid line represents p.d.f of transverse velocity gradient.

showed that for simulations with Reynolds numbers comparable to those in the current simulations, ϵ_0^4 is accurate provided $\eta/\Delta > 1$, a criterion that is satisfied in all the cases reported in this paper. Figure 4.6 shows the fine resolution of our simulations in terms of p.d.f.s of the transverse velocity increments for different separation distances for case R2. The p.d.f.s are almost identical to the p.d.f. of the transverse velocity gradient for the separation range of $r = 1\Delta \sim 6\Delta < 2\eta$.

Given that the local values of ϵ_0^n are accurate for values of n up to at least four, it is still necessary to check for what values of n is $\langle \epsilon_0^n \rangle$ statistically converged. The nth-order moment of ϵ_0 is statistically converged if $\epsilon_0^n P(\epsilon_0)$ of the ensemble approaches zero for large $\epsilon_0/\overline{\epsilon}$ [Donzis et al., 2008, Hamlington et al., 2012]. Here $P(\epsilon_0)$ is the probability density function of ϵ_0, which is computed by binning the data to form the histogram. The integrands for the fourth-order moments of the dissipation rate and the transverse surrogate are plotted in Figure 4.7. The convergence is good for both quantities in all three simulations.

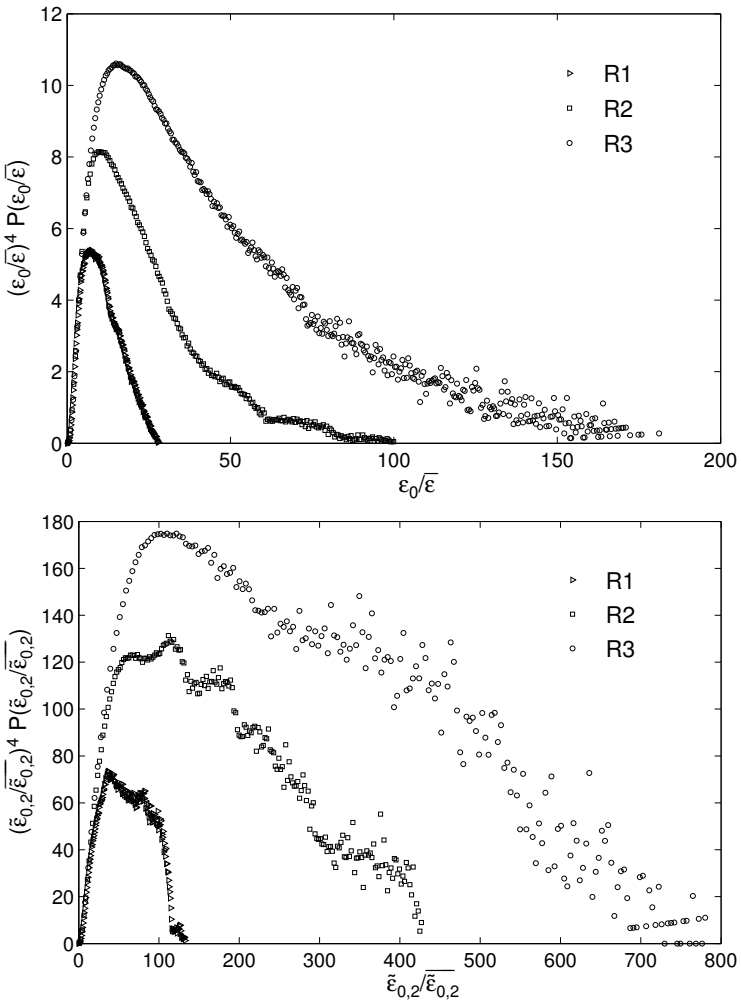

Figure 4.7: Convergence test of the fourth-order moments of normalized energy dissipation rate (left) and its transverse surrogate (right) for R1, R2, and R3.

4.2.4 Isotropy of Velocity Gradients

Motivating the definitions of the dissipation rate surrogates is the assumption that the flow is locally isotropic. Isotropy implies specific relationships between the moments of the velocity gradients and certain "invariants" that do not change with the rotation of coordinates in incompressible flow [Hierro and Dopazo, 2003, Siggia, 1981b]. Let

$$F_1^2 \equiv 2I_0/15, \tag{4.4a}$$

$$F_2^2 \equiv 4I_0/15, \tag{4.4b}$$

$$F_3^2 \equiv -I_0/15, \tag{4.4c}$$

$$F_1^4 \equiv 4I_1/105, \tag{4.4d}$$

$$F_2^4 \equiv 3I_1/140 + 11I_2/140 - 3I_3/35 + I_4/80, \tag{4.4e}$$

$$F_3^4 \equiv 11I_1/672 - 61I_2/3360 + 23I_3/840 + 7I_4/640, \tag{4.4f}$$

where the invariants are

$$I_0 \equiv \langle s_{ij}s_{ji}\rangle\,, \quad I_1 \equiv \left\langle (s_{ij}s_{ji})^2\right\rangle, \quad I_2 \equiv \left\langle \omega^2(s_{ij}s_{ji})\right\rangle, \quad I_3 \equiv \langle \omega_i s_{ij}s_{jk}\omega_k\rangle\,,$$

and $I_4 \equiv \langle(\omega^2)^2\rangle$, with ω the modulus of the vorticity vector. In table 4.2 the values of F_i^{2n} are shown relative to the corresponding moments of the velocity derivatives for case R3; the values for the other cases are comparable. In the first section of the table, the three choices for longitudinal surrogates are tabulated followed by those for the transverse and asymmetric surrogates in the other two sections. If the simulated flows were perfectly isotropic then all of the ratios in the table would be unity. We see from the tabulated values that the flow is sufficiently isotropic and the effect of anisotropy is negligible even for the fourth-order moments.

Another way to gage the effect of anisotropy on the surrogates is to compare the kurtosis of each velocity derivative. These are listed in table 4.3. Here the fact

	n=1	n=2
$\left\langle u_{1,1}^{2n} \right\rangle / F_1^{2n}$	0.996	0.991
$\left\langle u_{2,2}^{2n} \right\rangle / F_1^{2n}$	0.998	0.995
$\left\langle u_{3,3}^{2n} \right\rangle / F_1^{2n}$	1.000	1.001
$\left\langle u_{1,2}^{2n} \right\rangle / F_2^{2n}$	0.998	1.070
$\left\langle u_{1,3}^{2n} \right\rangle / F_2^{2n}$	0.998	1.063
$\left\langle u_{2,1}^{2n} \right\rangle / F_2^{2n}$	1.000	1.081
$\left\langle u_{2,3}^{2n} \right\rangle / F_2^{2n}$	1.005	1.113
$\left\langle u_{3,1}^{2n} \right\rangle / F_2^{2n}$	1.001	1.091
$\left\langle u_{3,2}^{2n} \right\rangle / F_2^{2n}$	1.000	1.090
$\left\langle u_{1,2}^{n} u_{2,1}^{n} \right\rangle / F_3^{2n}$	0.994	0.963
$\left\langle u_{1,3}^{n} u_{3,1}^{n} \right\rangle / F_3^{2n}$	0.998	0.959
$\left\langle u_{2,3}^{n} u_{3,2}^{n} \right\rangle / F_3^{2n}$	1.002	0.978

Table 4.2: The ratio of the moments of the velocity gradients to the isotropic values based on invariants for case R3, with $u_{i,j} \equiv \partial u_i / \partial x_j$.

	$u_{1,1}$	$u_{2,2}$	$u_{3,3}$	$u_{1,2}$	$u_{1,3}$	$u_{2,1}$	$u_{2,3}$	$u_{3,1}$	$u_{3,2}$
R1	4.99	4.85	4.86	7.52	6.82	6.71	6.45	6.87	7.03
R2	5.95	5.72	5.95	8.47	8.96	8.91	8.53	9.23	8.23
R3	6.57	6.58	6.59	9.84	9.78	9.91	10.0	9.97	9.97

Table 4.3: Kurtosis of the longitudinal and transverse velocity gradients for R1, R2, and R3.

that the three simulations have different Reynolds number is helpful; the variation in kurtosis due to even a modest change in Reynolds number is much larger than that due to anisotropy. It is also noted that the kurtosis values are in good agreement with those reported in the literature for flows with similar Reynolds numbers. See, e.g., Gotoh et al. [2002], Ishihara et al. [2007], Jiménez et al. [1993], Wang et al. [1996] and references cited therein.

The conclusion drawn from the data in tables 4.2 and 4.3 is that the flow is quite close to isotropic. Differences between, say, the three choices for the longitudinal

surrogate are much smaller than between the longitudinal and transverse surrogates or between the same surrogate in cases R1, R2, and R3. Therefore, in the remainder of the dissertation only one of each surrogate will be considered, namely the ones in the definitions in §3.2 unless mentioned otherwise.

4.2.5 Energy Spectra

In this section, the energy spectra and structure functions of the velocity field are analyzed and compared with the K41 predictions. The Kolmogorov spectra, which are defined in §2.1, are shown on log-log and semi-log axes for cases R1, R2, and R3 in Figure 4.8. From the plots, several conclusions can be drawn. First, the simulations exhibit K41 scaling in the inertial range, and they have values of $\alpha \approx 1.5$, $\alpha_1 \approx 0.49$ and $\alpha_2 \approx 0.65$ consistent with those in the literature, [e.g. Saddoughi and Veeravalli, 1994]. Second, the rise in the spectra near $\eta\kappa = 0.1$, which is observed in flow measurements and known as the bottleneck effect, is evident in the simulated flows. This effect has been discussed in detail by Dobler et al. [2003], Donzis and Sreenivasan [2010], Ishihara et al. [2009], Lohse and Mullergroeling [1995]. Third, the simulations are resolved deep into the dissipation range as evidenced by the spectra decreasing rapidly with increasing wave number. Note that the cusp at the right end of the three-dimensional spectrum is due to truncation error, not aliasing error, as discussed by Jang and de Bruyn Kops [2007]. Fourth, the simulated flows exhibit increasing intermittency with increasing Re. This is evident from the slight differences in the slope of spectra in the dissipation range in each simulation.

The one-dimensional spectra also provide a useful measure of isotropy in the inertial range and a cross-check that K41 scaling is exhibited. The ratio $\phi_2(\kappa_1\eta)/\phi_1(\kappa_1\eta)$ is plotted in Figure 4.9. Recall from the ratio α_1/α_2 that the ratio of the spectra will be 4/3 if the flow is perfectly isotropic and the Re is infinite. The simulations with the higher Re, cases R2 and R3, agree well with theory. Additionally, the ratio

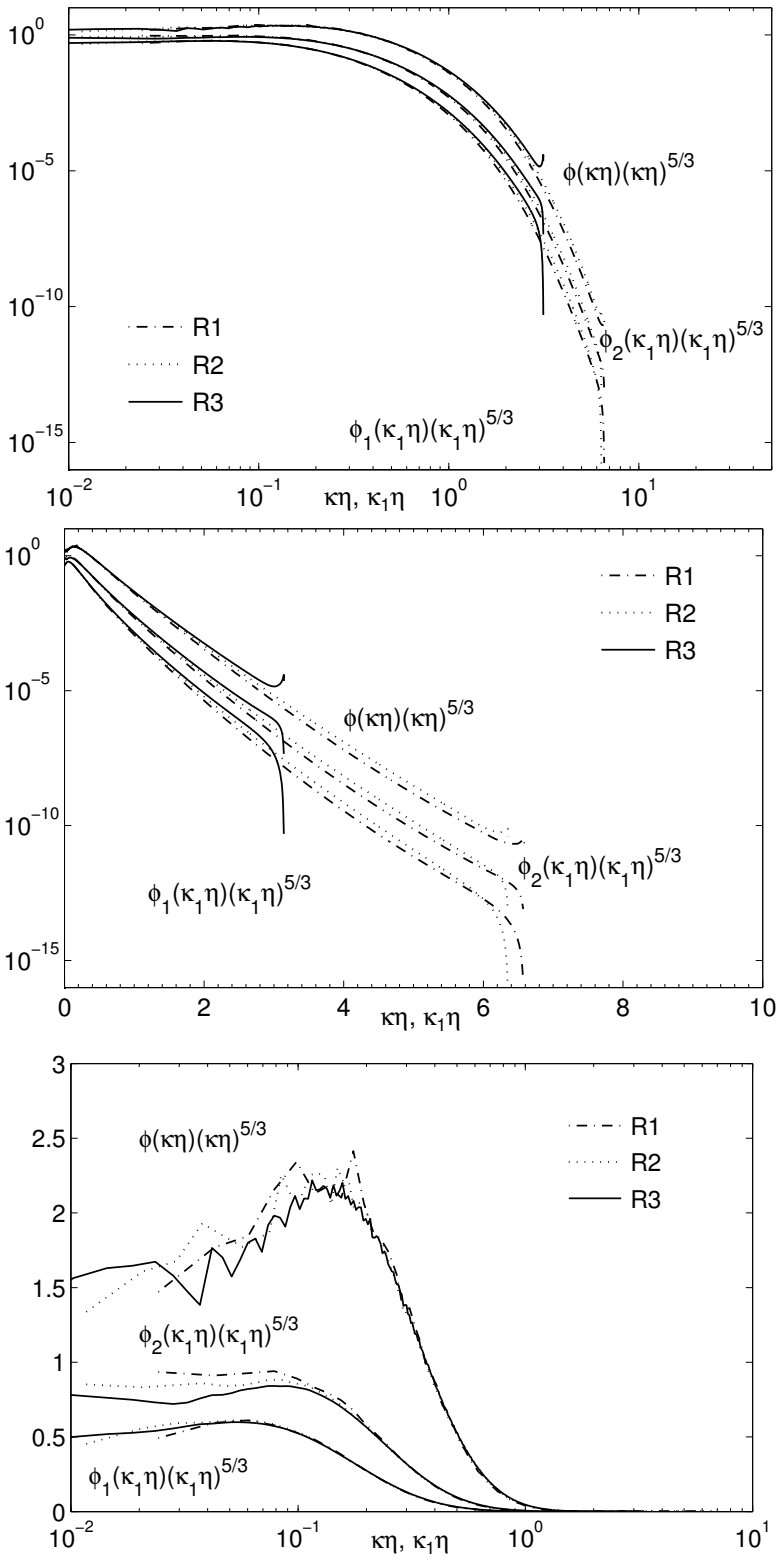

Figure 4.8: The Kolmogorov spectra plotted on log-log and semi-log axes.

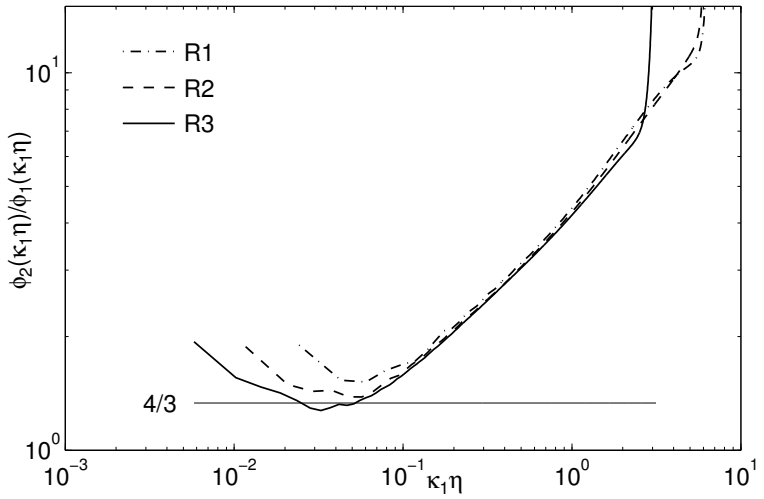

Figure 4.9: Ratio of the transverse to the longitudinal spectra.

$\phi_2(\kappa_1\eta)/\phi_1(\kappa_1\eta)$ suggests that the inertial range exists around $\kappa_1\eta \approx 3 \times 10^{-2}$. The results for case R1 suggest that the *Re* in this case is not high enough for this statistic to match the theory for high *Re* flows. Recall that the Taylor Reynolds number for this case is 102, which is at the lower limit suggested by the literature for simulations suitable for studying intermittency [Gulitski et al., 2007a,b, Ishihara et al., 2007, 2009, Yeung et al., 2006a,b, Zhou and Antonia, 2000b]. .

4.2.6 Structure Functions

In pseudo-spectral simulations, it is more efficient to compute the statistics in Fourier space. However, to have a better understanding of turbulence at different length scales, statistics in physical space are also presented. As noted in §2.1, Kolmogorov scaling is defined by Obukhov in terms of spectra and by Kolmogorov in terms of structure functions, but the two statistical quantities are exactly interchangeable only under assumptions not satisfied in the simulations. Therefore, for completeness, the second- and third-order longitudinal structure functions are shown as Figure 4.10.

The second- and third-order structure functions both exhibit two distinct regions of power law scaling corresponding to the dissipative and inertial scales. The dotted lines indicate the Kolmogorov power law behavior for the structure functions in these regions. The predicted power law exponent (K41) for the nth-order structure functions is n in the dissipation range and $n/3$ in the inertial range. The structure functions normalized by the Kolmogorov scaling represent Kolmogorov universal constants. These constants are discussed for the longitudinal structure functions as 2.0 for D_L^2 and at 4/5 for D_L^3 in §2.1. The normalized structure functions exhibit a plateau in the inertial range with numerical values very close to the universal constants. The width of the plateau representing inertial scaling range increases with Re and size of the simulation domain. The scaling holds very well for cases R2 and R3, but less well for case R1. This is consistent with the results from the spectra that case R1 has marginally high enough Re to be consistent with K41.

Note that Kolmogorov's 4/5 law is the only exact equation for turbulence expected to be valid at infinite or sufficiently high Re without reflecting intermittency effects. As a result, the existing difference between the measured constants from the normalized third-order structure function and its equivalent from high Re experiments (4/5), can be explained in terms of finite Re effects. The higher-order statistics of flows with finite Re are qualitatively similar to the high Re turbulence. To obtain the numerical values for the non-dimensional constants matching the high Re flows one can apply extended self similarity (ESS) hypothesis. For further information on ESS the reader is refer to Benzi et al. [1993]. In our simulations, a power law scaling range is observed for $\lambda/\eta \leq r/\eta \leq 3\lambda/\eta$ although the numerical value for the normalized second- and third-order structure functions in this region is slightly underestimating theoretical values. This range will be considered as the "scaling range" in our study. The scaling range is marked for case R2 on Figure 4.10.

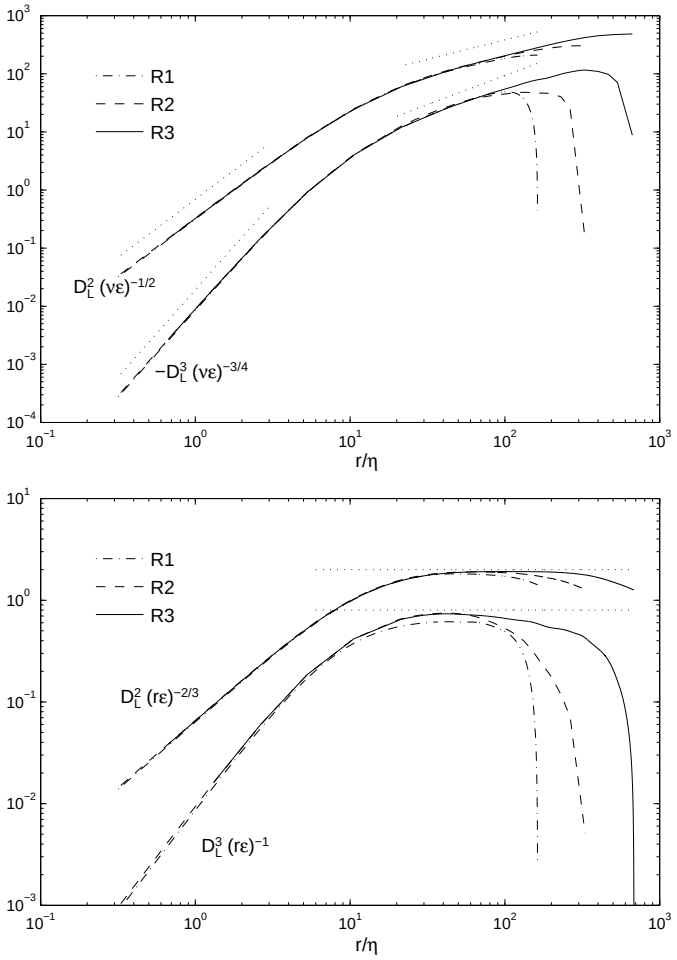

Figure 4.10: The longitudinal second- and third-order velocity structure functions. The dotted lines indicate the power law behavior in the dissipation and inertial ranges as predicted by K41. SR delineates $\lambda \leq r \leq 3\lambda$ for case R2.

CHAPTER 5

SMALL SCALE STATISTICS IN HOMOGENEOUS ISOTROPIC TURBULENCE

The results and discussion in the previous chapter show that the simulated flows are well resolved and suitable to study small scale dynamics including intermittency. In this chapter, we present the methodology and discuss the results of small scale turbulence studies and intermittency estimations using DNS of isotropic turbulence. A single snapshots of cases R1, R2, and R3 are chosen for this investigation. In section 3.2, three different surrogates for energy dissipation rate were defined. Each of the surrogates represents characteristics of either longitudinal, transverse, or asymmetric components. Note that due to the statistical isotropy and similarities between the gradients of different velocity components shown in §4.2.2, only the surrogates defined based on u_1 velocity are considered, unless it is mentioned otherwise. Instantaneous energy dissipation, ϵ_0, and its one-dimensional surrogates, $\tilde{\epsilon_0}$, are computed locally using DNS of isotropic turbulence, where the inherent assumptions in the surrogates are mostly valid. The statistical characteristics of the surrogates are compared with those of the direct measurements of energy dissipation rate and quantitative and qualitative differences are discussed. The effects of surrogates on intermittency estimations and potential biases are considered.

5.1 Analysis of the Local Energy Dissipation Rate and Surrogates

In this section, the characteristics of the local energy dissipation rate and its one-dimensional surrogates are studied. We start our analysis with a qualitative overview of the fields in Figure 5.1. The contour plots of horizontal cross section of energy dissipation and surrogates are shown. There are several striking characteristics evident in the images. The first relates to directionality. The dissipation rate and the surrogates are organized in slender structures having width and length of approximately λ and ℓ, respectively. These structures do not exhibit any directional preference in ϵ_0 while there is strong directional dependency in the longitudinal and transverse surrogates. The slender structures are oriented vertically for $\tilde{\epsilon}_{0,1}$ and horizontally for $\tilde{\epsilon}_{0,2}$. In other words the structures are perpendicular to the direction of the gradients used for computing the surrogates. Since it is composed of two gradients, $\tilde{\epsilon}_{0,3}$ does not exhibit strong directionality and has a smaller characteristic length scale. Also it is not positive definite.

The second difference between ϵ_0 and the surrogates evident in the images is that the surrogates exhibit much sharper gradients than ϵ_0. The images give the impression that the surrogates are more intermittent than ϵ_0, which is indeed the case as is shown quantitatively throughout this section.

5.1.1 Probability Density Functions

Next we consider the p.d.f.s of the local energy dissipation rate normalized by its mean, $\epsilon_0/\bar{\epsilon}$. These are plotted for each Re in the top panel of Figure 5.2. Energy dissipation rate is highly intermittent, as reflected in the pronounced tails of the distribution functions. The resolution of all the data sets are adequate for reliable measurements of energy dissipation, however, the far tails of p.d.f.s expand by Re. The larger simulation size and consequently extended dynamic range, increases the

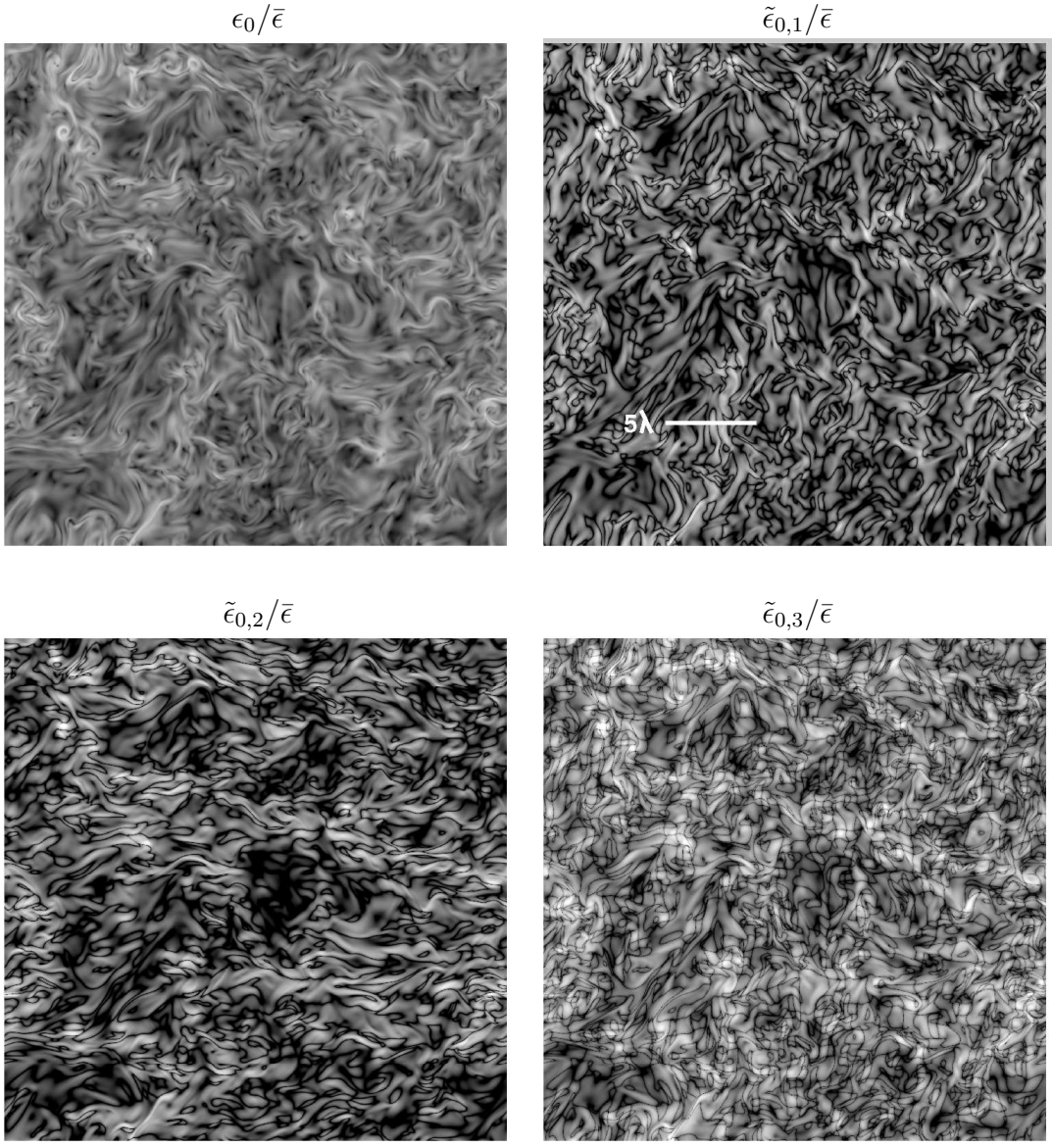

Figure 5.1: Dissipation rate and surrogates on an xy-plane from case R2. The x-direction is horizontal on the figures and a white line of length 5λ is shown in the upper right panel for reference. The shading is scaled logarithmically from 0.01 (black) to 100 (white) and is the same for all panels. The negative values in $\tilde{\epsilon}_3$ are shown as black.

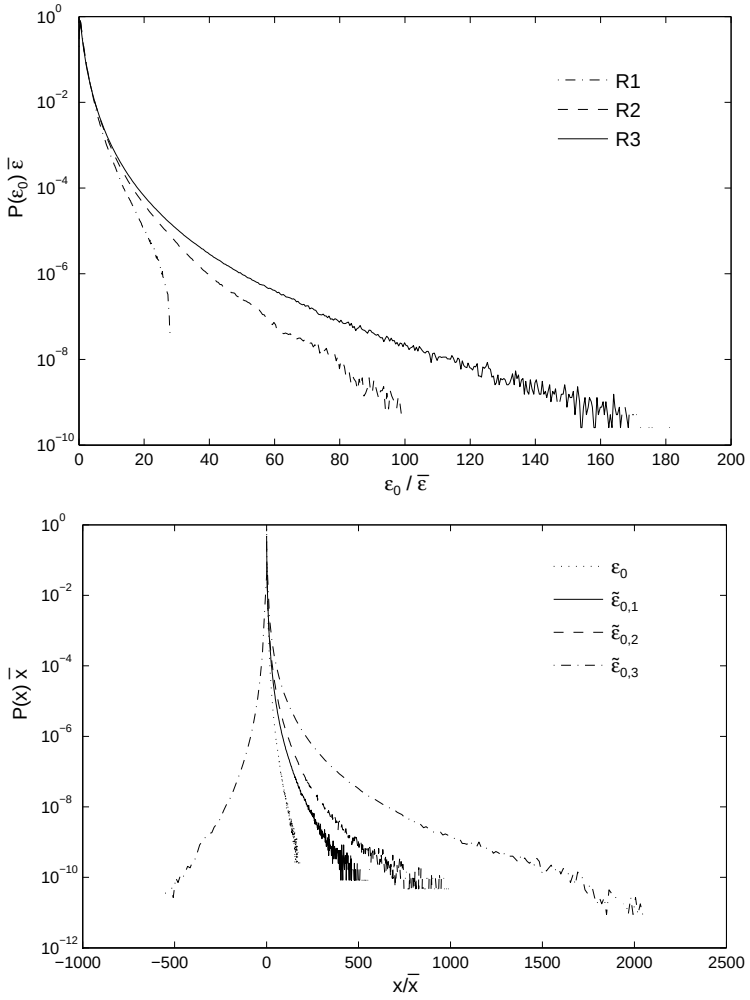

Figure 5.2: Top panel: p.d.f.s of the instantaneous energy dissipation rate normalized by its mean value for three Reynolds numbers. Bottom panel: p.d.f.s of dissipation rate surrogates for case R3 with x corresponding to each of the variables in the legend.

frequency of the intense and rare events. In case R3, the extreme values of ϵ_0 are more than 150 times the average value whereas the ratio is only about 30 for case R1. Note that the resolution in R1 and R2 simulations are similar but due to the higher Re and larger simulation domain of R2, energy dissipation exhibits significantly wider tail. In the literature, stretched exponential fits are suggested for the far tails of p.d.f.s of energy dissipation rate [see e.g. Bershadskii et al., 1993, Donzis et al., 2008, Meneveau and Poinsot, 1991].

The contour plots of the dissipation rate and surrogates (Figure 5.1) suggest that the surrogates are more intermittent than ϵ_0 and the results from §4.2.2 suggest that the transverse surrogate, $\tilde{\epsilon}_{0,2}$, will be more intermittent than the longitudinal surrogate, $\tilde{\epsilon}_{0,1}$. The p.d.f.s of the surrogates in the bottom panel of Figure 5.2 show both of these to be true. The transverse surrogate predicts dissipation rate values of more than 500 times the mean value compared with ratios of about 250 for the longitudinal surrogate and 150 for ϵ_0 itself. The p.d.f. of the asymmetric surrogate, $\tilde{\epsilon}_{0,3}$, has much different characteristics than those of either ϵ_0 or of the other surrogates both because $\tilde{\epsilon}_{0,3}$ is not positive definite and because it is extremely intermittent with a significant number of locations having values more than 1500 times the mean. The variance of this surrogate is also significantly higher than the other two surrogates. The numerical values of skewness and kurtosis of energy dissipation and its surrogates are listed in table 5.1 for all the cases. Consistent with the velocity derivatives, the transverse surrogate shows higher kurtosis than does the longitudinal surrogate.

Modelling energy dissipation rate and its distribution is the subject of ongoing research. The classical approach is to assume a lognormal distribution as suggested by Kolmogorov [1962] and Obukhov [1962]. This model is reviewed by Frisch [1995] and its shortcomings have been discussed previously [Kraichnan, 1974, Mandelbrot, 1974, Schertzer et al., 1997]. Here, we use the lognormal model as a reference when comparing the statistical characteristics of the surrogates with those of the energy

	Skewness			Kurtosis		
	R1	R2	R3	R1	R2	R3
ϵ	3.74	5.21	6.90	28.98	64.65	133.85
$\tilde{\epsilon}_2$	7.42	9.17	11.62	126.30	224.57	414.14
$\tilde{\epsilon}_2$	8.81	13.83	16.73	162.30	504.47	898.0
$\tilde{\epsilon}_3$	-7.15	-12.59	-16.01	144.19	526.65	997.24

Table 5.1: Skewness and kurtosis of local energy dissipation and its surrogates

	Skewness			Kurtosis		
	R1	R2	R3	R1	R2	R3
$\log \epsilon$	-0.20	-0.13	-0.10	3.14	3.09	3.11
$\log \tilde{\epsilon}_1$	-1.35	-1.29	-1.27	6.44	6.23	6.17
$\log \tilde{\epsilon}_2$	-1.19	-1.12	-1.10	5.87	5.65	5.59

Table 5.2: Skewness and kurtosis of the logarithm of the local energy dissipation rate and its surrogates.

dissipation rate. The p.d.f.s of the logarithm of the dissipation rate and its surrogates are plotted in Figure 5.3 along with the model distribution. The curves are scaled by the standard deviation of the logarithm of each variable, e.g., $\sigma_{\log \epsilon_0}$. The numerical values of skewness and kurtosis of these variables are listed in table 5.2 for all the cases. Consistent with the previous published data [e.g. Pope and Chen, 1990, Wang et al., 1996, Yeung et al., 2006a], the dissipation rate has a small negative skewness and slightly higher kurtosis than the model. Note that as discussed in §4.2.3 and §4.2.4 the statistical and anisotropy uncertainty for these statistics are negligible. Of greater interest in the current research are the p.d.f.s of the surrogates. The distributions of the surrogates are much different from that of the dissipation rate and the lognormal model is not appropriate even in the vicinity of the mean value.

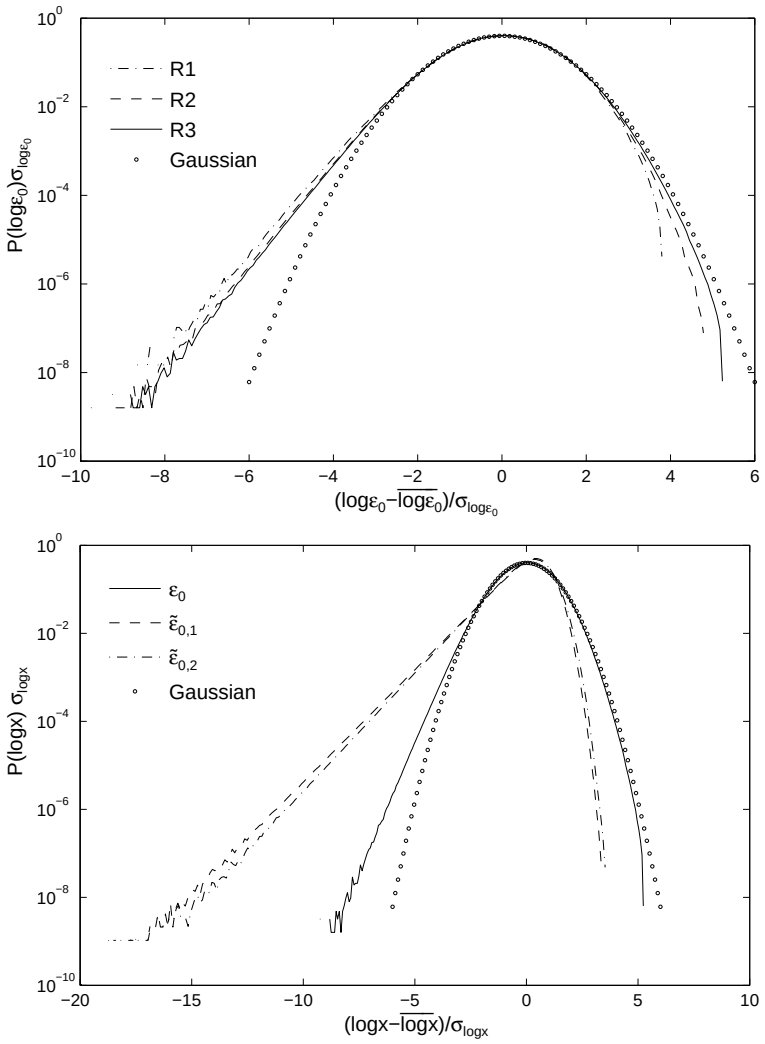

Figure 5.3: Top: Reynolds number effect on the p.d.f.s of logarithm of instantaneous energy dissipation in comparison to the Gaussian distribution. In the bottom panel the p.d.f. of logarithm of instantaneous energy dissipation and its surrogates are compared with Gaussian distribution for R3.

Based on the foregoing analyses several statistical differences between the energy dissipation rate and the surrogates have been observed. First, the mean dissipation rate computed from any of the surrogates will, by definition, be correct for isotropic flow. Second, higher moments of the dissipation rate fluctuations, and in general the probability density function of ϵ_0 are not well predicted by the surrogates. Third, the surrogates are more intermittent than ϵ_0 and intermittency is reflected in the higher moments of the p.d.f.s. Fourth, different surrogates exhibit different statistical characteristics including intermittency. The one-dimensional surrogates are directional statistics and could capture local characteristics of flow only in a particular direction, while the energy dissipation is a volumetric variable independent of direction. As a result, the sensitivity of the surrogates to the small scale anisotropy and the intermittency level predicted by each surrogate are different.

These results motivate a question about contribution of each component of strain rate tensor on the energy dissipation rate and its intermittency. We would like to determine the key mechanisms causing cancellation of the extreme events of surrogates in energy dissipation rate. It is hypothesized that either the extreme events of each component are partially canceled out by the competing events from the other components, or some of these mechanisms that contribute to the extreme events of a certain surrogates, would contribute less in the energy dissipation rate. To answer this question, the conditional statistics are applied and discussed in the next section. The effects of spatial averaging and cancellation of extreme events due to this averaging are discussed in terms of locally averaged statistics in §5.2.

5.1.2 Conditional Averages

In this section we examine the spatial correlation between energy dissipation and its surrogates to see whether the surrogates can provide good estimates of the dissipation rate if the infrequent events resulting from intermittency are omitted. For

this, consider the conditional average of the surrogate given $\epsilon_0 = \varepsilon$, where ε is the probability space analog of ϵ. As is often done, explicit reference to the probability space variable is omitted and we write the conditional average as, e.g., $\langle \tilde{\epsilon}_{0,1} | \epsilon_0 \rangle$.

The conditional averages of surrogates given the local energy dissipation rate are plotted in Figure 5.4 for R2 and R3. A line with slope one indicates the perfect correlation between the variables. For all values of ε, the longitudinal surrogate correctly predicts ϵ_0 on average. In other words, there is a strong spatial correlation between the longitudinal surrogate and the energy dissipation rate over all scales of fluctuations and the conditional p.d.f.s of the surrogate have very nearly the correct first moment for any value of ε. This is not the case for the other two surrogates. For both the transverse and asymmetric surrogates, the conditional average is too high for low values of ε and too low for high values of ε. There is no strong correlation between dissipation and these surrogates in regions of relative quiescence. For the moderate scales, the effect is more pronounced for the asymmetric surrogate presumably because it can have negative values even in locations where ϵ_0 is high.

Only one surrogate of each type is shown in Figure 5.4. It has been observed, however, that summing independent intermittent random fields will result in a less intermittent field and so the sum of, say, two different transverse surrogates may result in a surrogate with statistics closer to those of ϵ_0 [Wang et al., 1996]. This suggests looking at the conditional averages of the sum of all the possible transverse surrogates as done by Donzis et al. [2008]. The conditional averages of the sum of the transverse surrogates is similar to the conditional average of a single surrogate. Summing the surrogates to reduce the intermittency does not result in the conditional average agreeing with the dissipation rate.

The reverse conditional statistics, i.e., the conditional averages of instantaneous energy dissipation given surrogates does not show the same behavior. At low values of surrogates the conditional dependency is weak, but it increases for moderate and

extreme events. It is always below the line of slope one, indicating that the moderate and extreme events of surrogates are usually followed by lower energy dissipation rate. In other words extreme events of surrogates are partially canceled out by each other. The deviation is much higher in the transverse compared with the longitudinal surrogate. Note that the resolution effect is negligible and the conditional statistics of R2 and R3 are very close.

5.2 Analysis of the Locally Averaged Surrogates

Thus far, our analysis has been focused on the local dissipation rate, ϵ_0, and the corresponding surrogates. A principal motivation for studying surrogates, however, is to understand how they might bias our understanding of intermittency. Intermittency is quantified by how the dissipation rate varies in space and so we turn now to analyzing the locally averaged dissipation rate, ϵ_r, and its surrogates.

The locally averaged dissipation rate is defined as ϵ_0 averaged over a volume with *linear* dimension r. In theoretical analyses of isotropic turbulence the averaging volume is taken to be a sphere but the definition of r is not consistent in the literature. The original definition in Kolmogorov [1962] takes r to be the radius of the sphere [e.g. Frisch, 1995, Kolmogorov, 1962, Novikov and Stewart, 1964, Pope, 2000], while r is also defined as the diameter of the sphere in some references [e.g. Chen et al., 1993, Monin and Yaglom, 1975, Stolovitzky et al., 1992, Thoroddsen, 1995, Wang et al., 1996]. In this paper the second definition is used because, as explained in the next paragraph, we consider averages over spheres and also along straight lines. So for the analyses that follow, r is the linear dimension of the averaging volume and ϵ_r is

$$\epsilon_r(\boldsymbol{x}) = \frac{6}{\pi r^3} \int\int\int_{V(r)} \epsilon_0(\boldsymbol{x} + \boldsymbol{r})\, d\boldsymbol{r}. \tag{5.1}$$

With simulation data, the dissipation rate and the surrogates are known as functions of three spatial dimensions and so the spherical averages can be computed.

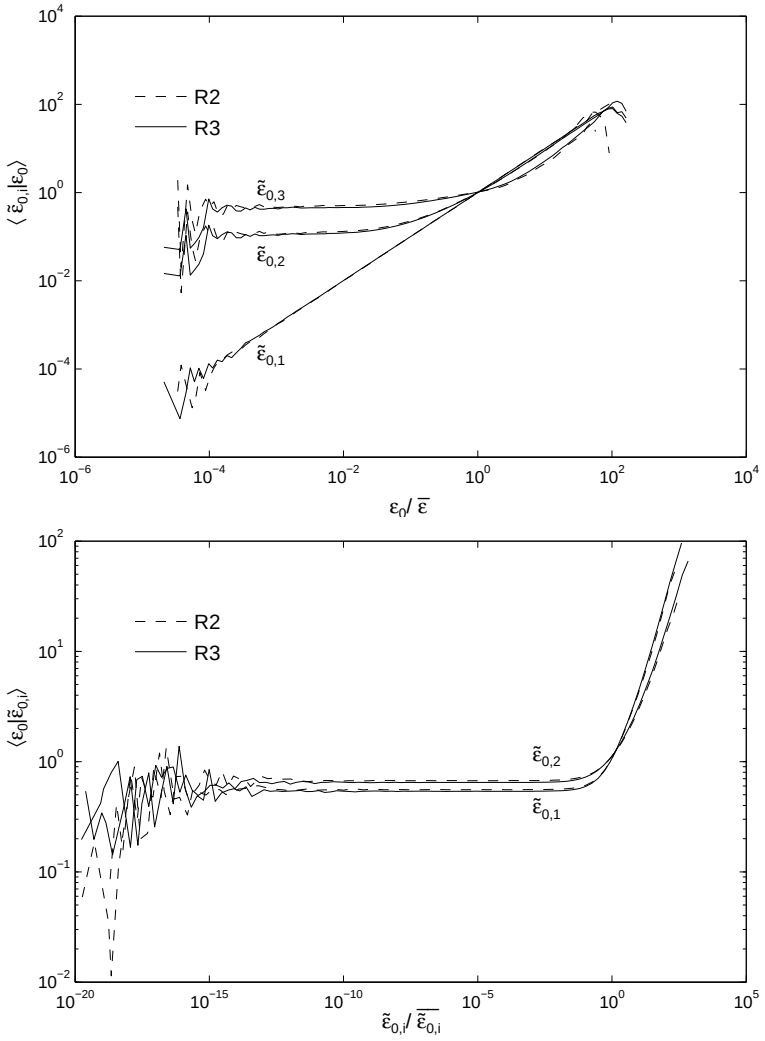

Figure 5.4: Conditional (top) and reverse conditional (bottom) averages of instantaneous energy dissipation surrogates and energy dissipation for R2 and R3.

When the surrogates are measured in a physical flow, however, typically they are sampled in time and Taylor's hypothesis is invoked to convert the time series to a spatial series. In this case, the surrogate is only known along a line and it is natural to compute the local averages along that line, not over a sphere. Thus, intermittency estimates based on surrogates will be affected both by differences between ϵ_0 and the surrogates and by differences between the averaging volume inherent in the definition of ϵ_r and that used to average the surrogates. In this study we consider the two effects separately. To make clear the averaging volume used to compute a given quantity, the subscript "r" indicates an average over a sphere of diameter r, e.g., $\tilde{\epsilon}_{r,1}$, and the subscript "h" indicates an average along a line of length h, e.g., $\tilde{\epsilon}_{h,1}$.

A further comment is warranted with regards to computing local averages from simulation data. In general, given ϵ_0 at discrete location in space, interpolation must be used to compute an average over an arbitrary region. If the interpolation scheme is not fully consistent with the numerical method used to solve the governing equations when the simulation was run then errors will result. Fortunately, with data from a pseudo-spectral simulation the interpolation function is known exactly. For the spherical filter, ϵ_r is exactly

$$\epsilon_r(\boldsymbol{x}) = \bar{\epsilon} + 3 \iiint_{-\infty}^{\infty} e^{i\boldsymbol{\kappa}\cdot\boldsymbol{x}} \hat{\epsilon}_0(\boldsymbol{\kappa}) \left(\frac{\sin(\kappa r/2)}{\kappa^3 (r/2)^3} - \frac{\cos(\kappa r/2)}{\kappa^2 (r/2)^2} \right) d\boldsymbol{\kappa}, \tag{5.2}$$

where $\hat{\epsilon}_0$ is the three-dimensional Fourier transform of ϵ_0 fluctuations. For the linear filter in the x_i direction,

$$\epsilon_h(\boldsymbol{x}) = \bar{\epsilon} + \int_{-\infty}^{\infty} e^{i\kappa_i x_i} \hat{\epsilon}_0(\boldsymbol{\kappa}) \frac{\sin(\kappa_i h/2)}{\kappa_i h/2} \, d\kappa_i. \tag{5.3}$$

where κ_i is the wave number in the i-th direction. More information on these averages is provided in Appendix B.

It is sometimes noted that (5.2) and (5.3) are not, in general, exact for simulation data, which is true if ϵ_0 cannot be exactly represented in Fourier space by $\hat{\epsilon}_0$. In fully dealiased pseudospectral simulations of the type reported here, ϵ_0 is described exactly by a finite discrete Fourier series and, therefore, by a Fourier integral with the coefficient function zero except at certain wave numbers. Since (5.2) and (5.3) do not introduce Fourier modes that are not in ϵ_0, ϵ_r and ϵ_h reported here are exact to within the precision of the computer arithmetic.

5.2.1 Probability Density Functions

To guide our analysis of the the locally averaged surrogates, we pose two questions motivated by the results from §5.1. First, does spatial averaging result in the fortuitous cancellation of the excessive intermittency of the surrogates, relative to that in ϵ_0, so that the moments of the averaged surrogates are comparable to those of ϵ_r? Second, is the lognormal model, often used in estimating the intermittency exponent, appropriate for the locally averaged surrogates even though it is not a good model for the local quantities? To address the first of these questions, the p.d.f.s of ϵ_r and the two positive-definite surrogates are plotted in Figure 5.5 for case R2 and r ranging from the Kolmogorov to the integral length scales.

Note that the curve for the highest r is plotted true and the remaining curves are offset vertically in increments of half a decade so that they can be distinguished. Based on the data in table 4.1 and figures 4.8 and 4.10, the curves for $r = 21\eta \approx \lambda$ and $r = 169\eta \approx \ell$ are representative of the variables averaged over scales in the scaling range and the energy containing range, respectively.

Consider first the general shape of the curves. For small r, the results are as expected from the preceding analysis of the local dissipation rate. The transverse surrogate exhibits higher frequency of extreme events than the longitudinal surrogate, but both surrogates exhibit significantly heavier tails compared with ϵ_r. Only for

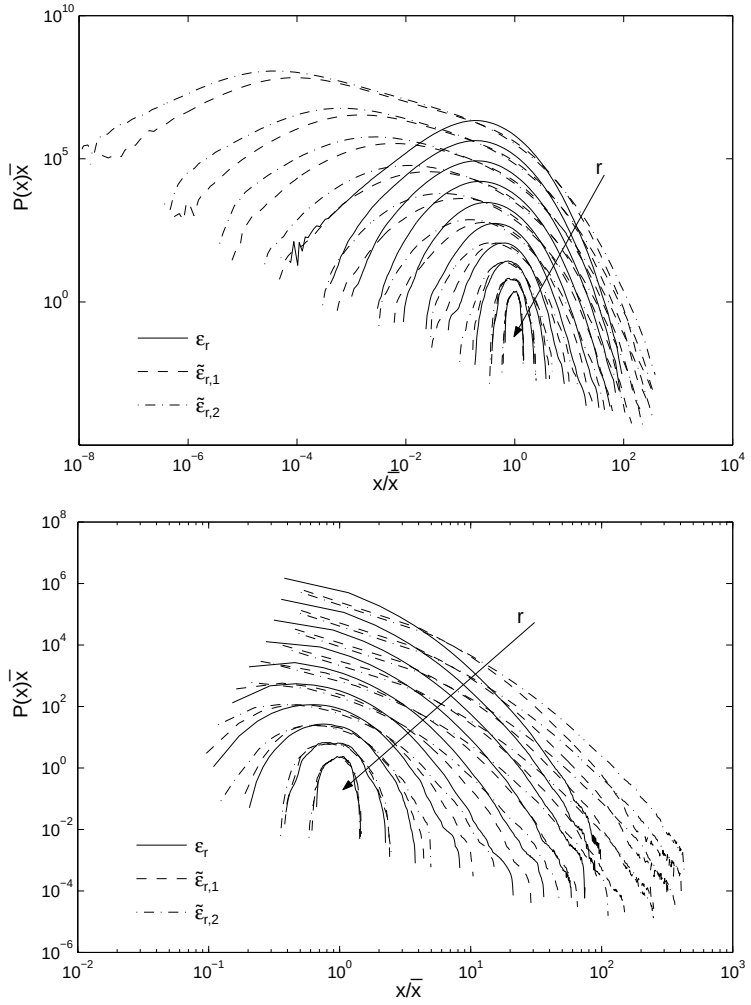

Figure 5.5: P.d.f.s of the locally averaged energy dissipation rate and the longitudinal and transverse surrogates for case R2 and $r/\eta = 0.7$, 1.3, 2.6, 5.3, 11, 21, 42, 84, 169, 337. Variables are normalized by their own mean, r increases in the the direction of the arrow, and x corresponds to each of the variables in the legend. The curve for the highest r is plotted true and the remaining curves are offset vertically in increments of half a decade. The p.d.f.s are calculated with bins of equal width in logarithm (top) and linear (bottom) scales.

averaging over the energy containing scales do the dissipation rate and the surrogates have similar distributions. The characteristics of the p.d.f.s are further quantified in terms of their centered-normalized moments, which are plotted as functions of r in Figure 5.6.

The moments are computed for all possible components over three different orthogonal directions. The averaged value for the longitudinal, transverse, and asymmetric surrogates are shown in the figure. Error bars, which are obtained by estimating the residual anisotropy from the fluctuations between measurements on three orthogonal directions, are smaller than the symbol size in the figures. The moments are nearly invariant with r in the dissipation range. For higher r, the moments decrease approximately as power laws and only for averaging over lengths characteristic of the energy containing scales are the moments of surrogates comparable with those of energy dissipation rate. The differences between the longitudinal and transverse surrogates preserve even when the fields are locally averaged over lengths in the scaling range.

Next we determine if the lognormal model is reasonable for the averaged surrogates. In Figure 5.7, the p.d.f.s of the logarithm of the locally averaged energy dissipation, longitudinal, and transverse surrogates are shown. The asymmetric surrogate is not necessarily positive and so its logarithm is not considered. In computing the p.d.f.s, the mean of each variable has been subtracted and the result normalized by its own standard deviation, e.g., $\sigma_{\log \epsilon_r}$, for comparison with the lognormal model. A wide range of r values are included in the top panel of the figure while the lower panel is a magnified version showing r in the scaling range and larger. In the bottom panel, dotted lines indicate the lognormal model. There is fairly good agreement between logarithm of the locally averaged energy dissipation rate and its surrogates for r in the scaling range and larger.

The suitability of the lognormal model for the surrogates is explored via the skewness and kurtosis of each distribution, which are plotted in Figure 5.8. The magnitude

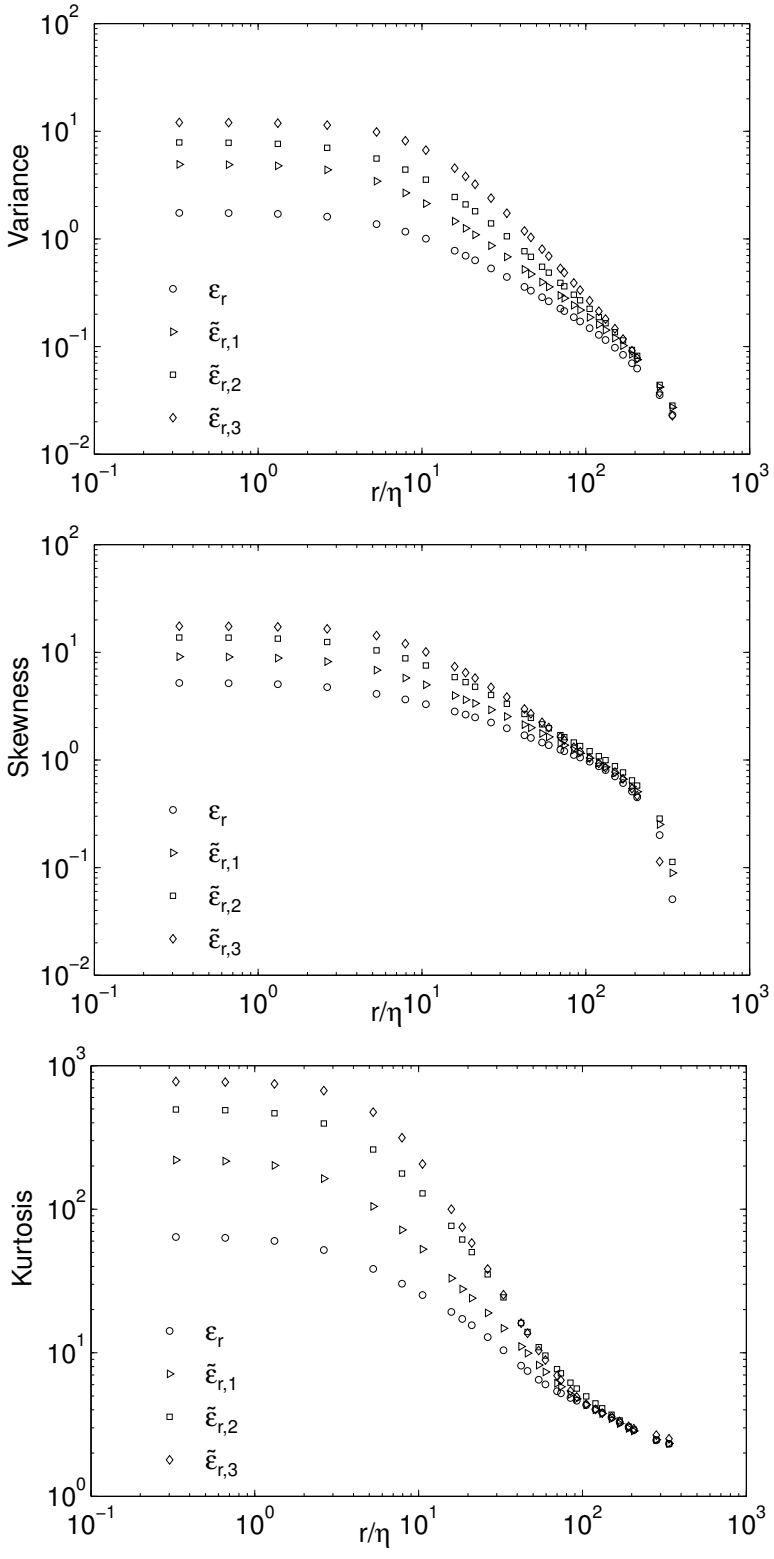

Figure 5.6: The variance, skewness, and kurtosis of the locally averaged energy dissipation rate and surrogates.

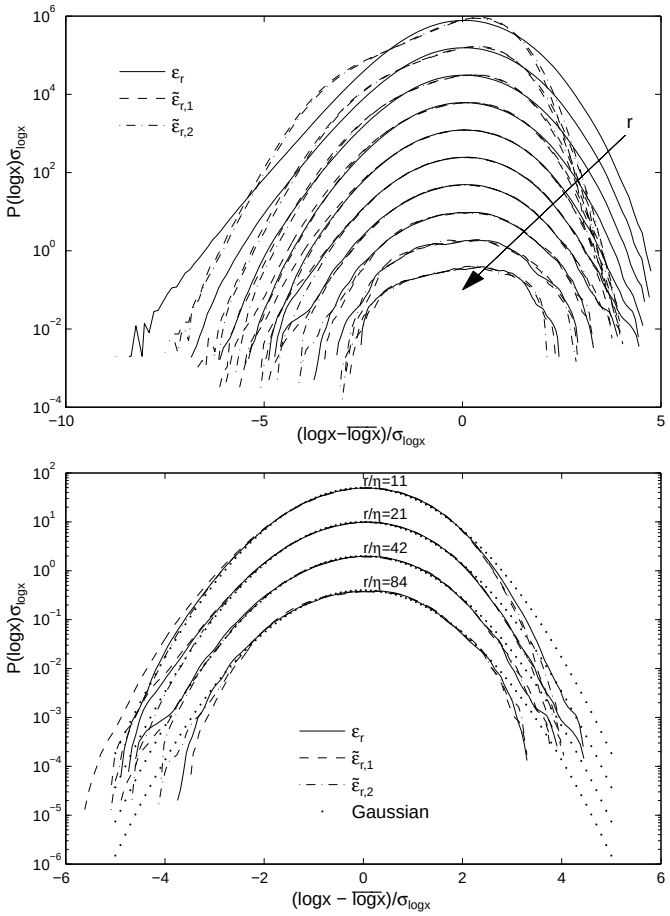

Figure 5.7: Top panel: p.d.f.s of the logarithm of the locally averaged energy dissipation rate and the longitudinal and transverse surrogates for $r/\eta = 0.7$, 1.3, 2.6, 5.3, 11, 21, 42, 84, 169, 337. Bottom panel: A magnified view of the same data for r/η in the scaling range. In both panels, the curve for the highest r is plotted true and the remaining curves are offset vertically in increments of half a decade and x corresponds to each of the variables in the legend.

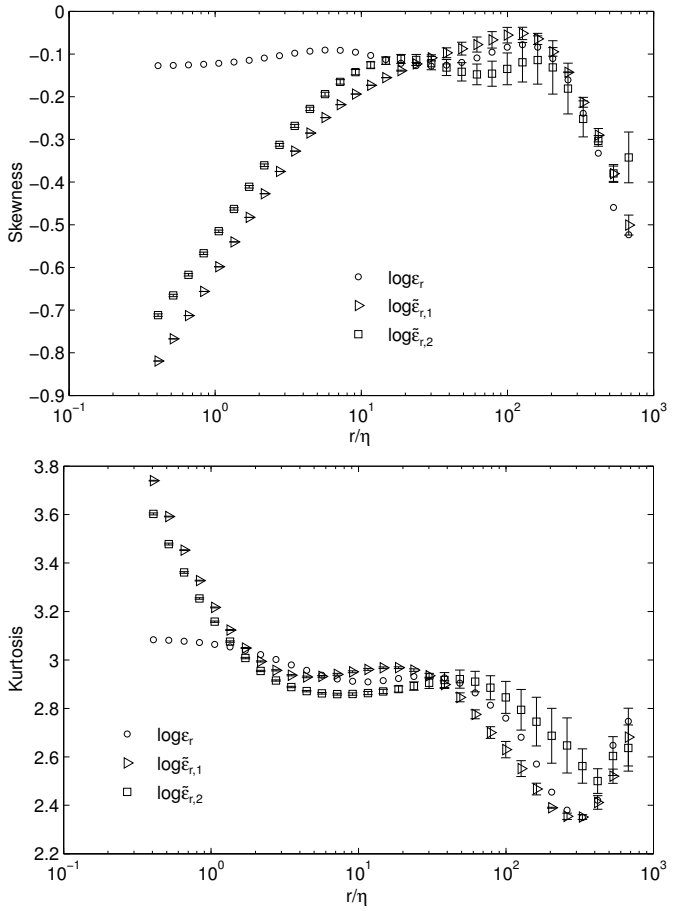

Figure 5.8: The skewness and kurtosis of the logarithm of the locally averaged energy dissipation rate and surrogates. Error bars indicate uncertainty due to residual anisotropy estimated from the fluctuations between measurements on three orthogonal directions.

of the moments decrease with increasing r in the dissipation range but are roughly constant for r in the scaling range. In the scaling range, the skewness and kurtosis values suggest distributions close to lognormal, but there is a distinct bias toward negative skewness, which is consistent with the results of Wang et al. [1996]. Perhaps surprisingly given Figure 5.7, the lognormal function represents the locally averaged surrogates fairly well for r in the scaling range and larger.

5.2.2 Conditional averages

Even though there are significant differences between intense events of the local dissipation rate and its surrogates, canceling of extreme values of the longitudinal surrogate result in $\langle \tilde{\epsilon}_{0,1} | \epsilon_0 \rangle \approx \epsilon_0$ for all values of ϵ_0 (c.f. Figure 5.4). This is not the case for the other surrogates. Now consider the cancellation of extreme events through a combination of spatial and conditional averaging. In Figure 5.9, the surrogates conditioned on ϵ_r are shown for the full range of r values in the simulations. The curves for small r are not surprising given that it has been shown earlier that neither spatial averaging nor conditional averaging of the transverse or asymmetric surrogates result in cancellation of extreme events. For r in the scaling range and smaller, only the longitudinal surrogate exhibits conditional averages approximately equal to ϵ_r. Values of r near the integral length scale are required for the transverse and asymmetric surrogates to do likewise. This result is remarkable because the spatial averages of the surrogates and the dissipation rate are equal for $r = \mathcal{L}$.

The reverse conditional expectations, i.e., averaged energy dissipation conditioned on given surrogate show different pattern. There is a weak correlation at small fluctuations while it gets stronger for moderate and large fluctuations. The correlation coefficient, however is less than perfect for all the scales of averaging. In other words, energy dissipation always underestimates longitudinal and transverse surrogates and locally averaging these variables does not change this behavior. The deviation is

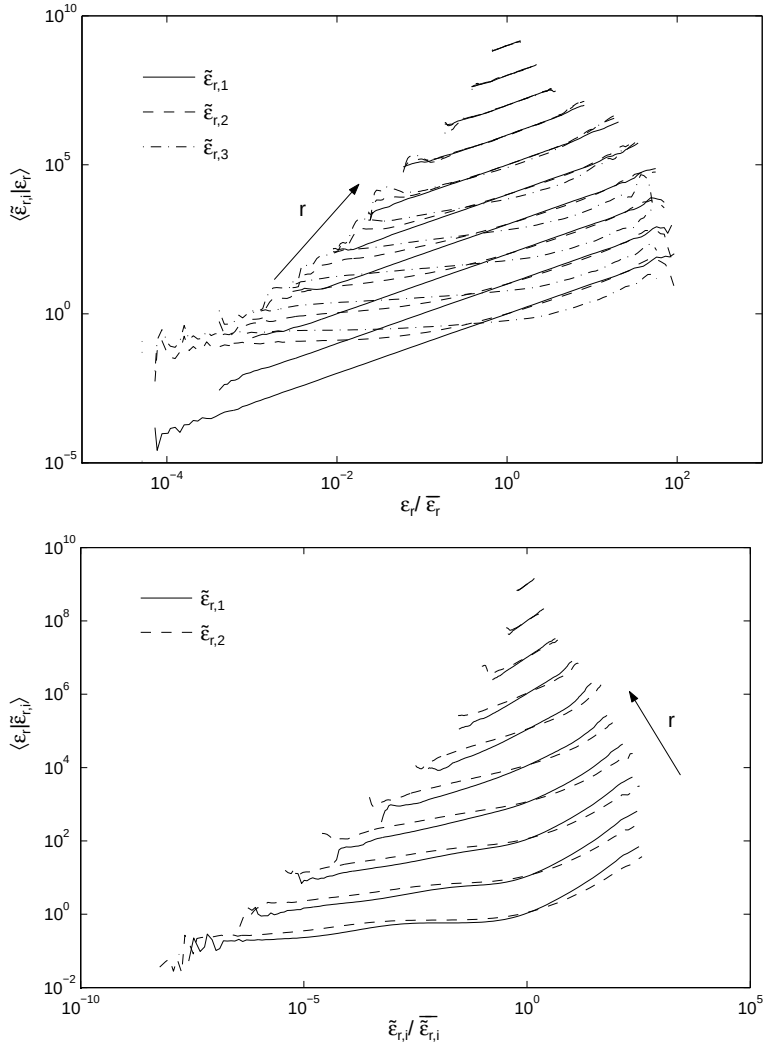

Figure 5.9: Conditional (top) and reverse conditional (bottom) expectation of the surrogates given the locally averaged energy dissipation rate for $r/\eta = 0.7$, 1.3, 2.6, 5.3, 11, 21, 42, 84, 169, 337. The curves for the lowest value of r are plotted true and the remaining curves are offset in increments of a decade. The arrow direction indicates increasing r.

stronger for asymmetric and transverse surrogates. Therefore, unless r is close to the integral length scale, the spatial correlation of locally averaged energy dissipation and its surrogates are similar to the instantaneous variables.

5.3 Quantifying Intermittency

Intermittency is quantified in terms of the scale dependency of the higher moments of ϵ_r. The theory of K62 includes the assumption of large scale separation between ℓ and η. Unfortunately, only the surrogates are available for flows with large scale separation. So the objective in this section is to use the DNS data to show how intermittency metrics computed from the surrogates can be expected to deviate from the exact values computed directly from ϵ_r. Because of the limited dynamic range in DNS, no suggestion is made that it can be used to validate theories on intermittency.

5.3.1 Scale Dependency of Moments

We begin our analyses with the second-order moments of the locally averaged energy dissipation rate and the surrogates. The moments are computed for all possible components over three different orthogonal directions. The averaged value for the longitudinal, transverse, and asymmetric surrogates are shown in the top panel of Figure 5.10 for case R2. The data in the figure is the same as in Figure 5.5 but now the second-order moment, not the variance, is shown. The error bars represent uncertainty due to the residual anisotropy estimated from the fluctuations between statistics on three orthogonal directions. The curves in the scaling range are approximately a power law for all the variables.

In order to evaluate power law scaling, as suggested by Miller and Dimotakis [1991], the local scaling exponents

$$\tau(n,r) \equiv -\frac{d(\log\langle\epsilon_r^n\rangle)}{d\log r}$$

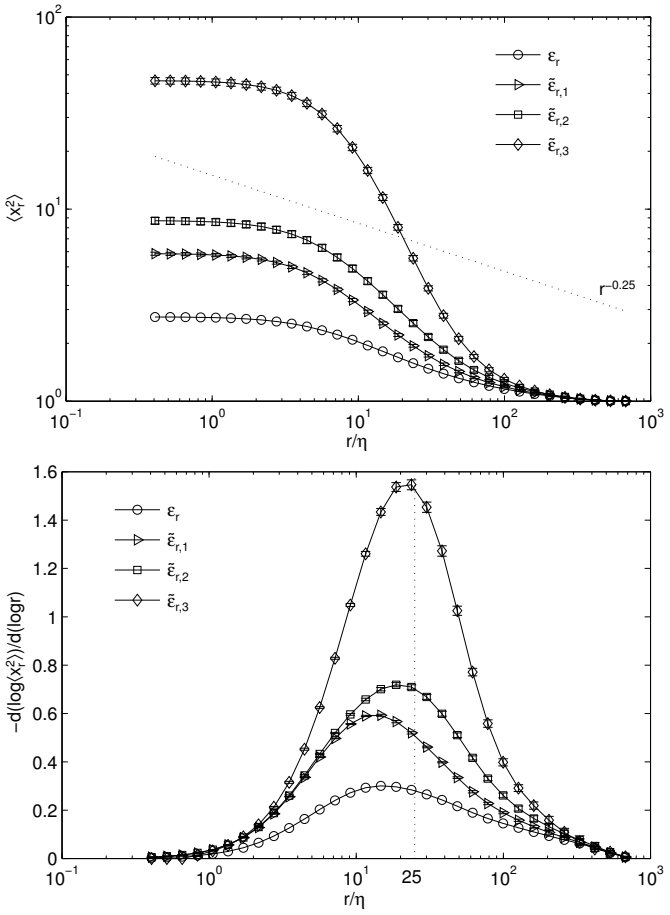

Figure 5.10: The second-order moments (top panel) and corresponding slopes (bottom panel) of the locally averaged energy dissipation rate and surrogates for R2. Error bars indicate uncertainty due to the residual anisotropy estimated from the fluctuations between statistics on three orthogonal directions.

and

$$\tilde{\tau}_i(n,r) \equiv -\frac{d(\log\langle\tilde{\epsilon}^n_{r,i}\rangle)}{d\log r}, \qquad i = 1,2,3$$

are plotted in the bottom panels of Figure 5.10. Recall that the intermittency exponent, μ, is defined as $\tau(2,r)$ for r in the scaling range. A vertical dotted line at $r = 25\eta \approx \lambda$ is shown on the plots to aid in reading the logarithmic scales. The curves reveal no broad range of r with power law scaling and the local scaling exponent decreases monotonically over the scaling range for all the variables. This result is consistent with the high Reynolds number experimental measurements and atmospheric observations of Praskovsky and Oncley [1997] and so is presumably not an artifact of the limited dynamic range of the simulations. Additionally, the numerical values of the local slopes from the longitudinal surrogate are consistent with those reported in this reference. Of greater interest in the current study is that the local scaling exponents are much higher for the surrogates than the energy dissipation rate, which means that the surrogates greatly overestimates the intermittency exponent if a one-for-one replacement is made of the dissipation rate with the surrogate. Similar results have been reported by, e.g., Wang et al. [1996], Zhou et al. [2006].

The third- and fourth-order moments and corresponding slopes are also computed in a similar method to the second-order moments and plotted in Figure 5.11. The error bars are more pronounced at higher-order moments, however, still negligible compared with the discrepancy between the statistics of energy dissipation rate and surrogates. The reference slopes corresponding to $\mu = 0.25$ and assuming the lognormal model are included on the plots to help the reader judge the slopes of the curves. The local scaling exponents of these curves averaged over the scaling range are listed in table 5.3 for both R2 and R3. The uncertainty reported in this table is due to the variation of the local scaling exponents over the scaling range. It indicates fluctuations of the averaged scaling exponents induced by the scaling range extension. The effect of uncertainty is dwarfed by the discrepancy between the statistics of energy dissipation

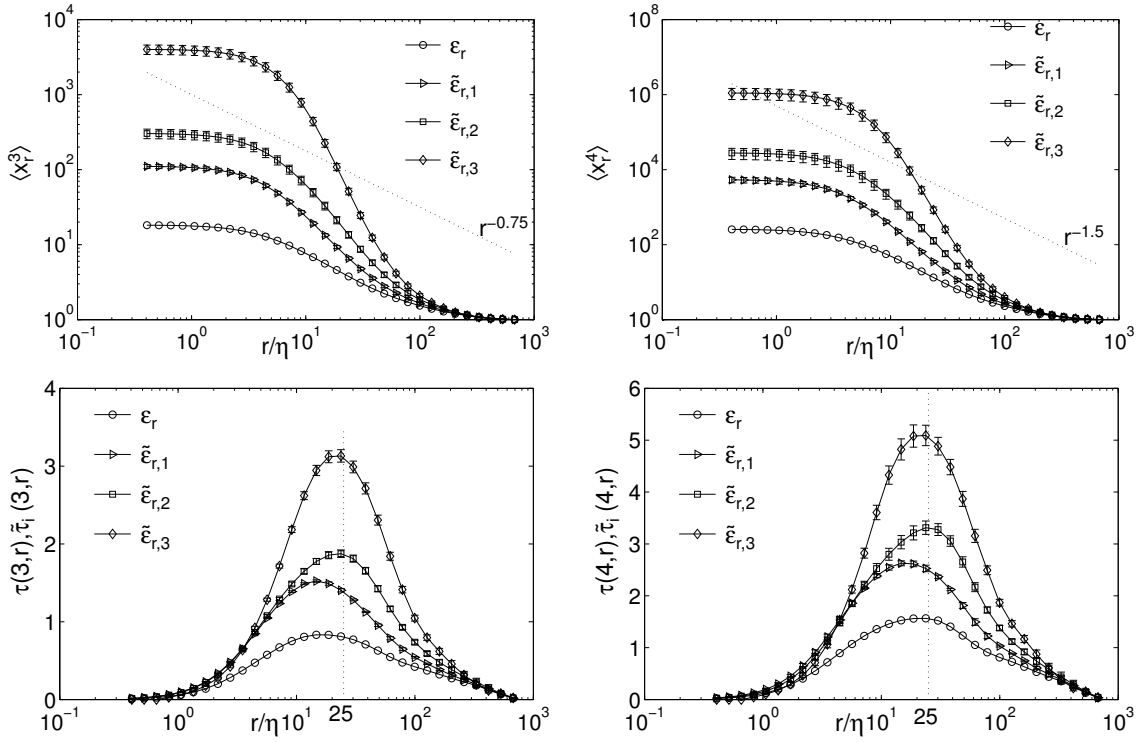

Figure 5.11: The third- and fourth-order moments of the locally averaged energy dissipation rate and longitudinal, transverse, and asymmetric surrogates over a range of r. The dotted lines are for reference in estimating slopes and x corresponds to each of the variables on the plot. The bottom panels are the corresponding local slopes. The uncertainty due to anisotropy is indicated by the error bars.

rate and surrogates. Regardless of which moment or which simulation is considered, the longitudinal surrogate yields significantly higher $\tau(n, r)$ for r in the scaling range than does ϵ_r, and the transverse and asymmetric surrogates yield even higher values. Note that in the reminder of this section the error bars are neglected to simplify the figures.

A wide range of values for the intermittency exponent has been reported in the literature, in part due to multiple methods used for computing it; see for example the reviews by Monin and Yaglom [1975], Praskovsky and Oncley [1997], Sreenivasan and Antonia [1997], Sreenivasan and Kailasnath [1993]. The textbook value is $\mu = 0.25 \pm 0.05$ [Pope, 2000, Sreenivasan and Antonia, 1997] and the scaling exponents of

	n	ϵ_r	$\tilde{\epsilon}_{r,1}$	$\tilde{\epsilon}_{r,2}$	$\tilde{\epsilon}_{r,3}$
	2	0.23 ± 0.03	0.38 ± 0.04	0.56 ± 0.04	1.16 ± 0.17
R2	3	0.67 ± 0.10	1.06 ± 0.12	1.53 ± 0.11	2.50 ± 0.28
	4	1.32 ± 0.20	1.99 ± 0.22	2.81 ± 0.19	4.15 ± 0.43
	2	0.23 ± 0.03	0.34 ± 0.04	0.51 ± 0.05	1.43 ± 0.10
R3	3	0.68 ± 0.08	0.99 ± 0.11	1.41 ± 0.11	3.00 ± 0.25
	4	1.35 ± 0.12	1.86 ± 0.17	2.59 ± 0.18	5.047 ± 0.61

Table 5.3: The averaged local scaling exponent of the energy dissipation rate and surrogates for nth-order moments. The uncertainty due to changes in the scaling range is indicated by the error bars.

ϵ_r in table 5.3 are in this range. All of the surrogates, however, over-predict μ. This is consistent with the results in §5.1 and §5.2, namely that the surrogates are more intermittent than the dissipation rate itself and averaging at length scales larger than the scaling range is required to make the intermittency in the surrogates comparable to that in the dissipation rate.

5.3.2 Testing for a Correctable Bias

The preceding results show that the one-dimensional surrogates significantly overestimate the intermittency exponent if ϵ_0 is simply replaced by a surrogate in the calculations. If the bias is predictable, however, then it might be corrected for. One approach to computing the bias [e.g. Benzi et al., 1993, Chen et al., 1997b] is to assume power law scaling for both $\langle \epsilon_r^n \rangle$ and $\langle \tilde{\epsilon}_{r,i}^n \rangle$, i.e.,

$$\langle \epsilon_r^n \rangle \sim r^{\tau(n,r)}, \ \langle \tilde{\epsilon}_{r,i}^n \rangle \sim r^{\tilde{\tau}_i(n,r)}, \tag{5.4}$$

so that

$$\langle \tilde{\epsilon}_{r,i}^n \rangle \sim \langle \epsilon_r^n \rangle^{\frac{\tilde{\tau}_i(n,r)}{\tau(n,r)}} = \langle \epsilon_r^n \rangle^{\tau_i'(n)}. \tag{5.5}$$

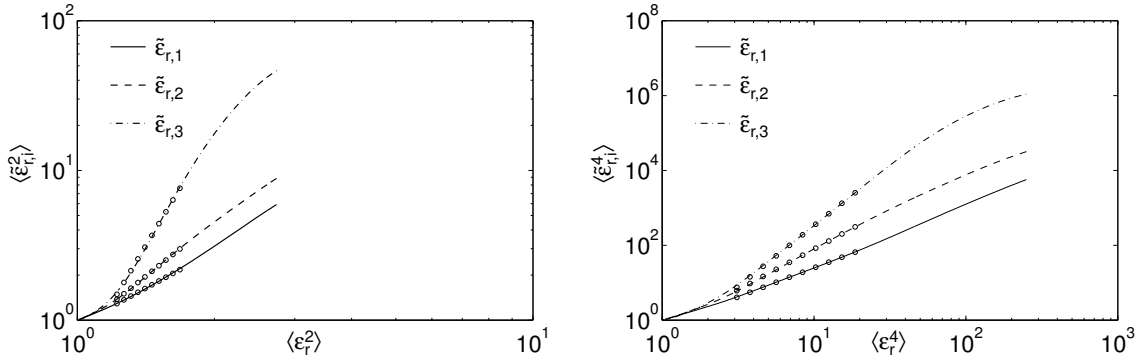

Figure 5.12: $\left\langle \tilde{\epsilon}^n_{r,i} \right\rangle$ as a function of $\langle \epsilon^n_r \rangle$ for n=2,4. The circles on each curve represent the best power law fit to the curve in the scaling range from table 5.4.

	R2			R3		
n	$\tilde{\epsilon}_{r,1}$	$\tilde{\epsilon}_{r,2}$	$\tilde{\epsilon}_{r,3}$	$\tilde{\epsilon}_{r,1}$	$\tilde{\epsilon}_{r,2}$	$\tilde{\epsilon}_{r,3}$
2	1.60 ± 0.01	2.38 ± 0.04	4.90 ± 0.09	1.47 ± 0.004	2.16 ± 0.02	4.50 ± 0.06
3	1.56 ± 0.02	2.26 ± 0.06	3.82 ± 0.09	1.42 ± 0.001	2.03 ± 0.02	3.52 ± 0.07
4	1.49 ± 0.02	2.12 ± 0.07	3.21 ± 0.13	1.36 ± 0.009	1.99 ± 0.04	3.14 ± 0.08

Table 5.4: Scaling exponent $\tau'_i(n)$ in $\left\langle \tilde{\epsilon}^n_{r,i} \right\rangle \sim \langle \epsilon^n_r \rangle^{\tau'_i(n)}$ for the three surrogates and n=2,3,4. The error bars indicate the uncertainty due to anisotropy and changes in the scaling range.

In the range of r where power law scaling occurs, $\tau'_i(n)$ is not a function of r, hence the omission of r from the notation. To test the efficacy of this approach, $\langle \tilde{\epsilon}^n_{r,i} \rangle$ is plotted versus $\langle \epsilon^n_r \rangle$ in Figure 5.12 for case R2 and n =2 and 4.

The numerical values of the exponents computed by minimizing the sum, for r in the scaling range, of the square of the differences between the data and the power law are listed in table 5.4 for R2 and R3. The results show that the biases in the longitudinal and transverse surrogates are fairly consistent for all moments. For instance, the $\tau'_1(n) \approx 1.5$ and $\tau'_2(n) \approx 2.2$ for n up to 4. Given the behaviour of the asymmetric surrogate reported in §5.1 and §5.2, it is not surprising that $\tau'_3(n)$ is not approximately constant.

5.3.3 Effect of the Averaging Volume

At the beginning of §5.2, it is observed that the averaging volume envisioned in K62 is a sphere of diameter r whereas it is natural to average the surrogates along a line of length h. The effect of the choice of averaging volume is examined with the help of Figure 5.13 in which the dissipation rate and the surrogates are averaged both ways for case R2. Linear averaging results in lower values of $\tau(n, r)$ for small r and higher values of $\tau(n, r)$ at large r. Quite remarkably, the cross over point is at r at the scaling range. Similar behavior is observed for the surrogates. Therefore, the tendency of the intermittency exponent estimated from the surrogates to be too high is partially counteracted by the averaging technique typically used with surrogates. Even so, the intermittency exponent based on $\tilde{\epsilon}_{h,1}$ is still too high and the estimates from the other surrogates are even higher.

5.3.4 Other Methods for Estimating the Intermittency Exponent

It has been suggested that in homogeneous turbulence the intermittency exponent can be obtained from the autocorrelation function of the local dissipation rate by relating it to $\langle \epsilon_r^2 \rangle$ in the scaling range [Monin and Yaglom, 1975, §25]. The autocorrelation function of the local energy dissipation rate and of the longitudinal, and transverse surrogates are defined as:

$$R_{\epsilon_0}(r) \equiv \langle \epsilon_0(\boldsymbol{x}) \epsilon_0(\boldsymbol{x} + \boldsymbol{r}) \rangle \ , \tag{5.6}$$

$$R_{\epsilon_{0,i}}(r) \equiv \langle \tilde{\epsilon}_{0,i}(\boldsymbol{x}) \tilde{\epsilon}_{0,i}(\boldsymbol{x} + r_i) \rangle, \quad i = 1, 2. \tag{5.7}$$

They are plotted versus separation distance in the top panel of Figure 5.14 for case R2. The second-order moments of the locally averaged energy dissipation rate and surrogates, for both linear and spherical averaging, are also shown in the same figure. Note that the autocorrelation functions are shifted in the vertical direction for illustration purposes.

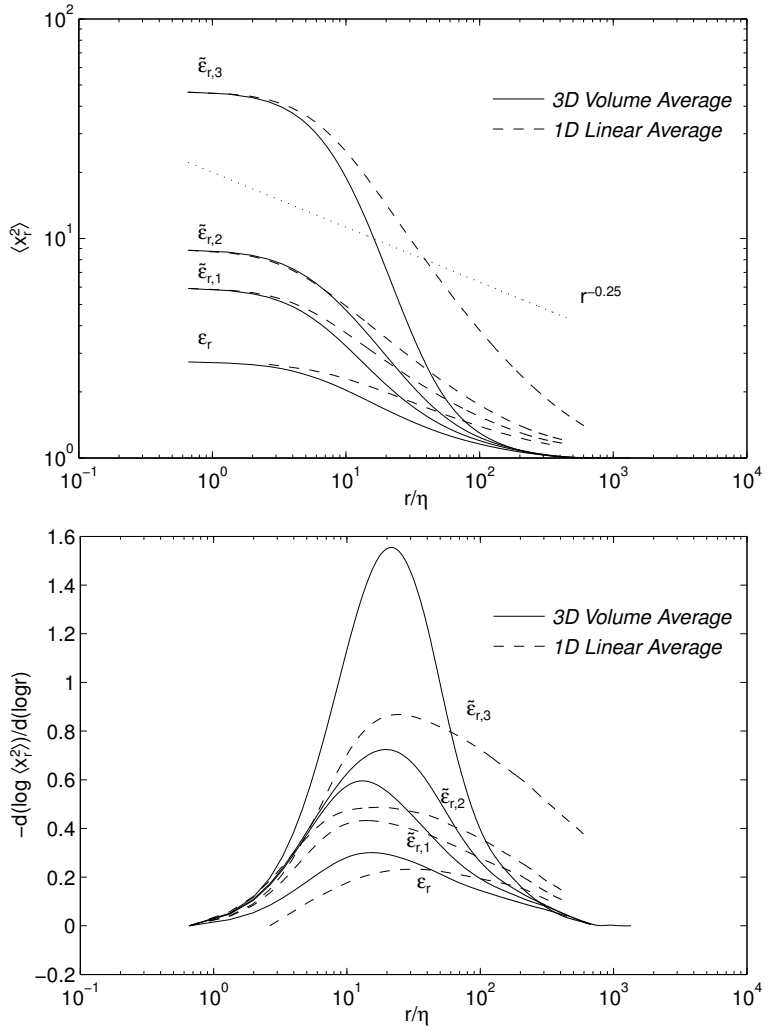

Figure 5.13: The second-order moments (top panel) and corresponding power law exponent (bottom panel) of the locally averaged dissipation rate and surrogates using both volume and linear averaging. x corresponds to each of the variables on the plot.

Considering first the characteristics of the autocorrelation functions, it is apparent that they exhibit power law scaling at values of r in the scaling range. Additionally, at these separation distances the autocorrelation function of the longitudinal surrogate is similar to that of the dissipation rate itself. The autocorrelation function of the transverse surrogate, on the other hand, does not behave like that of the dissipation rate except perhaps at larger length scales.

Next consider whether the autocorrelation functions yield the same value of μ as the local averages do. Recall that in the top panel of Figure 5.14 the autocorrelation functions are offset vertically for clarity of the figure. Removing the offset by eye, it is apparent that the autocorrelation and local average curves will not align and that the autocorrelation functions lie to the left from the average curves. If the averaging volume for ϵ_r is defined in terms of the radius instead of the diameter, as is done by, e.g., Frisch [1995], Kolmogorov [1962], Pope [2000] (c.f.§5.2), then there is very good agreement between the autocorrelation and the second moment data. The results are plotted in the bottom panel of Figure 5.14.

The first observation from the figure is that autocorrelation and the second moment curves for the exact dissipation rate lie almost on top of each other. This confirms the mathematical analysis of Monin and Yaglom [1975, §25]. There is no corresponding agreement for either surrogate, which is perhaps not surprising. A very encouraging result, with respect to using surrogates to estimate μ, however, is that the autocorrelation curve for the longitudinal surrogate almost aligns with the autocorrelation of the true dissipation rate for $r/\eta > 10$ where power law scaling is observed. In other words, the autocorrelation of the longitudinal surrogate yields the "correct" μ in the sense that it is very nearly the same as that from the dissipation rate itself. Similar conclusions are suggested by Cleve et al. [2003]. This raises the interesting question of why the correct μ can be obtained from the surrogate via the autocorrelation but not by averaging. It cannot be ruled out that this result is an

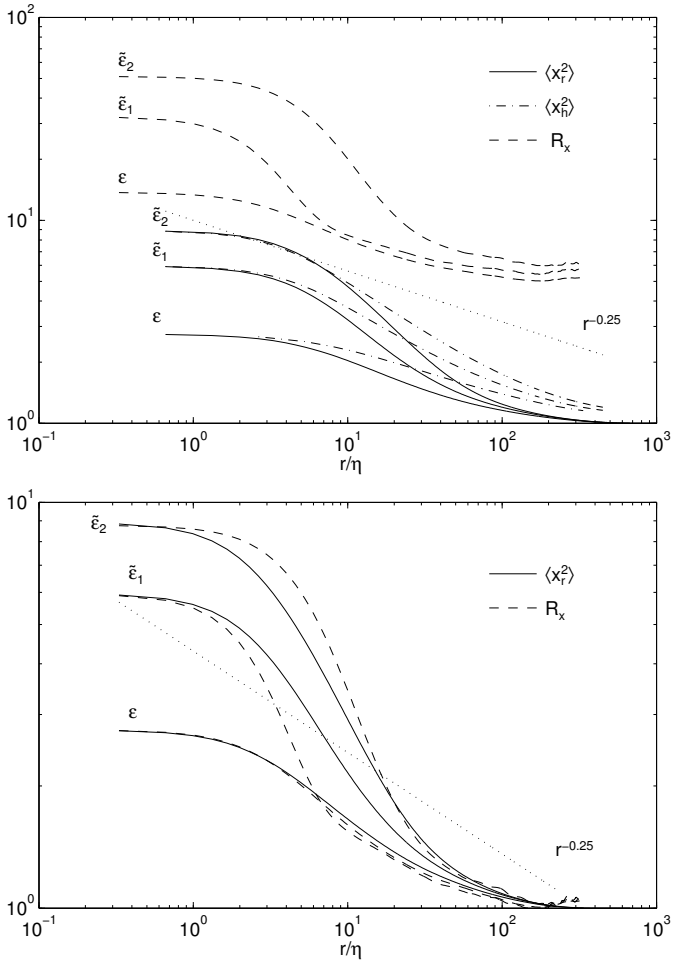

Figure 5.14: Top panel: the second-order moment of locally averaged dissipation rate and surrogates along with the corresponding autocorrelation functions. Note that the autocorrelations have been shifted up for clarity of the figure. Bottom panel: the same data except that the averaging volume in locally averaged variables is a sphere of radius r. x corresponds to each of the variables on the plot.

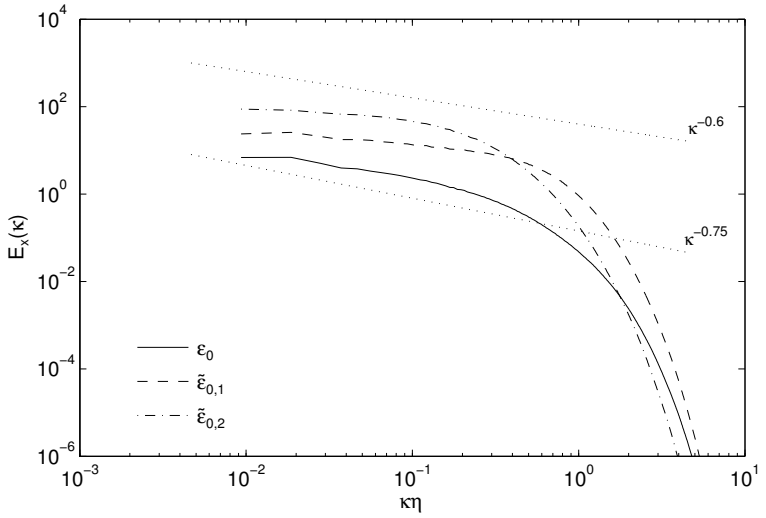

Figure 5.15: The one-dimensional spectra of energy dissipation rate, longitudinal and transverse surrogates. x corresponds to each of the variables in the legend.

artifact of the limited dynamic range in the DNS, but an alternative explanation is the following. It is observed that there is substantially higher intermittency at all but the largest length scales in the surrogates than in ϵ_0. The extreme events in the different components of the strain rate tensor evidently cancel each other. For the longitudinal surrogate, the extreme events can be averaged away simply by conditional averaging (c.f. Figure 5.4). It appears that the autocorrelation function, but not locally averaging, results in cancellation of the extreme events. Why this is so is beyond our current understanding.

Another way to compute the intermittency exponent is via the spectrum of the dissipation rate. By assuming a power law scaling for autocorrelation function of ϵ_0 with slope $-\mu$, it can be deduced that this spectrum will exhibit power law scaling in the scaling range $E_{\epsilon_0} \sim \kappa^{\mu-1}$. The method is used widely in atmospheric measurements and, depending on the choice of scaling range, different values of μ have been reported [e.g Gibson et al., 1970, Monin and Yaglom, 1975, Praskovsky and Oncley, 1997]. The spectra of energy dissipation rate and the longitudinal and transverse surrogates are plotted in Figure 5.15 for case R2. It is observed that in spite of finite

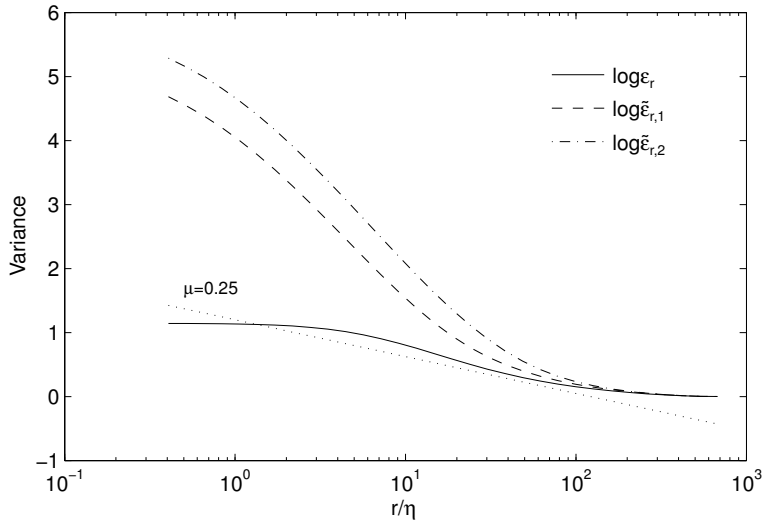

Figure 5.16: The variance of the logarithm of the locally averaged energy dissipation rate, longitudinal, and transverse surrogates.

Reynolds number of the simulations, the spectra do indeed follow a power law in the scaling range but the slope is different for each variable. The flatter slopes in the surrogates are consistent with higher intermittency. The slopes of -0.75 and -0.6 corresponding to the intermittency exponents of 0.25 and 0.4 are also plotted on the figure for comparison.

Finally, a common method of estimating the intermittency exponent is direct application of Kolmogorov [1962] and the lognormal model

$$\sigma^2_{\log \epsilon_r} \sim -\mu \log r. \tag{5.8}$$

In Figure 5.16 the variance of the logarithm of the locally averaged energy dissipation rate and its surrogates are plotted versus the logarithm of r. In agreement with Kolmogorov [1962], all the curves exhibit a linear region in the scaling range, but the slopes, which represent the estimated intermittency exponent, differ. The curve corresponding to the energy dissipation rate is almost parallel to the line with slope $\mu = 0.25$, while the curves corresponding to the surrogates display higher slope. So

once again the surrogates overestimate μ but in this case the differences between the longitudinal and transverse surrogates are small.

The results of this chapter generally suggest a higher intermittency for the transverse surrogates compared with the longitudinal surrogates. In contrary, the logarithm of the surrogates does not confirm such differences. The p.d.f.s of logarithm of the surrogates are very similar and the intermittency exponent estimated from these surrogates assuming lognormal model are also in good agreement. The differences between intermittency of logarithm of transverse and longitudinal surrogates are minimal.

CHAPTER 6

DIRECT NUMERICAL SIMULATIONS OF HOMOGENEOUS AXISYMMETRIC STRATIFIED TURBULENCE

The characteristics of small scale turbulence in flows dominated by large scale anisotropies, known as complex flows, is an open question. In this chapter, the DNS of stratified turbulence with different degrees of stratification over a wide dynamic range are introduced to study the effect of large scale anisotropies and complexities on the small scale dynamics and dissipative mechanisms. Understanding behavior of turbulence in strongly stratified flows is important in its own right. Here, stratification is used simply as a convenient way to create a homogeneous but anisotropic flow. A brief introduction to density stratified turbulence, simple flow with dominant large scale anisotropies, is presented in the following section. The details of the simulations and the related parameters are discussed in the second section followed by some results on the kinetic energy dynamics. Further investigations of this data set related to the small scale turbulence and intermittency are covered in the next chapter.

6.1 Density Stratified Turbulence

The mesoscale geophysical flows, including atmospheric and oceanic flows, are dominated by density stratification effects. Turbulence often occurs in the density stratified flows due to overcoming of inertial forces to stabilizing effects of viscosity and gravity. The dominant source of turbulence is the internal wave breakdown, while Kelvin-Helmholtz and zig-zag instabilities are also significant source of turbulence [Billant and Chomaz, 2000a,b, 2001, Billant et al., 2010, Deloncle et al., 2008,

Lindborg, 2006, Riley et al., 1981] . The vertical shear that sets the stage for these instabilities is spontaneous, *i.e.,* no mean shear is required. If there is any residual shearing motion then strong vertical shear develops as the flow forms layers. Stratified flows are usually simplified and modeled by Boussinesq approximation [Boussinesq, 1903]. A description of Boussinesq approximation as well as the complete set of governing equations in stratified turbulence are presented in Appendix A.

When a high Reynolds number flow subject to a stabilizing density gradient becomes unstable due to vertical shearing, the resulting turbulence is thought to be fully three-dimensional, but with the vertical length scale constrained by buoyancy forces. Further, it is thought that the turbulence develops a cascade with net transfer of energy down scale. These generalizations are based on laboratory experiments, numerical simulations and theoretical studies [e.g. Billant and Chomaz, 2000a,b, Fincham et al., 1996, Lindborg, 2005, 2006, Praud et al., 2005, Riley and de Bruyn Kops, 2003b]. The flow regime is termed *stratified turbulence* by Lilly [1983], Riley and Lelong [2000] provide a review, and Riley and Lindborg [2008] discuss its possible relevance to geophysical flows.

Note that the flows considered here are "strongly stratified", *i.e.*, the buoyancy force is at least as important as the inertial force. When a laboratory flow is strongly stratified, the dynamics are dramatically different from those of flows subjected to weaker stratification. For instance, horizontal eddies form and decouple in the vertical [Beckers et al., 2001, 2002, Bonnier and Eiff, 2002, Fincham et al., 1996, Flór and van Heijst, 1994, Lin and Pao, 1979, Meunier et al., 2006, Spedding et al., 1996a,b, Trieling and van Heijst, 1998, Voropayev et al., 1991, 1997], and the flows evolve much more slowly in time [Spedding et al., 1996a,b]. A number of experiments have been designed to isolate and study the structure of stratified flows, [e.g. Billant and Chomaz, 2000b, Bonnier et al., 2000, Godoy-Diana and Chomaz, 2003, Godoy-Diana et al., 2004, Spedding, 2002, Voropayev et al., 2001].

Numerical simulations have also been used to understand the stratified regime. Several of the early numerical studies involved hypothetical flows Herring and Métais [1989], Jacobitz et al. [1997], Métais and Herring [1989], Riley et al. [1981]. Even as computers have become more capable, simple flow configurations that are not readily realized in physical experiments have proven valuable for understanding certain aspects of stratified turbulence [e.g. Brethouwer and Lindborg, 2009, Deloncle et al., 2008, 2011, Hebert and de Bruyn Kops, 2006, Herring and Kimura, 2008, Lindborg, 2006, Riley and de Bruyn Kops, 2003a]. Other simulations have addressed laboratory flows such as wakes, mixing layers, and shear layers [e.g. Arobone and Sarkar, 2010, Basak and Sarkar, 2006, Brucker and Sarkar, 2007, 2010, Pham and Sarkar, 2010]. Recently, Diamessis et al. [2011] used large-eddy simulations to extend the wake experiments of Spedding et al. [Spedding et al., 1996a,b].

While there is some agreement in the literature on the basic features of stratified turbulence, a detailed picture of the energetics is not clear. One of the difficulties is due to the fact that the flow does not abruptly transition globally from laminar to turbulent but rather forms patches of turbulence. Following experimental studies of atmospheric turbulence, most of the numerical studies focused on investigating energy cascade and spectra. A power law spectrum is generally accepted but directional spectra exhibit different scaling behavior. The horizontal spectrum decays with close to $-5/3$ slope while the vertical spectrum shows much steeper slope [see e.g. Dewan and Good, 1986, Lindborg, 2006, Nastrom and Gage, 1985]. Recent research confirms the idea of forward energy cascade, *i.e.,* energy transfer from large to smaller scales [Lindborg, 2006, Riley and de Bruyn Kops, 2003a, Riley and Lindborg, 2008] .

It is generally believed that the directional differences diminish at smaller scales. The so-called Ozmidov length scale is defined as the smallest scale to which the stratified turbulence hypothesis can be applied. At scales smaller than Ozmidov length scale, the stratification effect is negligible and flow is supposedly similar to three-

dimensional homogeneous and isotropic turbulence. However, there is not enough research to prove such a theory and a detailed knowledge of small scale stratified turbulence remains an open question. The experimental measurements have shortcomings in providing information about the structures and turbulence dynamics at these scales and numerical simulations are always limited by the resolution and dynamic range.

A brief summary of the theoretical relationships and scaling analysis of stratified turbulence is provided in the next section. In the remainder of this chapter, DNSs of strongly stratified turbulence with extensive dynamic range are presented and the flow dynamics are analyzed. The unique DNS data exhibit large scale anisotropies while they are well resolved at small scales. A DNS data set of isotropic turbulence with similar dynamic range and resolution is also included for one to one comparisons of statistics of stratified turbulence with those of isotropic turbulence.

6.1.1 Theoretical Relationships

Many length and time scales are used to describe stratified turbulence, and the theoretical relationships between them have been developed in the limit of low Froude number [Billant and Chomaz, 2001, Lindborg, 2006, Riley and de Bruyn Kops, 2003a, Tseng and Ferziger, 2001]. In simulations, due to the limited dynamic range, these relationship can be difficult to discern, particularly when there are multiple ways to compute a theoretical quantity. Waite [2011] provides a recent analysis of the importance of careful attention to lengths scales in numerical simulations.

In this section, in addition to the classical key length scales of isotropic turbulence, some of the commonly used length scales in stratified turbulence are introduced and discussed. The Kolmogorov length scale and the Taylor micro-scale, which represent small and moderate scales in turbulent flows, are defined based on the averaged kinetic energy, $\overline{k}$, and averaged dissipation rate, $\bar{\epsilon}$, as below:

$$\eta \equiv \left(\frac{\nu^3}{\bar{\epsilon}}\right)^{1/4}, \tag{6.1}$$

and,

$$\lambda \equiv \left(\frac{10\nu\overline{k}}{\bar{\epsilon}}\right)^{1/2}. \tag{6.2}$$

It is generally believed that the dynamics of stratified flow at these scales are dominated by three-dimensional turbulence. Note that the occurrence of turbulence in the intermittent patches throughout the stratified flows and the existence of regions that are in approximately solid body motion with high energy but low dissipation rate, decreases the averaged dissipation rate of kinetic energy, significantly. Thus, the Kolmogorov and Taylor length scales defined based on the averaged value might overestimate the characteristics length scales of the small scale motion in stratified flows. We are not certain about the application of these two length scales in interpreting stratified turbulence and consider them cautiously here. The outer scale of three-dimensional turbulence in these flows known as Ozmidov length scale [Gargett et al., 1984, Lumley, 1964, Ozmidov, 1965],

$$L_O \equiv \left(\frac{\bar{\epsilon}}{\mathcal{N}^3}\right)^{1/2}, \tag{6.3}$$

which is defined based on dimensional reasoning, as is the smallest scale of turbulence, the Kolmogorov length scale η. $\mathcal{N}^2 = -(g/\rho_0)(d\rho_0/dz)$ is the square of the buoyancy frequency. If the factor of 2π is included in the conversion of frequency to time then the Ozmidov scale is

$$L_O^* \equiv \left(\frac{(2\pi)^3\bar{\epsilon}}{\mathcal{N}^3}\right)^{1/2}, \tag{6.4}$$

This is not a standard definition but it is consistent with including the factor of 2π in the other length scales and non-dimensional parameters that are defined later in this section. We retain the factor of 2π in the conversion between time and frequency

because omission of order one constants can make it difficult to interpret DNS data given the limited range of length and time scales in the simulated flows.

At larger scales, the flow dynamics are dominated by anisotropic flow with horizontal length scales much larger than the vertical ones. The outer horizontal scale of stratified turbulence corresponding to L in isotropic turbulence can be estimated by dimensional reasoning as [Taylor, 1935]

$$L_h \equiv \frac{\overline{E}_h^{3/2}}{\bar{\epsilon}} = \frac{u'^3}{2\sqrt{2}\bar{\epsilon}} \,, \tag{6.5}$$

with $\overline{E}_h^{3/2}$ as the kinetic energy due to horizontal motion. Here u' and w' are the root-mean-square horizontal and vertical velocities, respectively. Calculation of this length scale in stratified flows is also complicated due to the existence of quiescent regions. Hebert and de Bruyn Kops [2006] found that in simulations, even with significant turbulence, that L_h can be larger than the size of the simulation domain. The integral or correlation scale, equivalent to ℓ in isotropic turbulence, is more readily interpreted as the size of the horizontal motions in the flow. The horizontal integral length scale L_{hh} is defined as the integral of the autocorrelation of horizontal velocity in the horizontal direction.

The vertical length analogous to L_{hh} for unstratified flow is L_{vv}, the integral of the longitudinal autocorrelation of u_3. Strongly stratified flow dynamics, however, are thought to be dominated by the horizontal velocity and of principal interest in stratified flows is the characteristic thickness of the horizontal layers that form. Therefore the integral scale L_{hv} based on the vertical autocorrelation of the horizontal velocity is expected to be relevant in the case of strong stratification. Applying order of magnitude estimates to the continuity equation leads to $L_{hh}w'/u'$ as an estimate for the dynamically important vertical scale.

The buoyancy time scale is related to the buoyancy frequency by $T_b \equiv 1/N$, from which the buoyancy length scale is defined as

$$L_b \equiv \frac{u'}{\mathcal{N}} \ , \tag{6.6}$$

If the factor of 2π is included in the conversion of frequency to time then

$$L_b^* \equiv 2\pi \frac{u'}{\mathcal{N}} \ . \tag{6.7}$$

Note that, similar to Lo^*, we retain the factor of 2π in the conversion between time and frequency because omission of order one constants can make it difficult to interpret DNS data given the limited range of length and time scales in the simulated flows. The buoyancy scale is an important length in the generation of turbulence by overturning of internal gravity waves [Carnevale et al., 2001, Waite and Bartello, 2006] and the zigzag instability in columnar vortices [Billant and Chomaz, 2000b]. Of significance in the current study is that it is expected to characterize the thickness of the shear layers in stratified turbulence [Billant and Chomaz, 2001, Lilly, 1983, Waite and Bartello, 2004] and so should be comparable to L_{hv}.

Several definitions of Reynolds and Froude numbers can be written in terms of the foregoing length scales. The nominal Froude, Prandtl, and Reynolds numbers are defined based on nominal velocity scale $\hat{U}$ and length scale $\hat{L}$ as

$$F = \frac{2\pi\hat{U}}{\mathcal{N}\hat{L}}, \ \ \mathrm{Pr} = \frac{\mu c_p}{K} \ \ \text{and} \ \ Re = \frac{\hat{U}\hat{L}}{\nu} \, .$$

The horizontal Froude and Reynolds numbers can be defined as:

$$F_h = \frac{2\pi u'}{\mathcal{N} L_{hh}} \tag{6.8}$$

and

$$Re_h = \frac{u' L_{hh}}{\nu}. \tag{6.9}$$

By the analysis of Billant and Chomaz [2001], the vertical length scale will adjust to the stratification so that the vertical Froude number

$$F_v = \frac{2\pi u'}{\mathcal{N} L_{hv}} \sim 1 \ . \tag{6.10}$$

Apparent differences between various simulations and laboratory experiments suggest that careful consideration must be paid to the location in Reynolds-Froude number parameter space of an experiment or simulation. Simply reporting Reynolds and Froude numbers may not be sufficient, particularly if the dynamically relevant length and velocity scales are among the quantities being investigates. There is an analogous need to accurately identify the Reynolds number regime in studies of unstratified turbulence. In that case, well-developed theory for the dynamics of turbulence at high Reynolds number exists against which to verify experimental or simulation data. For stratified turbulence, the theory is not as advanced but a number of studies provide expected characteristics for flows in the limit of strong stratification. For instance Riley et al. [1981] present a scaling analysis that separates the flow into internal waves and vortical modes. Theoretical analyses of self-similar scaling [Billant and Chomaz, 2001] and the "zig-zag" instability [Billant and Chomaz, 2000a,b, Billant et al., 2010, Deloncle et al., 2008] provide frameworks for characterizing a flow. Lindborg [2006] reviews a number of theoretical relationships expected to hold for strongly stratified flow at high Reynolds number. Riley and de Bruyn Kops [2003a] postulate that $Re_h F_h^2$, rather than the either the Reynolds or Froude numbers by themselves, is the important parameter for predicting the occurrence of stratified turbulence. Hebert and de Bruyn Kops [2006] report that $Re_h F_h^2$ and buoyancy Reynolds Re_b are linearly related in their simulations. The buoyancy Reynolds number is

$$Re_b = \left(\frac{L_o}{\eta} \right)^{4/3} . \tag{6.11}$$

It has been hypothesized that the flow must have buoyancy Reynolds number, Re_b, above a threshold value of about 30 in order for turbulence to be significant [Gibson, 1980, Gregg, 1987, Imberger and Boashash, 1986, Smyth and Moum, 2000].

6.2 Numerical Simulations

The DNSs of stratified flow with a range of Re_b are considered. There is no mean shear and no internal waves are intentionally introduced so that the turbulence in the flows results primarily from instabilities in horizontal layers that spontaneously form. A very simple flow configuration is considered for this research. Specifically, persistent numerical forcing at large scales in the horizontal is used to represent a two-dimensional outer flow. This force induces homogeneous and axisymmetric turbulence at smaller scales. A range of Froude numbers is considered to understand how the turbulence responds to the outer flow as a function of stratification strength. Importantly, the Froude numbers are order unity or smaller and are chosen to span the threshold value of $Re_b = 30$. The Prandtl number is unity, close to that in the atmosphere but not that in the ocean; de Stadler et al. [2010] report on a recent investigation on the effect of Prandtl number in simulations of stratified turbulence.

The simulated flows considered in this research are solutions to the Navier-Stokes equations in a non-rotating reference frame subject to the Boussinesq approximation. The dimensionless governing equations are

$$\nabla \cdot \boldsymbol{u} = 0 \tag{6.12a}$$

$$\frac{\partial \boldsymbol{u}}{\partial t} + \boldsymbol{u} \cdot \nabla \boldsymbol{u} = -\left(\frac{2\pi}{F}\right)^2 \rho \boldsymbol{e}_z - \nabla p + \frac{1}{Re}\nabla^2 \boldsymbol{u} + \boldsymbol{b} \tag{6.12b}$$

$$\frac{\partial \rho}{\partial t} + \boldsymbol{u} \cdot \nabla \rho - w = \frac{1}{Re\,\mathrm{Pr}}\nabla^2 \rho \ . \tag{6.12c}$$

Here, $\boldsymbol{u} = (u, v, w)$ is the velocity vector, and ρ and p are the deviations of density and pressure from their ambient values. Also, $\boldsymbol{e}_z$ is the unit vector in the vertical direction.

The pressure is scaled by the dynamic pressure and the density using the ambient density gradient. The nominal Froude, Prandtl, and Reynolds numbers are defined in the previous section with $\hat{U}$ and $\hat{L}$ as the forcing scales. For the details on the complete set of equations and variables the reader is referred to Appendix A. The force, $\boldsymbol{b}$, is implemented by the deterministic forcing schema [Rao and de Bruyn Kops, 2011]. The objective is to force all of the simulations to have the same spectra at large scales. The highest wave number forced is $\kappa_f = 16\pi/\mathcal{L}_h$ with $\mathcal{L}_h$ the horizontal dimension of the numerical domain. Deterministic forcing requires choosing a target spectrum. Unlike for turbulence that is isotropic and homogeneous in three dimensions, there are no theoretical model spectra for forcing (c.f. [Overholt and Pope, 1998]). Therefore, run 2 from Lindborg [2006] was rerun using a stochastic forcing schema similar to that used by Lindborg. The spectrum for large scales was computed from this simulation and used as the target for the simulations reported here. In addition to forcing the large horizontal scales, 1% of the forcing energy is applied stochastically in vertical scales. This random forcing induces some vertical shear [Lindborg, 2006].

The governing equations (6.12) are solved numerically using the pseudo-spectral technique described in Riley and de Bruyn Kops [2003a]. Spatial derivatives are computed in Fourier space, the non-linear terms are computed in real space, and the solution is advanced in time in Fourier space with the variable-step, third-order, Adams-Bashforth algorithm with pressure projection. The non-linear term in the momentum equation is computed in rotational form, and the non-linear term in the internal energy equation is computed in conservation and advective forms on alternate time steps. These techniques are standard to eliminate most aliasing errors, but the simulations are fully dealiased in accordance with the 2/3 rule via a spectral cutoff filter.

The extent of the domain in the horizontal and vertical directions are $\mathcal{L}_h$ and $\mathcal{L}_v$ with $\mathcal{L}_h/\mathcal{L}_v$ chosen to accommodate the vertical motions that develop in the flow.

While the simulation domains are not cubes and the vertical extent of the domain varies with Froude number, the grid spacing Δ is the same in all directions. It is assumed for the purpose of choosing the resolution of the numerical grid that the flows are approximately isotropic at the smallest length scales in the simulation. Therefore, a three-dimensional grid with spacing Δ in all directions is used and any small-scale anisotropy in the flows can be attributed to flow physics rather than to numerical artifacts of an anisotropic grid (c.f. Waite [2011]).

6.2.1 Simulation Parameters

Before considering the dynamics of the flows, it is worthwhile to review some choices made in choosing the simulation parameters. On the one hand, we are interested in the strongly stratified regime with buoyancy Reynolds number spanning 30. So it is desirable to have one case with Froude number near the upper limit expected to be consistent with strong stratification. On the other hand, one can hypothesize a lower limit of the Froude number at which, for a given Reynolds number, the stratification is so strong that two-dimensional turbulence will be pronounced even if three-dimensional stratified turbulence is present. If this occurs then upscale transfer of energy at large length scales will preclude a numerically stable and statistically stationary solution without revamping the simulations. For the current research, a simulation more strongly stratified than those reported was run but abandoned when the energy at the largest length scales rose so high as to cause numerical difficulties. This simulation is mentioned because it suggests that the simulations that are reported here fairly bracket the range of strong stratification that can be studied with the current methodology until computers become sufficiently powerful to simulate flows at higher Reynolds number.

Three simulations are considered all having the same forcing spectrum, Prandtl number, and nominal Reynolds number but different values of Froude number. They

are denoted by F1, F2, and F3 in order of descending Froude number. The parameters and statistics are extracted from the simulations after the flow had reached statistical stationarity. In addition to the stratified simulations, we include a data set of homogeneous isotropic turbulence simulations with a dynamic range similar to the stratified cases denoted as R4. Case R4 is similar to the simulations discussed and analyzed in chapters 4, but with lower small-scale resolution and larger dynamic range. The simulation parameters are given at the top of Table 6.1 for all the cases.

The general parameters of the simulations are listed in the first section of the table. The isotropic homogeneous case is twice better resolved compared with the stratified flows. λ/η is almost the same for all of the simulations and the Reynolds number based on λ is in a similar range for all of the cases, slightly higher for the stratified flows. This verification is important for small scale intermittency studies, which is discussed in the next chapter. The different definitions of the non-dimensional parameters are in good agreement with the nominal parameters. The horizontal Froude numbers order of one and smaller indicate strongly stratified flow regime, which is the case for stratified simulation cases. Re_b spans over the threshold value of 30. The last section of the table lists the theoretical length scales defined earlier.

6.3 Overview and Verification of Simulated Flows

We begin our analysis with an overview of the velocity fields, proceed to the one-dimensional spectra of the kinetic energy and second-order structure functions of the velocity field. Spectra are a valuable tool for studying turbulence (c.f. 4.2.5). Stratified flow, however, is obviously not isotropic in three dimensions at all length scales and so spectra averaged over spherical shells have no obvious interpretation. Therefore, one-dimensional spectra are usually considered. These can be misleading, though due to both aliasing and averaging effects. Because of the limited dynamic range of simulations, multiple theoretical length scales are close together and it can be

Identifier	F1	F2	F3	R4
$\mathcal{L}_h/\Delta$	4096	4096	4096	4096
$\mathcal{L}_v/\Delta$	2048	1024	512	4096
$\mathcal{L}_h/\mathcal{L}_v$	2	4	8	1
$\kappa_{\max}\eta$	1.5	1.5	1.5	3.2
η/Δ	0.72	0.74	0.73	1.54
λ/η	42	43	44	40
$L_h/\mathcal{L}$	0.35	0.40	0.45	0.41
Re_λ	466	472	500	400
$Re_L = \overline{k}^2/\bar{\epsilon}\nu$	32643	33356	37530	23660
$w'^2/2\overline{k}$	0.12	0.07	0.04	0.31
F	1.048	0.5239	0.2615	
$F_h = 2\pi u'/\mathcal{N}L_{hh}$	1.46	0.58	0.26	
$F_v = 2\pi u'/\mathcal{N}L_{hv}$	1.96	1.80	1.33	
Re	9216	9216	9216	
$Re_h = u'L_{hh}/\nu$	10300	12800	16300	
$Re_h F_h^2$	22100	4330	1080	
Re_b	220	48	13	
L_O/Δ	41	14	5	
L_O^*/Δ	648	216	79	
$L_b/\mathcal{L}_v$	0.057	0.056	0.058	
$L_b^*/\mathcal{L}_v$	0.36	0.35	0.37	
$L_{hh}/\mathcal{L}_h$	0.14	0.18	0.21	0.17
$L_{hv}/\mathcal{L}_v$	0.21	0.23	0.33	
$L_{vv}/\mathcal{L}_v$	0.09	0.16	0.17	0.17

Table 6.1: Simulation parameters.

difficult to understand the significance of each length scale in terms of aliased spectra. Additionally, one-dimensional spectra from simulations are typically averaged in the vertical direction, which can make them hard to interpret. To avoid, as much as possible, the challenges associated with interpreting one-dimensional spectra, one can consider the so-called two-dimensional spectra integrated over horizontal circles to form a spectrum in terms of horizontal and vertical wave number. The two-dimensional spectra analysis are not included in this section and for the details the reader is referred to Almalkie and de Bruyn Kops [submitted].

6.3.1 Local Velocity

For a qualitative view of the range of length scales that exist in the simulations and the resolution of the small scales, consider contour plots of the instantaneous velocity. A horizontal slice of vertical velocity for case F3 is plotted in Figure 6.1 at four magnifications. The lowest magnification, panel A of the figure, reveals large horizontal structures with linear dimension about one quarter of the simulation domain. This suggests $L_{hh}/\mathcal{L}_h \approx 1/5$, which is close to the value of 0.21 given in Table 6.1. Also evident are the patches of strong vertical velocity interspersed with regions of near zero vertical velocity. In the other panels of the figure, the region of high vertical motion in the lower left corner of panel A is magnified to reveal some of its structure. From panel D, which shows a region of 64×64 grid points, it appears that the flow is well resolved spatially.

A vertical slice of the u-velocity for case F3 is shown in Figure 6.2. At the lowest magnification, it appears that there are four horizontal layers in much of the image, which leads us to expect that the vertical length scale of the horizontal motions is about 0.25 $\mathcal{L}_v$. The visual estimate of the length scale is a little smaller than the numerical values of $L_{hv}/\mathcal{L}_v$ and $L_b/\mathcal{L}_v$ given in the table. Note that the ratio $L_{hv}/\mathcal{L}_v$ is increasing with stratification strength while $L_b/\mathcal{L}_v$ stays almost constant for all three

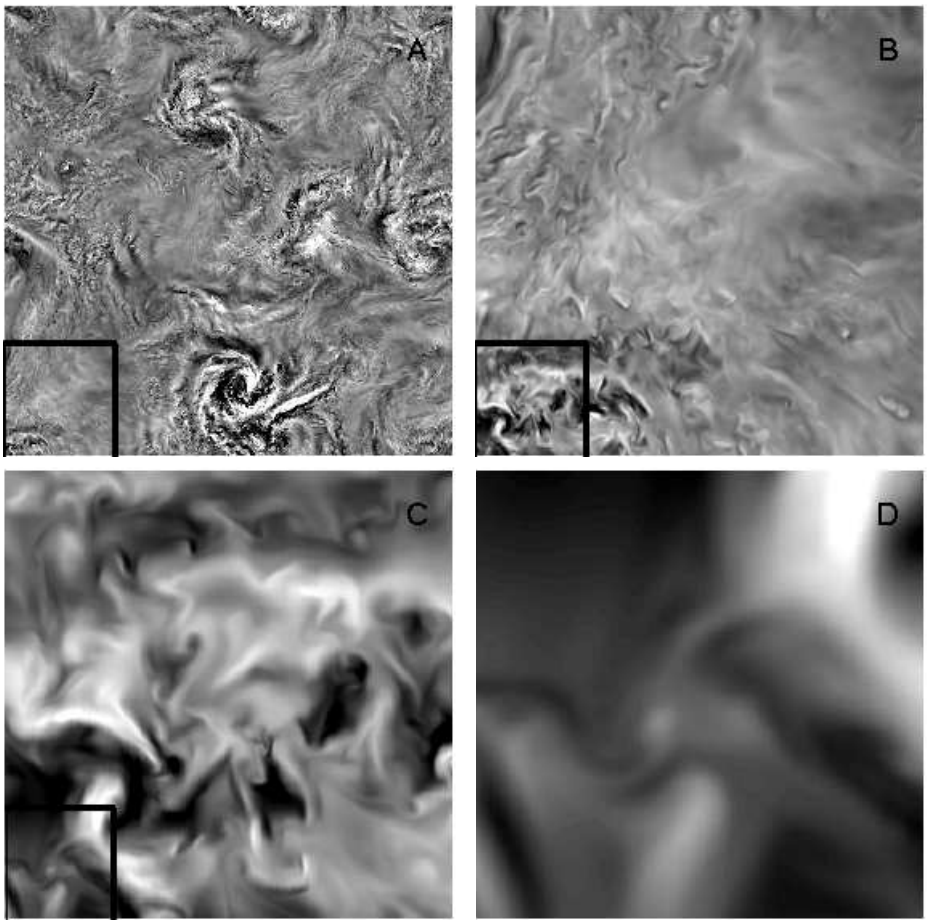

Figure 6.1: A horizontal slice of vertical velocity normalized by its rms value for case F3. The color scale goes from -3 (black) to +3 (white). Each panel shows the region in the black square on the preceding panel. The number of grid points in each direction are A) 4096, B) 1024, C) 256, D) 64.

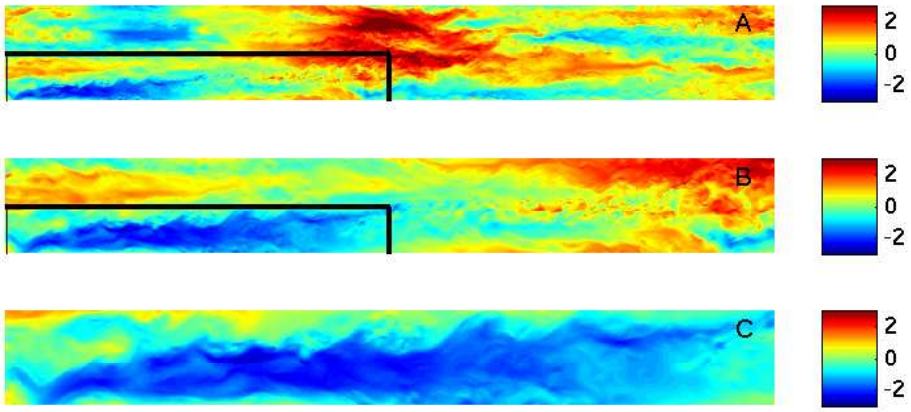

Figure 6.2: A vertical slice of horizontal velocity normalized by its rms value for case F3. Each panel shows the region in the black square on the preceding panel. The number of grid points are A) 4096×512, B) 2048×256, C) 1024×128.

cases. This suggests that the buoyancy length scale is decreasing linearly with Froude number and is the appropriate characteristic vertical length scale of the horizontal motion. By magnifying the image to produce panels B and C of the figure, Kelvin-Helmholtz billows are evident, which is consistent with the observations of Riley and de Bruyn Kops [2003a]. From the agreement between the visual and calculated vertical length scales it is concluded that the flow is forming layers with the expected thickness [Billant and Chomaz, 2001, Lilly, 1983, Waite and Bartello, 2004]. It is also concluded that the calculations of the thickness of these layers, in particular the inclusion of the factor of 2π in the definition of L_b^*, are correct.

6.3.2 One-Dimensional Spectra and Structure Functions

Anisotropic dynamics of stratified flows require definition of directional statistics including directional spectra and structure functions. The flow is perfectly axisymmetric, thus the statistics are independent of horizontal directions x, y. The vertical statistics, however, are dominated by a very different dynamics. In this section we will consider one-dimensional spectra and structure functions of both horizontal and vertical velocities. For the horizontal velocity components, the transverse statistics in

the horizontal and vertical directions are treated separately. Therefore, in addition to the conventional longitudinal and transverse statistics, the vertical statistics are also defined. The spectra, for example for u_1, are denoted $E_{u_1}(\kappa_1)$ as longitudinal, $E_{u_1}(\kappa_2)$ as transverse, and $E_{u_1}(\kappa_3)$ as vertical spectra. Similarly, the structure functions for u_1, are denoted $D_{u_1}(r_x)$ as longitudinal, $D_{u_1}(r_y)$ as transverse, and $D_{u_1}(r_z)$ as vertical structure functions. As is usual with simulation data, all the spectra and structure functions are averaged over the computational domain.

The one-dimensional spectra of u_1 and u_3 are shown in Figures 6.3 for all the cases. The longitudinal spectra are plotted true while the transverse and vertical spectra are offset by one and two decades, respectively. To make judging the slope of the curves easier, some of the expected power laws are also plotted. The one-dimensional spectra for all the cases show an overall energy cascade from large to small scales in both horizontal and vertical directions. Therefore, the existence of forward energy cascade in both directions in stratified turbulence has been confirmed by this data set. The spectra exhibit an extensive power law scaling range. The slope of the curves, however, are changing over a range of scales and directions. This behavior indicates the existence of multiple dominant dynamics over different ranges of scales.

To understand the scaling characteristics of the spectra and to identify the scaling range in terms of the theoretical length scales, the compensated spectra are plotted in Figures 6.4 and 6.5. Recall from the discussion of Table 6.1 that one can define the length scales by either considering or eliminating a factor of 2π in the buoyancy frequency. We defined the theoretical length scales in both formats and denote the ones with this factor by superscript $*$. In Figure 6.4 the wave numbers are normalized by Ozmidov length scale L_o and in Figure 6.5 by L_o^*.

As it is expected, different scalings are observed for the longitudinal, transverse, and vertical spectra. In the longitudinal spectra of horizontal velocity, there are two different power law ranges. A scaling with $\kappa^{-5/3}$ is apparent over an extended range

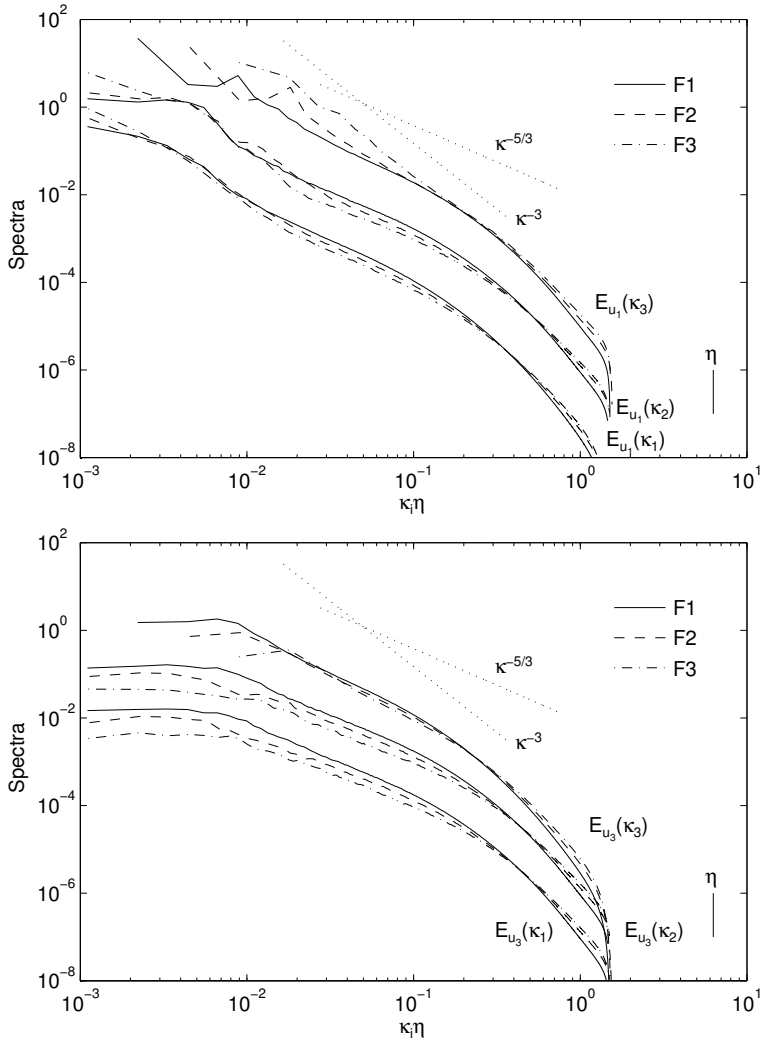

Figure 6.3: Longitudinal, transverse, and vertical spectra for horizontal (top) and vertical (bottom) velocities. The longitudinal spectra is plotted true, the transverse spectra are offset by one decade, and the vertical spectra are offset by two decades.

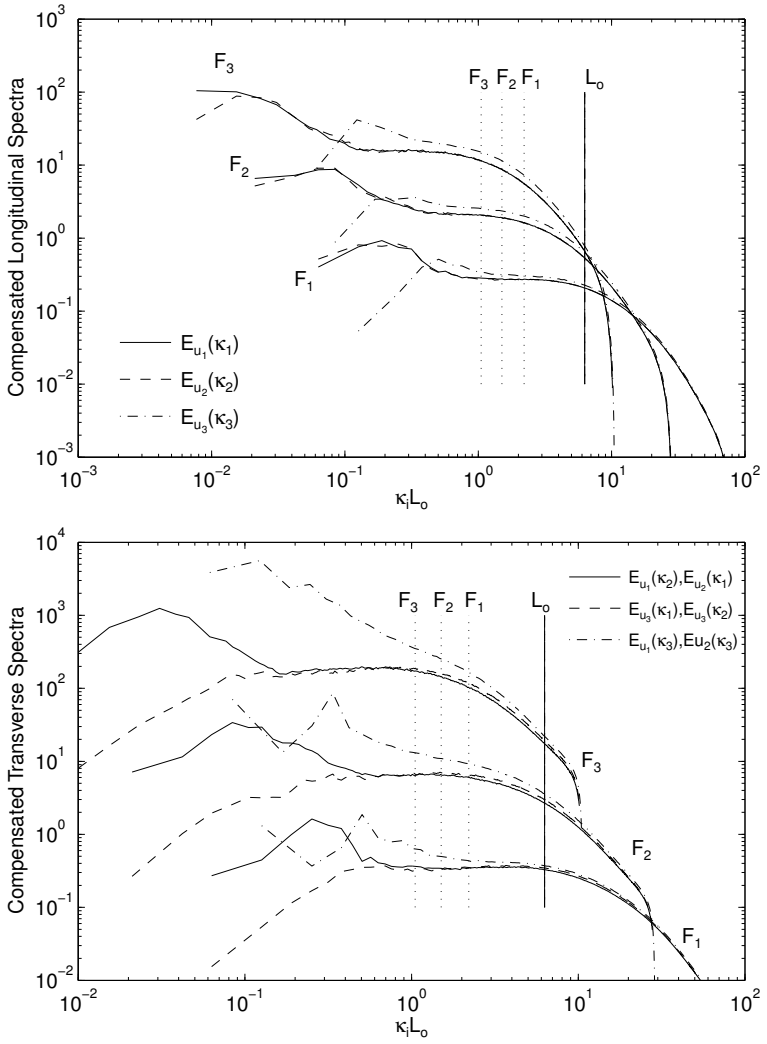

Figure 6.4: Compensated longitudinal (top panel), transverse, and vertical (bottom panel) spectra. The spectra are normalized by Kolmogorov scaling, $E\kappa^{5/3}\overline{\epsilon}^{-2/3}$ and the wavenumber axis is normalized by L_o. The spectra for F1 are plotted true, the spectra are offset by one and two decades for F2 and F3 cases. The Ozmidov L_o and buoyancy L_b length scales are marked with solid and dotted lines, respectively.

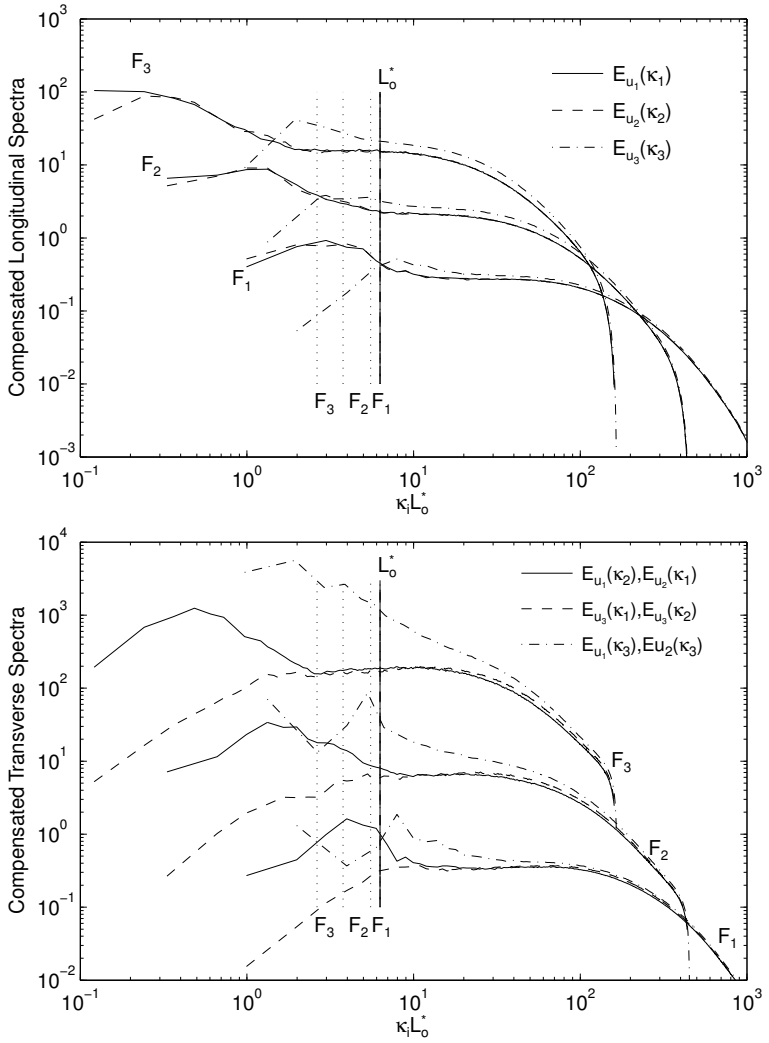

Figure 6.5: Compensated longitudinal (top panel), transverse, and vertical (bottom panel) spectra. The spectra are normalized by Kolmogorov scaling, $E\kappa^{5/3}\bar{\epsilon}^{-2/3}$ and the wavenumber axis is normalized by L_o^*. The spectra for F1 are plotted true, the spectra are offset by one and two decades for F2 and F3 cases. The Ozmidov L_o^* and buoyancy L_b^* length scales are marked with solid and dotted lines, respectively for all the cases.

of wave numbers at small and moderate scales. At larger scales, the slope is much steeper, which indicates stronger power law dependency close to κ^{-3} scaling. The longitudinal spectrum of the vertical velocity exhibits only the $-5/3$ scaling all the way up to large scales.

The transverse spectra of the horizontal velocity follow a trend very similar to the longitudinal spectra. In the case of vertical velocity, the transverse spectra is only scaled by $\kappa^{-5/3}$ over an extensive range of wave numbers. There is a distinct separation point between the transverse spectra of the horizontal and vertical velocities. This scale can be explained as the marginal scale for the horizontal motion due to stratification and large scale anisotropies that only occur in the horizontal direction. The sharp scaling of the transverse spectra of horizontal velocity at scales larger than this margin confirms this hypothesis. The vertical spectra of the horizontal velocity exhibit fundamentally different scaling characteristics. The slope is a function of stratification level and approaches -3 for the strongest stratification in case F3. It is not apparent in the other cases, but it is not clear if this result is significant or if it is just an artifact of the limited scale separation and the inherent aliasing in one-dimensional spectra. Scaling of the vertical spectra with κ_3^{-3} satisfies self-similarity under the assumption of strong stratification [Billant and Chomaz, 2001]. Note that the separation of the vertical spectra of the horizontal velocity from the other transverse spectra can be related to the outer scale of three-dimensional turbulence.

The scaling discussed above is consistent for all the cases, however, there is no obvious relationships to the theoretical length scales can be deduced. Again, it is not clear if this is significant or if it is just an artifact of the limited scale separation and the inherent aliasing in one-dimensional spectra. It seems that $-5/3$ slope is observed for scales both smaller and larger than the Ozmidov length scales up to buoyancy length scale. It is tempting to conclude that a stratified inertial range and a fully three-

dimensional inertial range exist, both with $\kappa^{-5/3}$ scaling. This would explain why the range of wave numbers over which this power law scaling is observed is significantly greater than expected based on simulations of unstratified isotropic turbulence at comparable Reynolds numbers (case R). The $-5/3$ scaling of the stratified inertial range is consistent with the literature [e.g. Dewan, 1979, Dewan and Good, 1986, Kitamura and Matsuda, 2006, Lindborg, 2005, 2006, Riley and Lindborg, 2008].

To provide more information about scaling of stratified flows, we consider the second-order structure functions of u_1 and u_3 as plotted in two panels of Figure 6.6 for all the cases. To make judging the slope of the curves easier, some of the expected power laws are also plotted. Structure functions and spectra contain the same information and one can be computed from the other. As discussed in chapter 4, in the inertial range of isotropic turbulence with large scale separation, the power law scaling of structure functions can be deduced from that of one-dimensional spectra; Obukhov's $\kappa^{-5/3}$ scaling of spectra corresponds to Kolmogorov's $r^{2/3}$ scaling of second-order structure functions. This relationship is observed in the structure functions of u_3. It seems that the slopes are sharper for the structure functions of the horizontal velocity.

The compensated structure functions, scaled by $(r\bar{\epsilon})^{2/3}$, are plotted in Figures 6.7 and 6.8. Similar to the spectra, in the plots horizontal axis is normalized by both L_o and L_o^*. As expected, the structure functions of the vertical velocity exhibit a plateau over a range of scales, which indicates $r^{2/3}$ scaling. The longitudinal and transverse structure functions of the horizontal velocity exhibit two different power law scalings over the range of scales that corresponds to the $\kappa^{-5/3}$ region of the spectra. At smaller length scales a small plateau develops, which indicates the existence of the Kolmogorov scaling but immediately it turns to a sharper power law at larger scales. It can be hypothesized that the range of smaller scales corresponds to the inertial range of the three-dimensional turbulence, while the sharper slope corresponds to

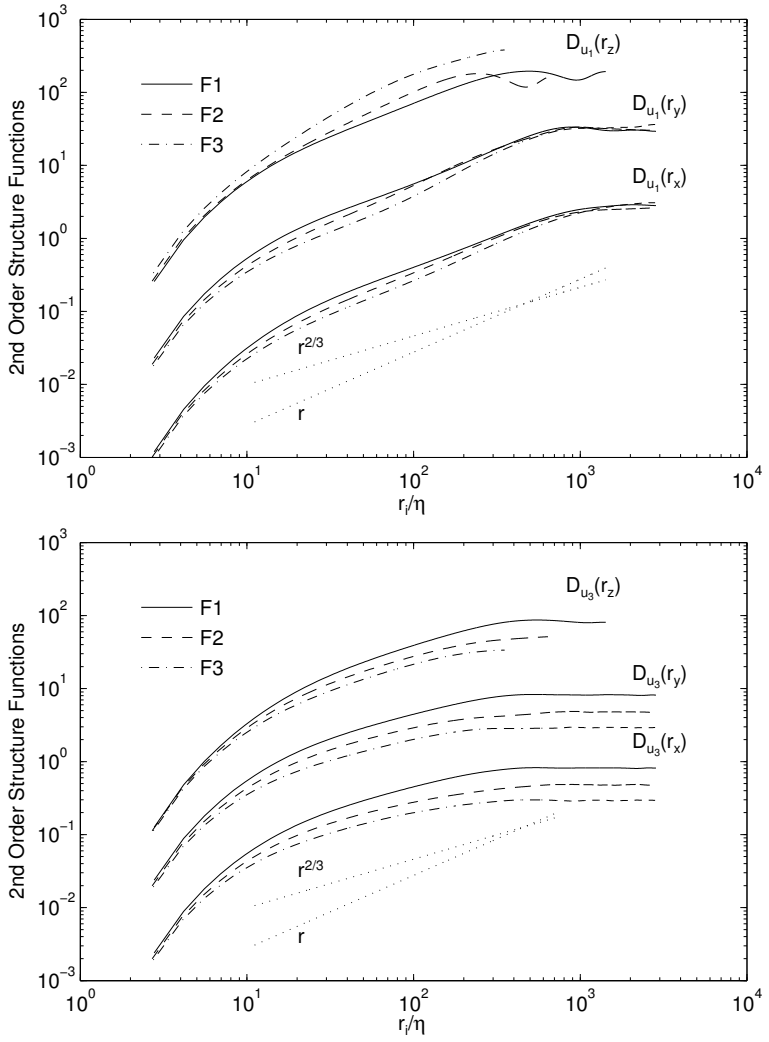

Figure 6.6: Longitudinal, transverse, and vertical structure functions for horizontal (top) and vertical (bottom) velocities. The longitudinal structure functions are plotted true, the transverse structure functions are offset by one decade, and the vertical structure functions are offset by two decades.

the inertial range of stratified turbulence. The inertial range of stratified turbulence exhibits a $-5/3$ slope region in the spectra but that does not imply a $2/3$ slope in the structure functions. This suggests that the flows do not exhibit Kolmogorov-Obukhov scaling, which is in agreement with the hypotheses of Riley and Lindborg [2008].

Similar to the spectra, the marginal separation points of the longitudinal and transverse structure functions of the vertical velocity from those of the horizontal velocity are observed for all three cases. Note that a scaling close to r^1 is observed for the vertical structure functions of the horizontal velocity. Consistent with the vertical spectra, the slope of the vertical structure functions increases by the stratification level. Again as it is discussed earlier, there is no obvious relationships to the theoretical length scales can be deduced.

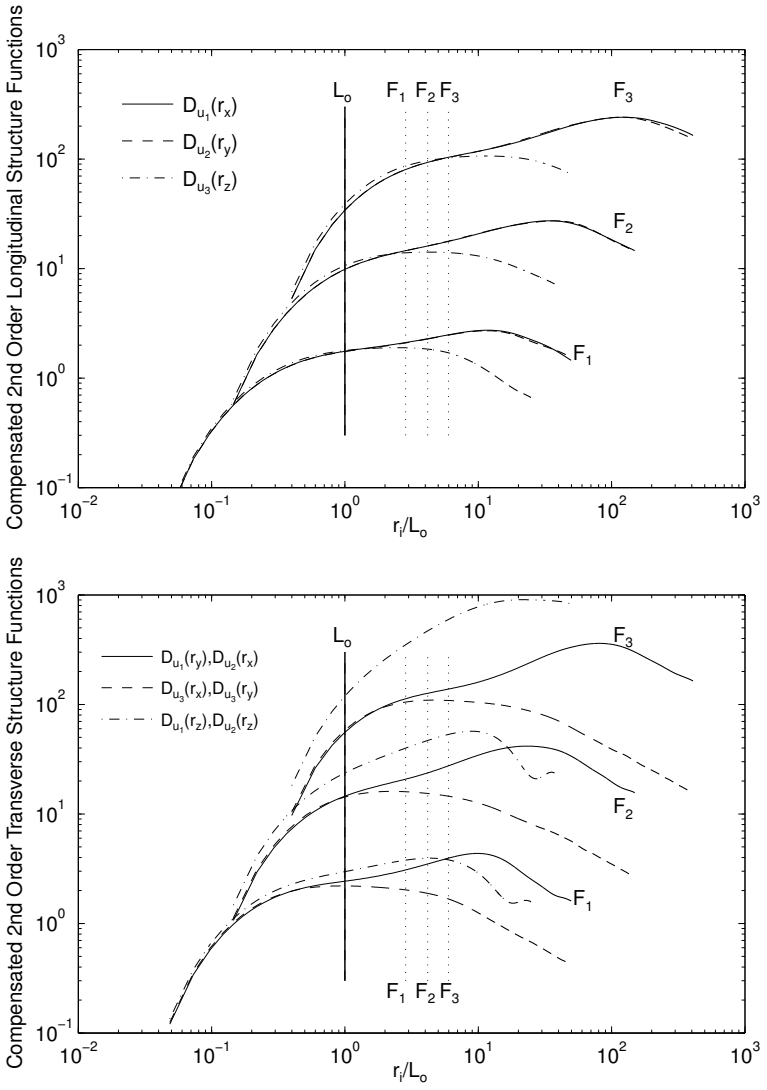

Figure 6.7: Compensated longitudinal (top panel), transverse, and vertical (bottom panel) second-order structure functions. The structure functions are normalized by Kolmogorov scaling, $D(r\bar{\epsilon})^{-2/3}$ and the separation distance r is normalized by L_o. The statistics for F1 are plotted true, they are offset by one and two decades for F2 and F3 cases. The Ozmidov L_o and buoyancy L_b length scales are marked with solid and dotted lines, respectively.

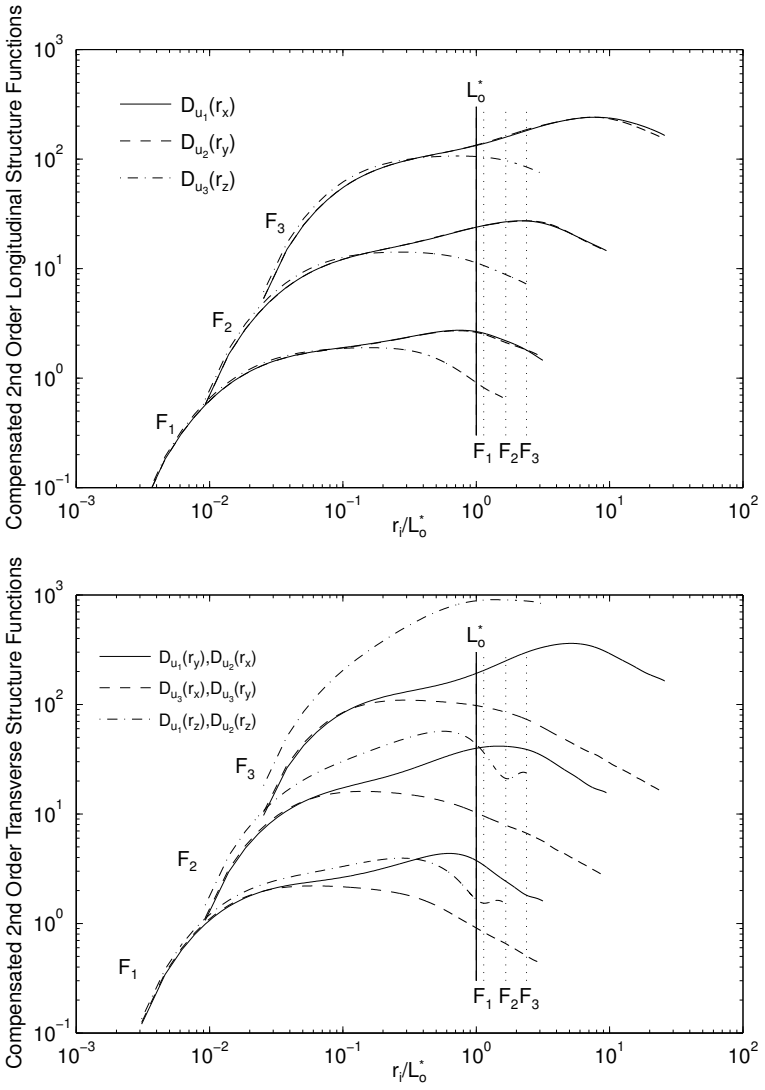

Figure 6.8: Compensated longitudinal (top panel), transverse, and vertical (bottom panel) second-order structure functions. The structure functions are normalized by Kolmogorov scaling, $D(r\bar{\epsilon})^{-2/3}$ and the separation distance r is normalized by L_o^*. The statistics for F1 are plotted true, they are offset by one and two decades for F2 and F3 cases. The Ozmidov L_o^* and buoyancy L_b^* length scales are marked with solid and dotted lines, respectively.

CHAPTER 7

SMALL SCALE DYNAMICS IN STRONGLY STRATIFIED TURBULENCE

The two main variables in analyzing small scale dynamics of turbulent flows are energy dissipation rate and enstrophy density. In this chapter, the statistical characteristics of the kinetic energy dissipation rate in strongly stratified turbulence over a range of Froude numbers are analyzed. The effect of large scale anisotropies, in terms of different Froude numbers, on the small scale turbulence are discussed. The results are compared with the statistics extracted from the isotropic homogeneous turbulence simulations with similar dynamic range and resolution to investigate universality of small scales. We apply the methodology introduced in chapter 5 for small scale studies in isotropic turbulence and modify it for anisotropic stratified flows to account for the directional dependency of the statistics. Single snapshots of cases F1, F2, F3, and R4 are chosen for this investigation. Instantaneous energy dissipation rates, ϵ_0, are computed locally using DNS data and their quantitative and qualitative differences are discussed. The effects of stratification on small scale intermittency are also investigated.

7.1 Analysis of the Local Energy Dissipation Rate

In this section, the statistical characteristics of the local kinetic energy dissipation rate is studied. Instantaneous energy dissipation rate ϵ_0 is computed locally for the stratified flows and its statistical characteristics is compared with the direct measurements of energy dissipation rate in isotropic flow. The differences are investigated both quantitatively and qualitatively. As mentioned previously, the Reynolds

numbers are in the same range for all of the simulations under the study here. The differences between the small scale statistics of the stratified and isotropic flows are discussed in terms of fundamental effects of stratification on the small scale turbulence.

7.1.1 Overview

We start our analysis with a qualitative overview of the fields in Figures 7.1 and 7.2. The contour plots of horizontal cross section of the energy dissipation rate normalized by its mean are shown in Figure 7.1 for all of the cases. The top left panel is the local energy dissipation rate in R4 case. Similar to other isotropic flows (Figure 5.1), the energy dissipation rate is organized in slender structures having width and length of approximately λ and ℓ, respectively. The size of these structures is homogeneous throughout the flow. The dissipative structures do not show any specific direction dependency.

The three other panels show the energy dissipation rate in stratified cases. There are several striking differences evident in the images of stratified cases from those of isotropic flows. It seems that by increasing the stratification level, the flow with uniform dissipative structures is transformed to a highly intermittent field consistent of large patches of high intensity turbulence surrounded by almost quasi-laminar flow. Note that the small scale slender structures are still present in the stratified flows with almost the same scales as in the isotropic flows. These structures appear smaller in the stratified images due to the higher resolution of R4 compared with the stratified simulations. As in the isotropic simulations, the dissipative structures do not exhibit any direction dependency.

Another major difference between ϵ_0 from different flows evident in the images is that ϵ_0 exhibits much sharper gradients under stronger stratifications. Note that the images are normalized by the mean value of each field and the color bar is the same

for all of the plots. By increasing the stratification level, the dissipation seems to be concentrated in the smaller patches but with stronger intensity. The size of the patches decreases by the stratification level while the intensity increases. The patches of quiescent flow expands both in size and frequency with stratification.

The vertical slices of the dissipation field are also plotted for all of the cases in Figure 7.2. In isotropic turbulence the vertical and horizontal slices through the flow are statistically similar. On the other hand, in stratified turbulence vertical statistics are affected strongly by the stabilizing effect of stratification and are very different from the horizontal statistics. These differences are apparent in the vertical slices of the stratified simulations.

The vertical slices of ϵ_0 of the stratified simulations reveal a layered flow consist of regions with high intensity separated by quiescent layers. Of course the regions with high intensity dissipation rate corresponds to regions of large velocity gradients. The existence of the layers is the very distinct characteristic of the stratified flows observed in these images. These layers start to appear in case F1 through a zig zag pattern and instability. The turbulent layers become more distinct in cases F2 and F3 while their thickness decreases by increasing stratification. The external intermittency or the patchy nature of the flow is also obvious in the images. Note that the small scales structures in the vertical direction are very similar to those shown in the plots of horizontal slices. This can be an indication of isotropic dynamics at small scale of stratified turbulence.

From the qualitative images of both horizontal and vertical slices, one can conclude that the stratification results in creation of thin layers in the flow and the shear between these layers is a source for instability and turbulence.The aspect ratio of the layers in the flow or the patches is very small. It can be hypothesized that stratified turbulence is a combination of large scale stratified flow with patches of turbulence superimposed on the dominant stratified flow. The characteristic length scales and

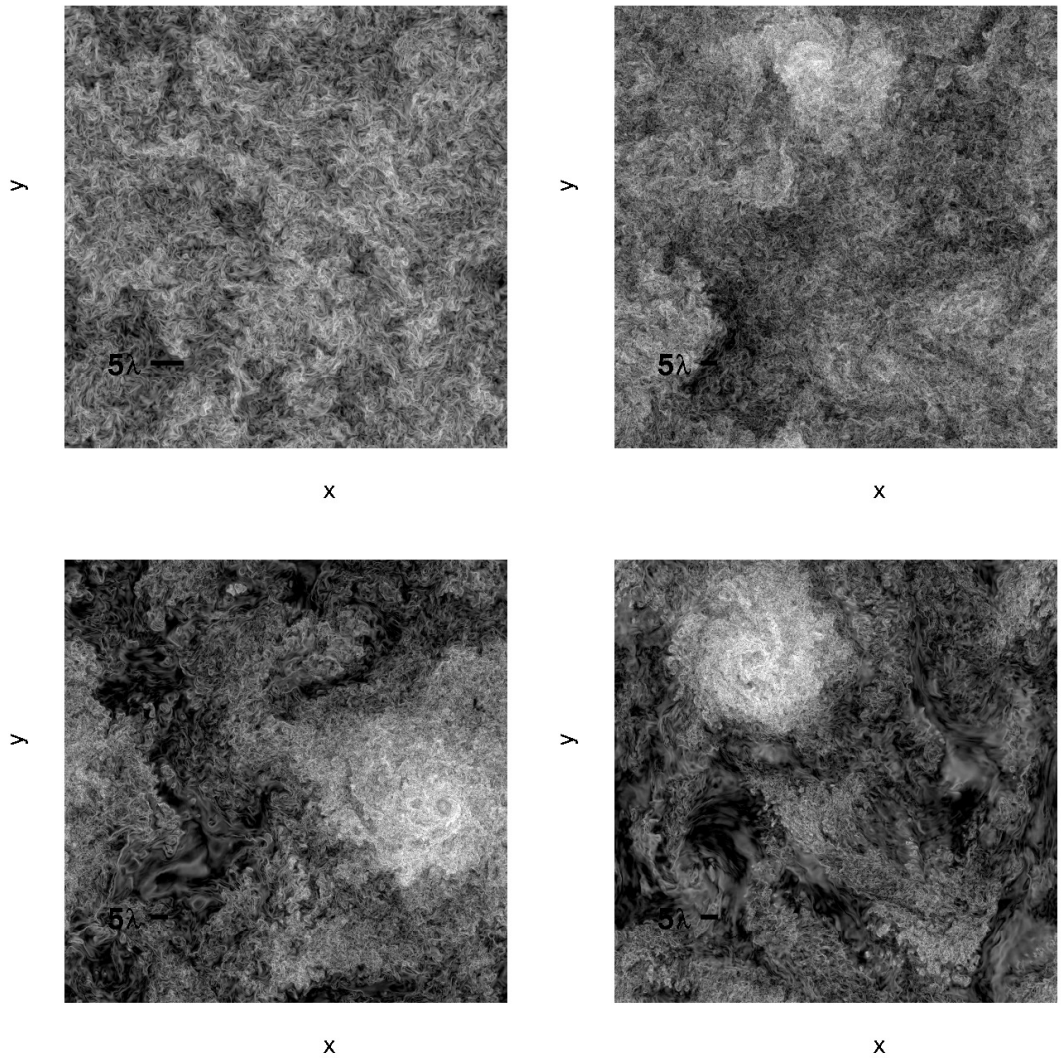

Figure 7.1: A horizontal slice of energy dissipation rate normalized by its mean value for R4 (top left), F1 (top right), F2 (bottom left), and F3 (bottom right). The shading is scaled logarithmically from 0.01 (black) to 100 (white) and is the same for all panels.

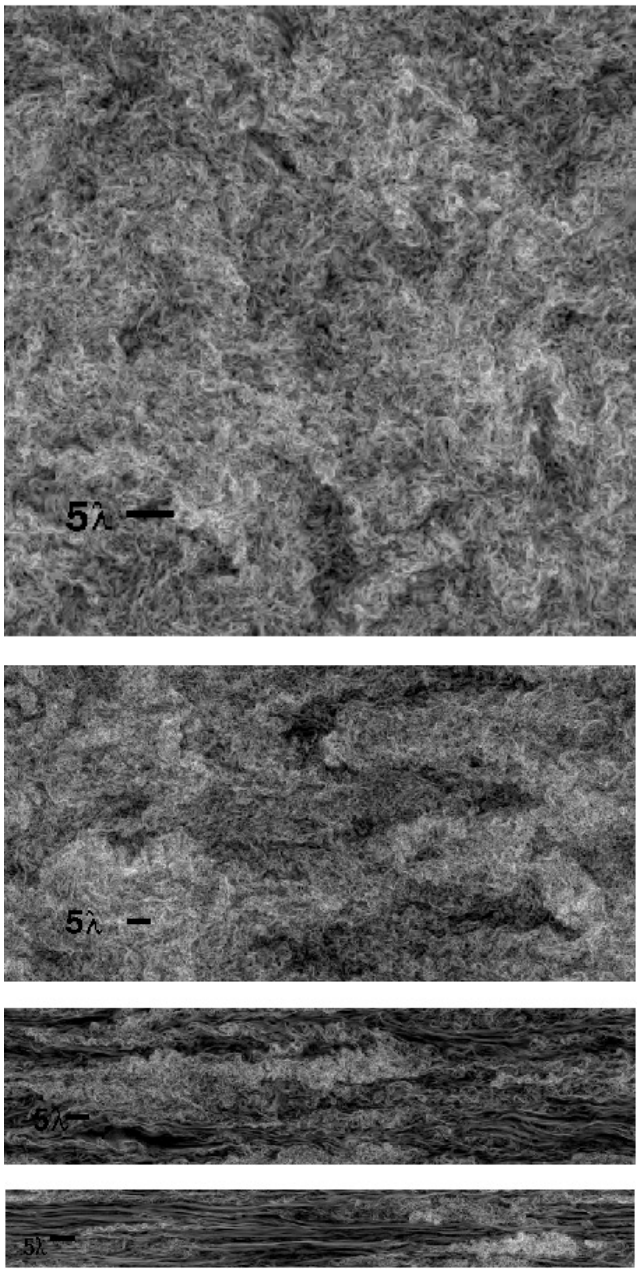

Figure 7.2: A vertical slice of energy dissipation rate normalized by its mean value from top to bottom for R4, F1, F2, and F3. The shading is scaled logarithmically from 0.01 (black) to 100 (white) and is the same for all panels.

intensity of these patches, their relationships to the Froude and buoyancy Reynolds numbers are of the main interest. These two main points will be investigated in detail in the remainder of this chapter.

7.1.2 Small-scale Resolution and Statistical Convergence

The qualitative view of the flow in Figure 6.1 and $\kappa_{\max}\eta \sim 1.5$ indicate that the velocity field is smooth and well resolved. However, the required resolution for the correct computation of the higher-order statistics, for example ϵ_0, in stratified turbulence is still an open question. The resolution $\kappa_{\max}\eta \sim 1.5$ is sufficient for correct computation of lower-order moments of ϵ_0. The validity of the conventional criteria for the isotropic turbulence, in case of stratified flow is dubious due to the effect of quiescent flow on reducing the averaged energy dissipation rate and consequently overestimating characteristic length for dissipative scales (c.f. 6.1.1). This issue can not be addressed by the current dat set and requires simulations with a range of small scale resolutions. In this research we limit our analysis to the lower-order statistics of ϵ_0 only.

Another challenge in calculating accurate statistics in the simulations other than the resolution is the statistical convergence of higher-order moments (c.f. 4.2.3). If we assume that the resolution is sufficient for nth-order moment, we still need to check the convergence of statistics for this moment with a methodology explained in § 4.2.3. The nth-order moment of ϵ_0 is statistically converged if $\epsilon_0^n P(\epsilon_0)$ of the ensemble approaches zero for large $\epsilon_0/\bar{\epsilon}$ [Donzis et al., 2008, Hamlington et al., 2012]. Here $P(\epsilon_0)$ is the probability density function of ϵ_0, which is computed by binning the data to form the histogram. The integrands for the third- and fourth-order moments of the dissipation rate are plotted in Figure 7.3. The convergence is good even up to fourth-order in all four simulations. However, we should be cautious in analyzing the

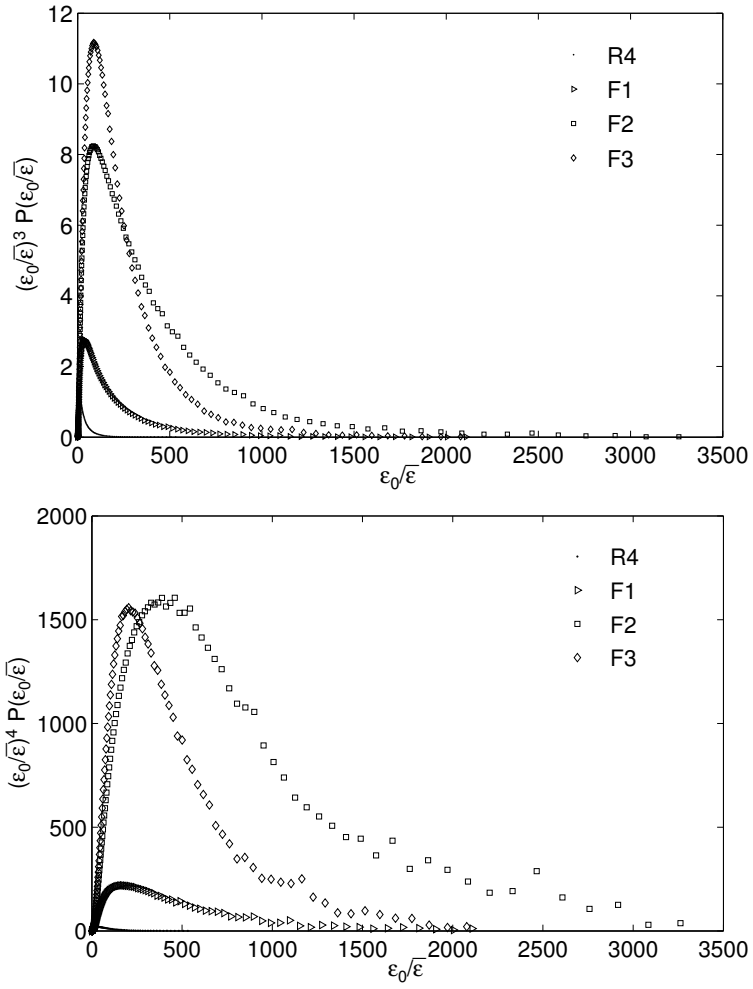

Figure 7.3: Convergence test of the third- and fourth-order moments of normalized energy dissipation rate for R4, F1, F2, and F3.

fourth-order moments of energy dissipation rate since the resolution, even based on the isotropic turbulence standards, are not sufficient for the fourth-order statistics.

7.1.3 Probability Density Functions

Modeling energy dissipation rate and its distribution is the subject of ongoing research specially in the flows dominated by large scale anisotropies. In this section the statistical characteristics of ϵ_0 in stratified flows including p.d.f.s are examined. The contribution of the components of the velocity gradient tensor on the averaged

	F1	F2	F3	R4
$\langle u_{1,1}^2 \rangle / \bar{\epsilon}$	0.0655	0.0626	0.0570	0.0667
$\langle u_{1,2}^2 \rangle / \bar{\epsilon}$	0.1268	0.1180	0.1056	0.1333
$\langle u_{1,3}^2 \rangle / \bar{\epsilon}$	0.1417	0.1615	0.1948	0.1333
$\langle u_{2,1}^2 \rangle / \bar{\epsilon}$	0.1217	0.1177	0.1055	0.1333
$\langle u_{2,2}^2 \rangle / \bar{\epsilon}$	0.0653	0.0625	0.0571	0.0667
$\langle u_{2,3}^2 \rangle / \bar{\epsilon}$	0.1411	0.1589	0.1887	0.1333
$\langle u_{3,1}^2 \rangle / \bar{\epsilon}$	0.1322	0.1247	0.1131	0.1333
$\langle u_{3,2}^2 \rangle / \bar{\epsilon}$	0.1314	0.1244	0.1129	0.1333
$\langle u_{3,3}^2 \rangle / \bar{\epsilon}$	0.0690	0.0698	0.0655	0.0667

Table 7.1: Contribution of velocity gradients on the averaged energy dissipation rate, with $u_{i,j} \equiv \partial u_i / \partial x_j$.

energy dissipation rate is listed in table 7.1. The results show that at lower buoyancy Reynolds number thee is a deviation from isotropic relations and the vertical shear ($u_{1,3}$ and $u_{2,3}$) are has higher magnitude than what is expected by isotropy. However, by increasing the buoyancy Reynolds number isotropic relations are recovered. The normalized moments of ϵ_0 are listed in table 7.2. Note that the reported variance in the table is normalized by $\bar{\epsilon}^2$. The moments are much higher in the stratified flows compared with R4. The variance increases with stratification level, while skewness and kurtosis do not follow the monotonic behavior for F3 case.

Next we consider the p.d.f.s of the local energy dissipation rate normalized by its mean. The p.d.f.s are shown on log-log and semi-log axes for all the cases in Figure 7.4. The top panel shows that the general shape of the p.d.f.s, which is consistent for all the cases while the variance increases by the stratification level. In the middle panel, the focus is on the tails of the p.d.f.s, which represent the extreme events in the flows. Energy dissipation rate is highly intermittent, as reflected in the pronounced tails of the distribution functions. When normalized by the mean value, the heavier tails of the p.d.f.s of stratified flows indicate an increase in both frequency and magnitude

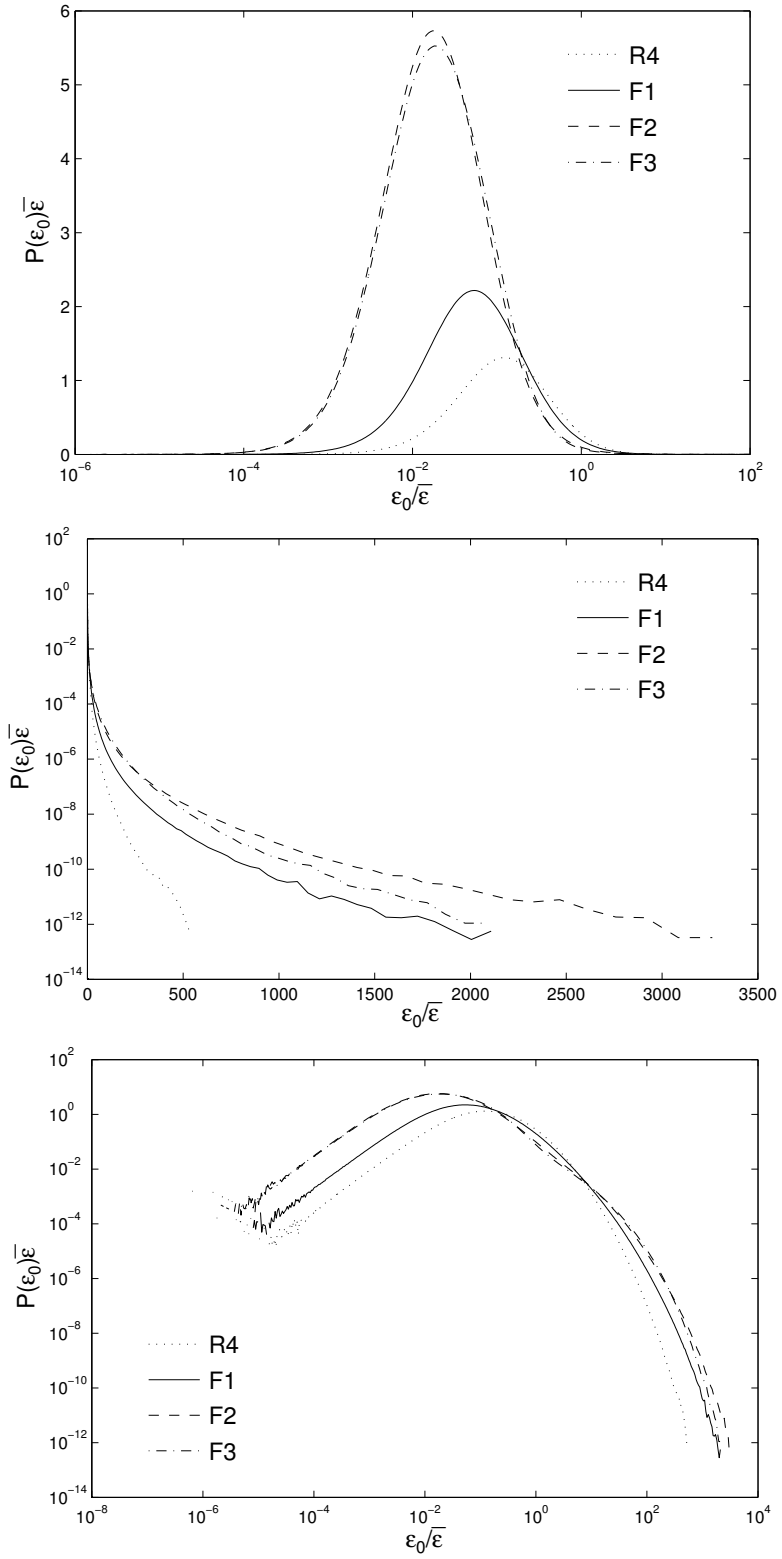

Figure 7.4: P.d.f.s of local energy dissipation rate normalized by its mean value for cases R4, F1, F2, and F3.

of the extreme events by stratification effect. In case R4, the extreme values of ϵ_0 are about 500 times the average value whereas the ratio exceeds 2000 for stratified cases. Note that for all the cases, the general shape of the tails of the distributions are consistent with the stretched exponential functions suggested in the literature [e.g. Bershadskii et al., 1993, Donzis et al., 2008, Meneveau and Sreenivasan, 1991].

In addition to the differences in the tails of the distributions related to the extreme events, there is a main discrepancy in the peak of the p.d.f.s shown in the bottom panel of Figure 7.4. In the transition from isotropic to stratified flow, the peak of the p.d.f. moves to the left side to almost an order of magnitude smaller values, and another local peak starts to appear at larger values. We hypothesize that the peak at the small magnitude represents the patches of quiescent flow and the peak at the larger magnitude represent the turbulent patches. By increasing the stratification level, the existence of two peaks and their differences are more pronounced. This effect, which is hypothesized to be related to the patchy nature of the flow and external intermittency, changes the shape of the p.d.f.s substantially and requires additional data analysis and investigations. This subject will be discussed later at the end of this chapter.

Note that the Reynolds number range is the same for all of the cases, hence the differences between the tails of the p.d.f.s can be related to the stratification effects only. To examine the effects of stratification on the intermittency and frequency of extreme events in the stratified flows, the p.d.f.s normalized by the r.m.s of ϵ_0 are plotted in Figure 7.5. The normalization of the p.d.f.s by variance instead of mean value is more appropriate due to the nature of the stratified flows and external intermittency. As noted previously, due to the presence of quiescent flow, the averaged dissipation rate is small and the variance is high in stratified flows.

Even with this normalization, stratified cases exhibit much heavier tails than the isotropic flow. Cases F1 and F2 have almost identical tails and intermittency, while

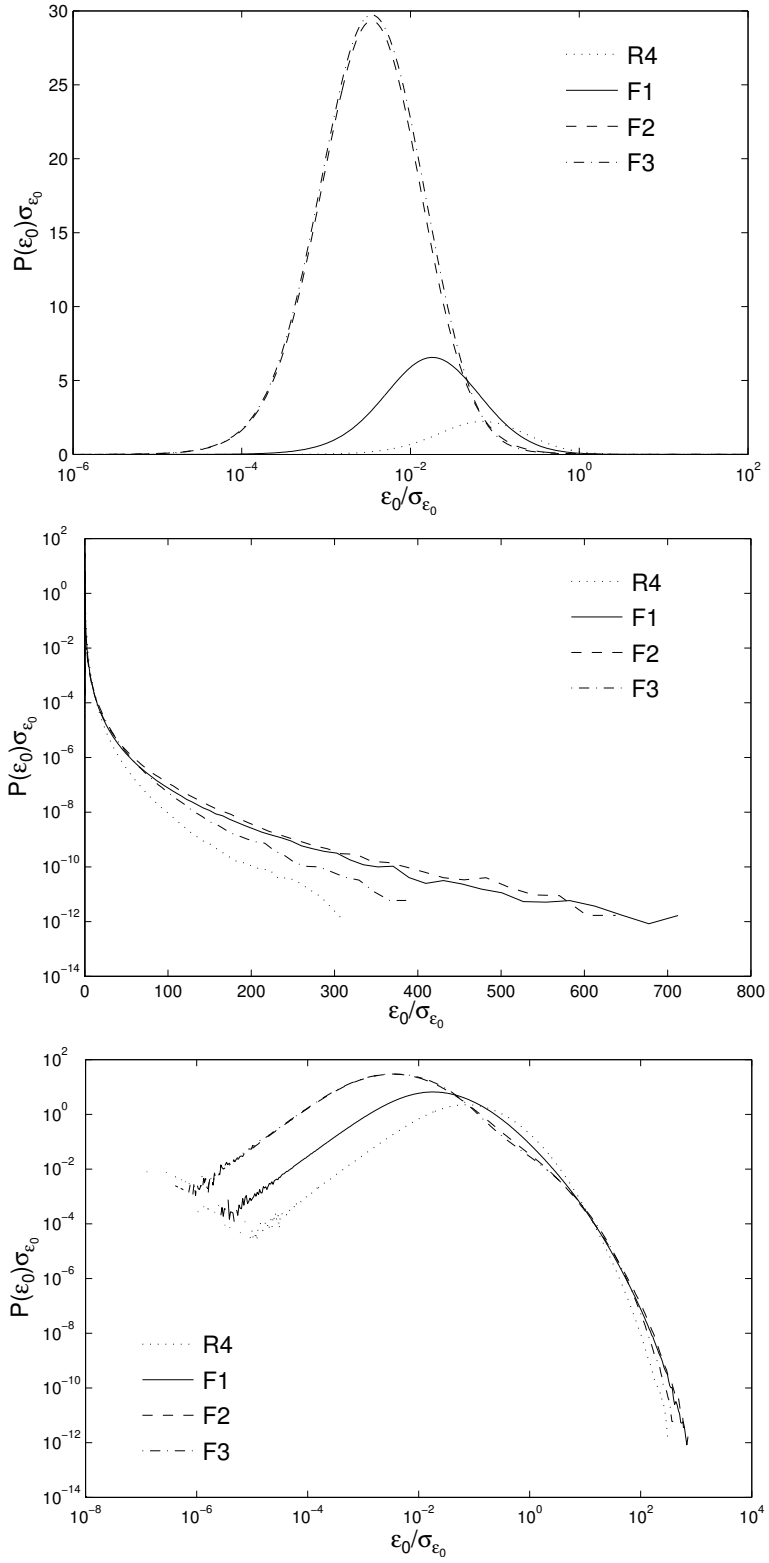

Figure 7.5: P.d.f.s of local energy dissipation rate normalized by its mean value for cases R4, F1, F2, and F3.

	Variance	Skewness	Kurtosis
R4	2.90	9.31	268
F1	8.75	23.64	1959
F2	26.18	30.70	2786
F3	28.98	21.99	1112

Table 7.2: Variance, skewness, and kurtosis of the local energy dissipation rate.

	Variance	Skewness	Kurtosis
R4	1.19	-0.058	3.07
F1	1.41	0.135	3.10
F2	1.70	0.487	3.42
F3	1.65	0.619	3.94

Table 7.3: Variance, skewness, and kurtosis of the logarithm of the local energy dissipation rate.

in case F3 the frequency of extreme events decreases slightly. It can be concluded that the frequency of occurrence of the extreme events in the stratified turbulence is not a strong function of stratification level but decreases slightly for low buoyancy Reynolds numbers.

The classical approach in modeling energy dissipation rate, *i.e.*, the lognormal model, is discussed in chapter 5. Here, we again apply this model as a reference to investigate the distribution of energy dissipation rate in the stratified flows and to verify its deviation from the isotropic flows. The p.d.f.s of the logarithm of the dissipation rate are plotted in Figure 7.6 for all of the cases along with the model distribution. The curves are scaled by the standard deviation of the logarithm of each variable, $\sigma_{\log \epsilon_0}$, in the bottom panel.

The numerical values of variance, skewness, and kurtosis of $\log \epsilon_0$ are listed in table 7.3. The normalized moments increase monotonically with the stratification level, and are much higher for the stratified flows compared with the isotropic tur-

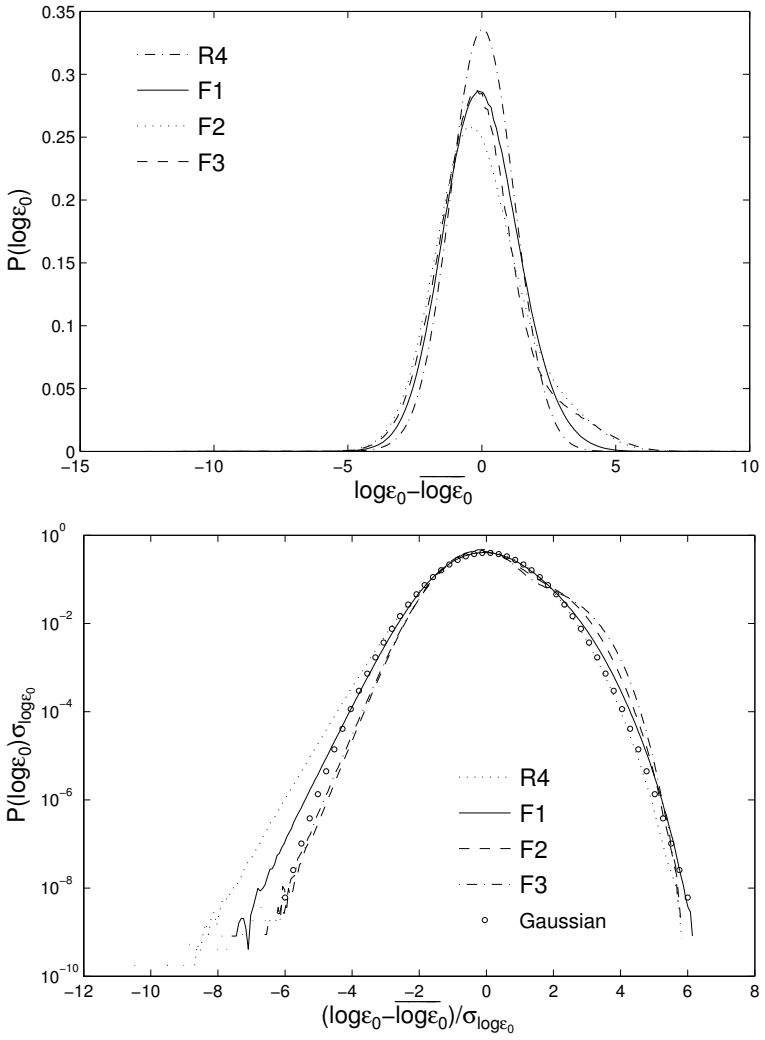

Figure 7.6: Top panel: normalized p.d.f.s of the logarithm of local energy dissipation rate for cases R4, F1, F2, and F3.

bulence. The higher skewness and kurtosis compared with the Gaussian values of 0 and 3, indicates deviation from lognormal distribution. The major discrepancy is the positive skewness of the stratified turbulence compared with the well-accepted negative skewness in the distribution of the logarithm of the local energy dissipation rate (c.f. 5.1.1). The positive skewness is in agreement with our hypothesis about the shape of the p.d.f.s and the two peaks of the distribution due to the external intermittency. Although the shape of the p.d.f.s are fundamentally different than the lognormal model, the overall deviation from this model is still smaller than what is observed for the isotropic surrogates. In contrast to the surrogates, the deviation is not due to the tails only but the general shape and body of the p.d.f.s..

7.2 Analysis of the Locally Averaged Energy Dissipation Rate

Thus far, our analysis of the local energy dissipation rate in stratified turbulence reveals some of the fundamental characteristics of stratified turbulence. While there are crucial differences in dynamics and distributions of the ϵ_0 of stratified turbulence with those of isotropic turbulence, there exist noticeable similarities specially at small scales. Our hypothesis is that the stratified turbulence consists of a dominant stratified flow with patches of turbulence superimposed on the background stratified flow. The analysis of the probability distributions of the local energy dissipation rate confirms this hypothesis with showing two peaks in the p.d.f.s. that represents these two regimes. The question of interest is the scale dependency of these regimes and the range of the scales that this transition in dynamics occurs. To approach this question, we apply the methodology introduced in § 5.2, namely the statistical analysis of locally averaged variables. To our knowledge this is the first time this methodology is applied in non-isotropic flows.

In chapter 5, the locally averaged energy dissipation rate is defined as ϵ averaged over a volume with *linear* dimension r. Stratified flows, however, are not isotropic at

all length scales and exhibit different dynamics, and consequently characteristic length scales in horizontal and vertical directions (c.f. 7.1.1). Therefore, the volumetric spherical averaging has no obvious interpretation. The locally averaged variables for stratified turbulence, are defined as linear averages of local energy dissipation rate instead of spherical averages . The differences between the spherical and linear locally averaged variables are discussed for isotropic turbulence in § 5.2. To account for the directional statistics, we define the linear locally averaged variables in two horizontal (x, y) and vertical (z) directions using the methodology introduced in § 5.2 and derivation in appendix B as below:

$$\epsilon_{r_x}(\boldsymbol{x}) = \bar{\epsilon} + \int_{-\infty}^{\infty} e^{i\kappa_1 x_1} \hat{\epsilon}_0(\boldsymbol{\kappa}) \frac{\sin(\kappa_1 r/2)}{\kappa_1 r/2}\, d\kappa_1, \tag{7.1}$$

$$\epsilon_{r_y}(\boldsymbol{x}) = \bar{\epsilon} + \int_{-\infty}^{\infty} e^{i\kappa_2 x_2} \hat{\epsilon}_0(\boldsymbol{\kappa}) \frac{\sin(\kappa_2 r/2)}{\kappa_2 r/2}\, d\kappa_2, \tag{7.2}$$

$$\epsilon_{r_z}(\boldsymbol{x}) = \bar{\epsilon} + \int_{-\infty}^{\infty} e^{i\kappa_3 x_3} \hat{\epsilon}_0(\boldsymbol{\kappa}) \frac{\sin(\kappa_3 r/2)}{\kappa_3 r/2}\, d\kappa_3, \tag{7.3}$$

where κ_i is the wave number in the ith direction. Note that It is sometimes noted that (7.1)-(7.3) are not, in general, exact for simulation data, which is true if ϵ_0 cannot be exactly represented in Fourier space by $\hat{\epsilon}_0$. In fully dealiased pseudospectral simulations of the type reported here, ϵ_0 is described exactly by a finite discrete Fourier series and, therefore, by a Fourier integral with the coefficient function zero except at certain wave numbers. Since (7.1)-(7.3) do not introduce Fourier modes that are not in ϵ_0, ϵ_r reported here are exact to within the precision of the computer arithmetic.

7.2.1 Moments of Locally Averaged Energy Dissipation Rate

We begin our analyses with the moments of the locally averaged energy dissipation rate in all three directions. The statistics in the two horizontal directions (x, y) are almost identical and only one of them is presented in the remainder of this chapter. Note that we limit our analysis to the second-order moment, since we are uncertain

about the required resolution of simulations for the higher-order moments of the stratified turbulence (c.f. 7.1.2).

The linear averaged energy dissipation is computed in three different directions for all the cases. The second-order moment of the horizontal averages are plotted in Figure 7.7 for the isotropic case, R4, and all three stratified cases, F1, F2, and F3. The Taylor microscale and horizontal integral length scales are also marked on the plot. Similar to the isotropic turbulence the moments show a power law scale dependency. In stratified turbulence, however, there are two distinct regions with different power law dependency. At small and medium scales the slope is similar to the isotropic case, while at larger scales the slope is much steeper. Also, there is a slight variation in the slope with stratification levels. For a precise examination of the slopes, the local scaling exponents

$$\tau(n,r) \equiv -\frac{d(\log\langle\epsilon_r^n\rangle)}{d\log r}$$

are computed with the same methodology explained in § 5.3.1. The local scaling exponents corresponding to the second-order moments of the horizontal averages are plotted in the bottom panel of Figure 7.7.

This figure reveals many remarkable characteristics of stratified turbulence. At small scale ($\sim \lambda$), the flow structures follow isotropic turbulence closely. It is hypothesized in the theory of isotropic turbulence that locally averaged energy dissipation shows a power law scaling over inertial range, which implies a plateau in the slope. As discussed in § 5.3.1 and as it is shown in this figure for case R4, the local slope increases to a maximum value at scales of $r \sim \lambda$ and shows a slight plateau region. Then the slope monotonically decreases to zero at large scales. The magnitude of the averaged slope is in good agreement with intermittency exponent $\mu = 0.25 \pm 0.05$ reported from high Reynolds number flow measurements and accepted as universal value in the literature.

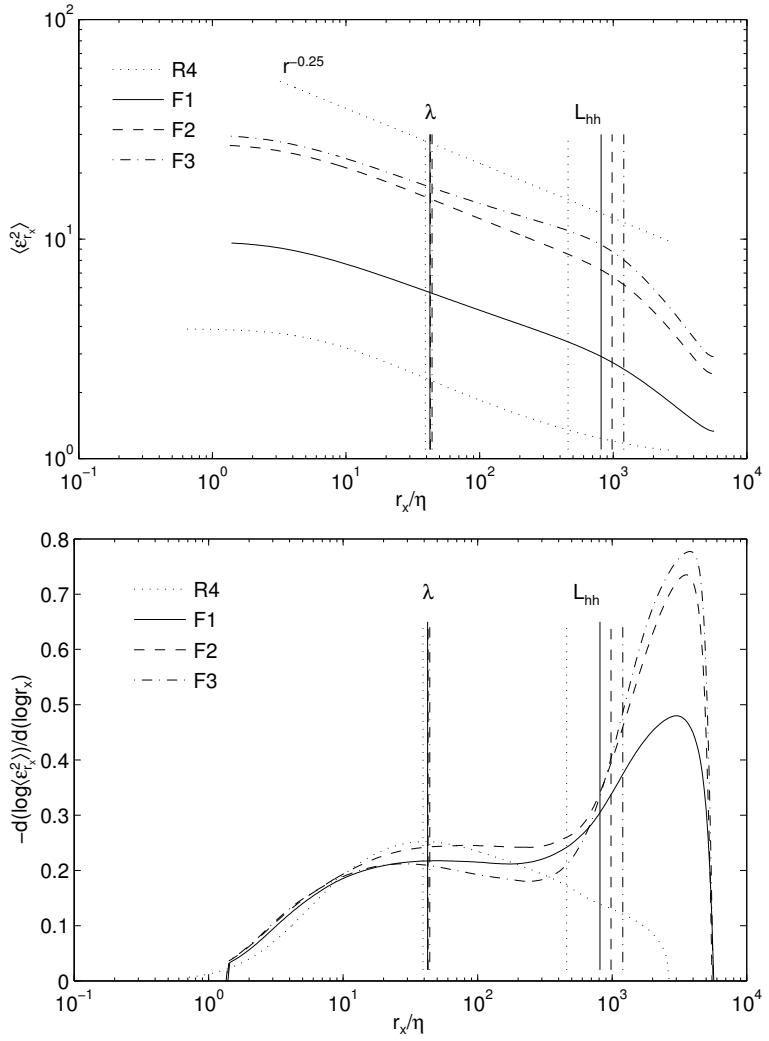

Figure 7.7: The scale dependency of the second-order moments (top panel) and corresponding slopes (bottom panel) of the locally averaged energy dissipation rate in the horizontal direction x for R4, F1, F2, and F3 cases. Taylor microscale and horizontal integral length scale are marked for each case using the same symbols shown in the legend.

The stratified flow with the same dynamic range and Reynolds number, exhibits a distinct plateau at the small and medium scales ($r \sim \lambda$). This plateau extends over almost a decade of scales up to buoyancy length scale. This is a remarkable observation since such plateau has not been observed for the isotropic turbulence. The magnitude of the slope is also in good agreement with the universal intermittency exponent of isotropic flows. Note the slight change of the local slope over the plateau region for different stratification levels. For F1 and F2 cases the extension of this region is almost the same, while F2 shows slightly higher slope compared with F1. The trend is not monotonic for F3 case and the magnitude of the local slope decreases, especially at scales larger than λ. The lower intermittency exponent for F3 is in agreement with the shorter tails of the p.d.f. of ϵ_0 in this case discussed in the previous section. It is anticipated that the small scale intermittency and frequency of extreme events descend in F3 due to stabilizing effects of stronger stratification.

At scales larger than the buoyancy length scale, the slope of the curves starts to increase monotonically for all three cases and at the scales larger than the integral length scale, they start to form a second plateau with a magnitude much higher than the intermittency exponent in the inertial range. In other words, the moments of energy dissipation rate averaged over the scales larger than the high intensity turbulent patches, change drastically with scale most likely due to the patchy nature of the flow. The higher local slope at large scales indicate intermittency at large scales or the so-called external intermittency, which is caused by the anisotropic nature of the flow. The magnitude of the slope at these scales changes monotonically by the stratification level. The higher stratification results in the higher slope and consequently stronger external intermittency.

It is remarkable that the dynamics of the small scale turbulence in stratified flows, which are dominated by substantially different large scale dynamics, are very close to the dynamics of isotropic flows. This observation supports the theory of universality

at small scales. For a complete and comprehensive analysis of energy dissipation rate dynamics in stratified turbulence, the vertical statistics are considered next.

The moments of the locally averaged energy dissipation rate in the vertical direction and their corresponding slopes are plotted in Figure 7.8 for all of the cases. Note that the extension of the scales in the vertical direction is different for each case and corresponds to the outer vertical scale of the flow. Similar to the horizontal statistics, the moments exhibit power law scaling with slopes close to the isotropic value. The distinct plateau over the middle scales in the local scaling exponents of the stratified cases is an indication for such power law scaling. While the magnitude of the slope is in the range of accepted intermittency exponent for all the cases, there is a slight variation between the different stratification levels. Note that the uncertainty in these statistics are not measurable with the current data set.

Due to isotropy, the vertical and horizontal statistics of R4 are similar, while there are distinct differences between the statistics of the horizontal and vertical averages in the stratified flows. The second-order moment of locally averaged energy dissipation and corresponding slopes on all of the three directions are plotted in Figures 7.9 and 7.10, respectively. At small and medium scales the vertical and horizontal averages are very similar indicating local isotropy for the stratified flows at these scales. At the scales beyond the buoyancy length scale, the dynamics are directional and exhibit very different characteristics in the vertical and horizontal directions. The statistics of the vertical averages are similar to the isotropic flows where there is no indication of large scale structures. On the other hand, the statistics of the horizontal averages show large scale structures in the flow and indicate external intermittency. The external intermittency is stronger at higher stratification levels.

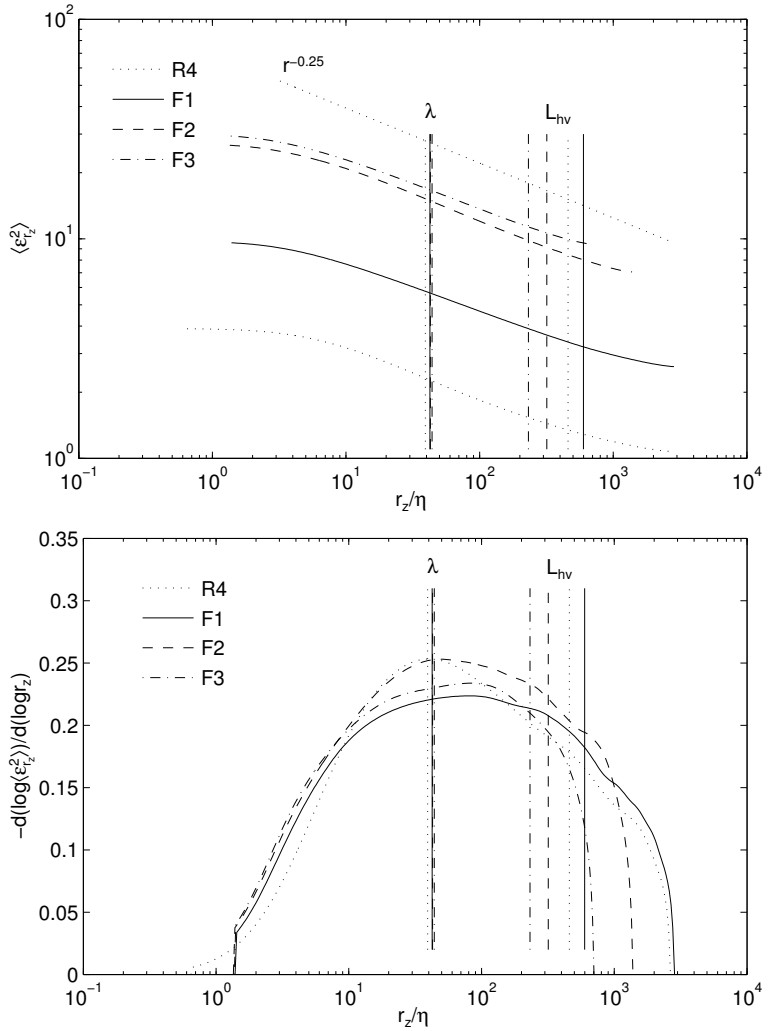

Figure 7.8: The scale dependency of the second-order moments (top panel) and corresponding slopes (bottom panel) of the locally averaged energy dissipation rate in the vertical direction z for R4, F1, F2, and F3 cases. λ and L_{hv} are marked for each case using the same symbols shown in the legend.

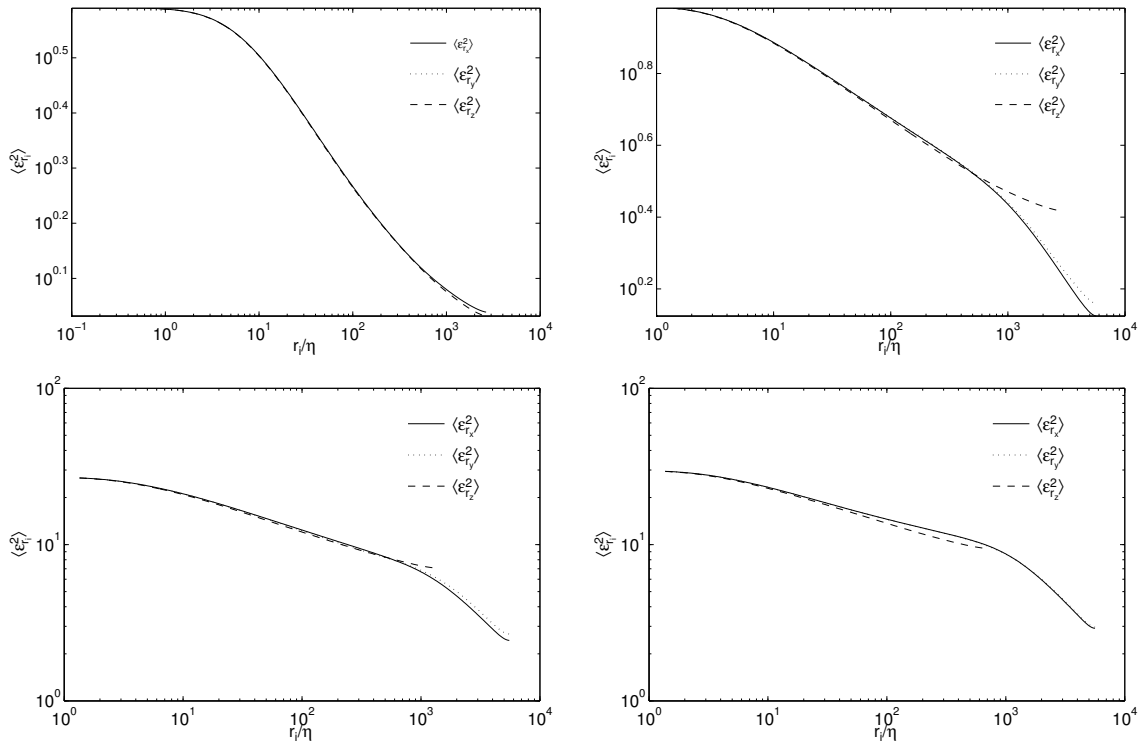

Figure 7.9: The scale dependency of the second-order moments of the locally averaged energy dissipation rate in all three directions for R4 (top left), F1 (top right), F2 (bottom left), and F3 (bottom right) cases.

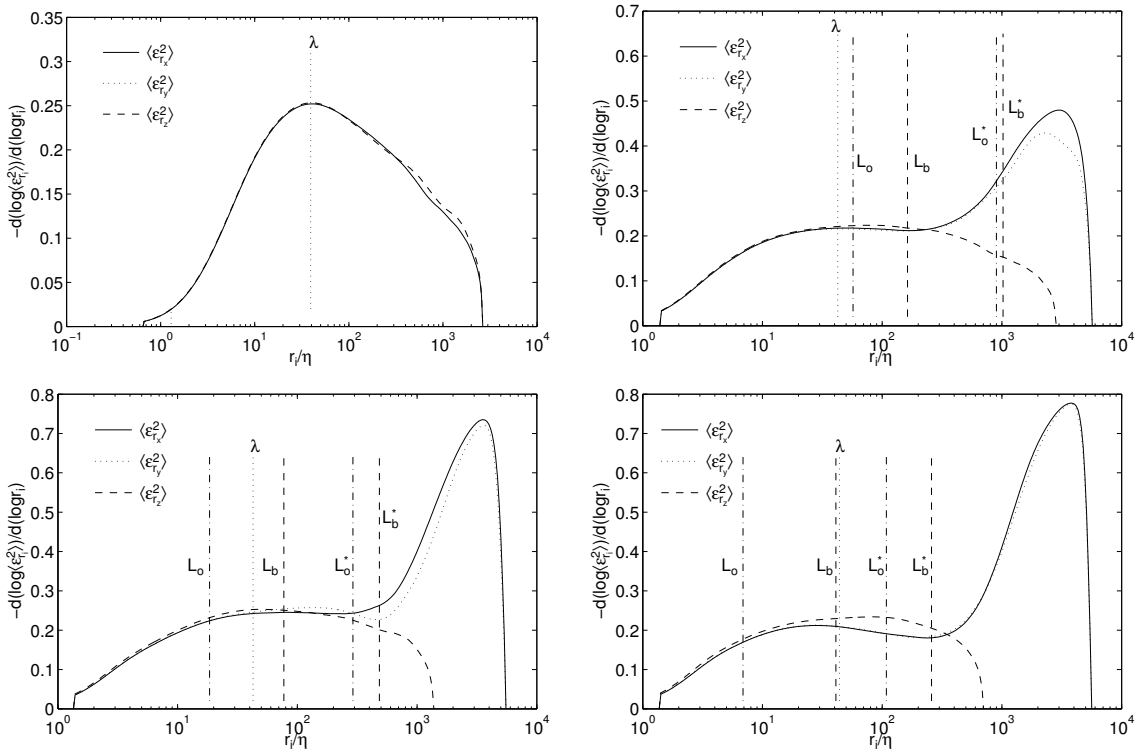

Figure 7.10: The local scaling exponents of the second-order moments of the locally averaged energy dissipation rate in all three directions for R4 (top left), F1 (top right), F2 (bottom left), and F3 (bottom right) cases. The two different definitions of Ozmidov and buoyancy length scales are also marked on the plots.

7.2.2 Autocorrelation Functions and Spectra of Energy Dissipation Rate

The relationships between the autocorrelation function of the local energy dissipation rate and the second-order moments of locally averaged energy dissipation rate in isotropic turbulence were discussed in § 5.3. This hypothesis is valid for the homogeneous turbulence [Monin and Yaglom, 1975, §25]. Thus, the relationship between the scaling of autocorrelation function and the second-order moments is expected to be valid for the stratified turbulence as well. The autocorrelation function of the local energy dissipation rate, similar to the other directional statistics, are defined in three directions, x, y, and z. For example in x direction:

$$R^x_{\epsilon_0}(r_x) \equiv \langle \epsilon_0(\boldsymbol{x})\epsilon_0(\boldsymbol{x}+r_x)\rangle \ , \tag{7.4}$$

The autocorrelation functions of the local energy dissipation rate in both horizontal and vertical directions are plotted in Figure 7.11 for all of the cases. These statistics are compared to the second order moments of locally averaged energy dissipation rate in Figure 7.12. The curves of the stratified cases show an extensive power law scaling range with a slope similar to the isotropic case. Similar to the moments of locally averaged energy dissipation rate, there are two distinct power law scaling ranges. At smaller scales the slope is in agreement with intermittency exponent. At larger scales, the slope is much steeper indicating the external intermittency. However, there is a distinct difference between the numerical values of the slopes of autocorrelation functions and the moments at larger scales. The spectra of the local energy dissipation rate is also shown in Figure 7.13. As expected, the spectra also exhibit power law scaling and the slope is consistent with the intermittency exponent μ. Note that by assuming a power law scaling for autocorrelation function of ϵ_0 with slope $-\mu$, it can be deduced that the spectrum will exhibit power law scaling in the scaling range $E_{\epsilon_0} \sim \kappa^{\mu-1}$.

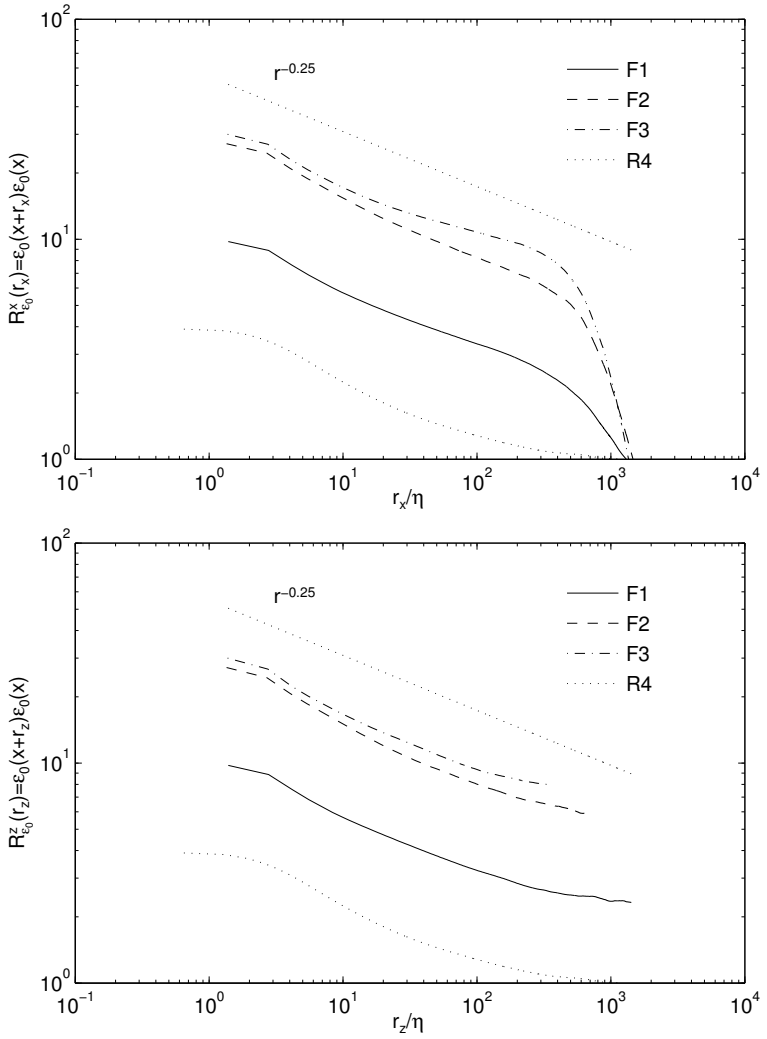

Figure 7.11: The autocorrelation functions of local energy dissipation rate in horizontal (top panel) and vertical (bottom panel) directions for F1, F2, F3, and R4.

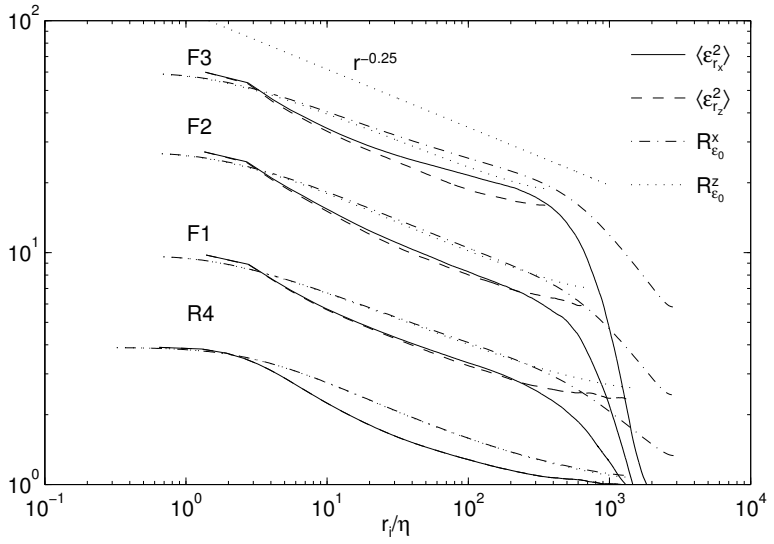

Figure 7.12: The second-order moment of locally averaged dissipation rate and the autocorrelation function of local energy dissipation rate in both horizontal and vertical directions for all of the cases. The results for R4 are plotted true and for other cases shifted up for clarity of the figure.

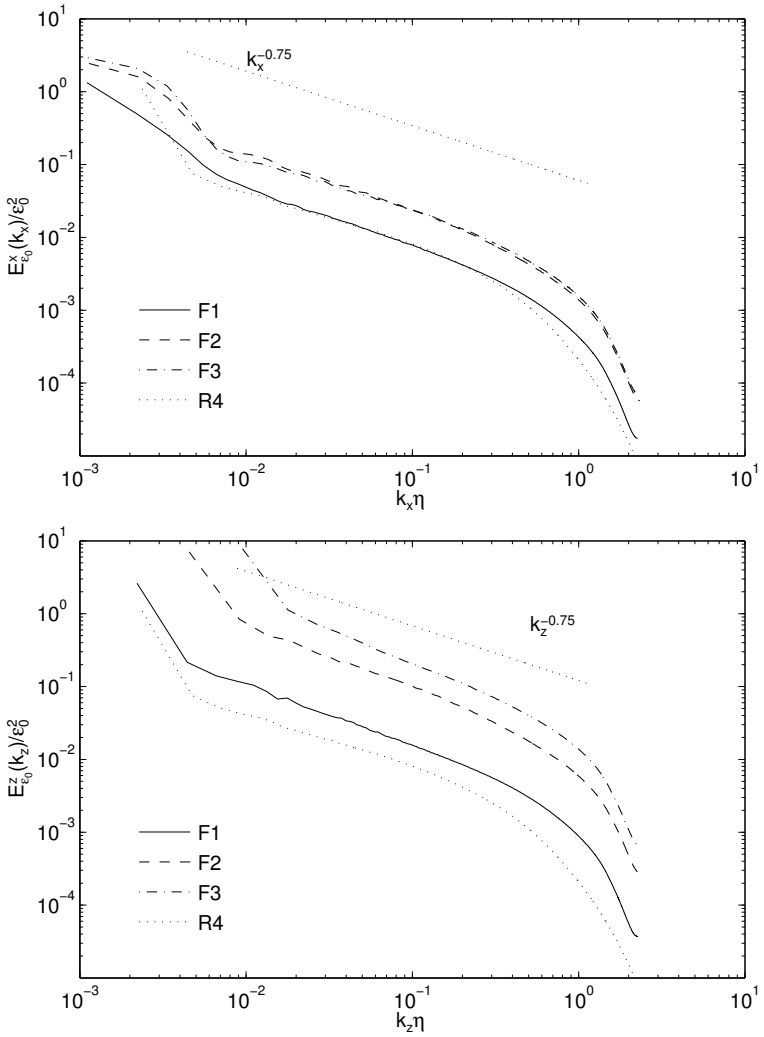

Figure 7.13: The one-dimensional spectra of local energy dissipation rate in horizontal (top panel) and vertical (bottom panel) directions for F1, F2, F3, and R4.

CHAPTER 8

SUMMARY AND CONCLUSIONS

A systematic methodology based on direct numerical simulations of turbulent flows is developed to understand aspects of small scale turbulence. Understanding characteristics of the small scale intermittency in turbulent flows and the accuracy of the models and theories for intermittency are the main objectives. The research is designed to address two central questions; 1) possible effects of large scale anisotropies on the small scale turbulence and 2) potential biases in characterizing small scale turbulence due to the nature of surrogates of energy dissipation rate.

Direct numerical simulations of isotropic homogeneous turbulence with a range of Reynolds numbers, and stably stratified turbulence with a range of Froude numbers are considered. Isotropic homogeneous turbulent flows are analyzed first to provide a clear insight to the small scales in the absence of large scale anisotropy. The density stratified turbulent flows with different levels of stratification, which causes different levels of large scale anisotropy, are considered next. The structures of small scale turbulence are described in terms of the dissipation rate of turbulent kinetic energy. A number of surrogates of energy dissipation rate are also considered. The surrogates are the key variables in extracting small scale turbulence in physical measurements. The efficiency and accuracy of the surrogates are investigated using simulations of isotropic turbulence. Their usefulness in the presence of large scale anisotropy remains an open question and suggested as future work. A summary of the results are discussed in the following sections.

8.1 Isotropic Turbulence

Direct numerical simulations of forced, isotropic homogeneous turbulence with extraordinarily fine spatial resolution up to $\kappa_{max}\eta \approx 6$ on a very large domain with up to 4096^3 grid points, were computed and analyzed to understand aspects of small scale intermittency in the absence of large scale anisotropies. The general characteristics of the flows are investigated in terms of statistics of local velocity, velocity gradients, energy spectra, and structure functions. Note that even the most powerful computers do not enable sufficient dynamic range in simulations to satisfy all of the assumptions underlying small scale theories; nevertheless, the simulated flows are well resolved and their characteristics are fully consistent with those reported in the literature for high Reynolds number flows. The small scale isotropy is observed through an investigation in terms of invariants of velocity gradients up to the fourth-order. The statistics of local and locally averaged energy dissipation rate are applied to characterize small scale turbulence and to quantify intermittency.

The surrogates of energy dissipation rate that are based on measurements of a subset of the strain rate tensor are considered. In particular, the one-dimensional longitudinal and transverse surrogates, as well as a surrogate based on the asymmetric part of the strain rate tensor, are analyzed in detail. These surrogates are selected since they are considered as the characteristic building blocks of the energy dissipation rate and reflect different structural information of the flow. The instantaneous surrogates are studied locally, locally averaged in space, and conditionally averaged to see what statistics of the dissipation rate might accurately be inferred given measurements of the surrogates.

Significant differences between the energy dissipation rate and its surrogates are observed. Generally the one-dimensional surrogates exhibit extreme events much stronger and more frequent compared with those in the energy dissipation rate. A simple explanation for this behavior is that the extreme events of the one-dimensional

components average out due to the summation in the dissipation rate [Wang et al., 1996]. In other words, the summation of multiple intermittent random variables is a less intermittent random field if the original fields are independent. If this theory is correct then, presumably, averaging in space over lengths larger than η but smaller than ℓ will result in comparable statistics for the dissipation rate and surrogates. The DNS data show that even with averaging volumes approaching ℓ the surrogates are significantly more intermittent than the dissipation rate. So it appears that cancellation of rare events by averaging does not explain why dissipation rate is less intermittent than the surrogates.

Another explanation for why the surrogates are more intermittent than the dissipation rate is that multiple types of structures generate extreme events in the flow and each velocity derivative reflects only some of these structures whereas the energy dissipation rate captures the comprehensive effect. Our statistical analysis of the longitudinal, transverse, and asymmetric surrogates reveal fundamental differences between these variables and supports this explanation. All of the surrogates are more intermittent than the dissipation rate, the transverse surrogate is more intermittent than the longitudinal. As a consequence, the intermittency exponent computed from the moments of the locally averaged longitudinal and transverse surrogates is approximately 1.5 and 2.2 times higher, respectively, than the one computed by the same method from the dissipation rate field. Consistent with our results is the differences between the scaling exponents of longitudinal and transverse structure functions, which have been reported previously [e.g. Benzi et al., 2010, Biferale and Procaccia, 2005, Boratav and Pelz, 1997, Chen et al., 1997a,b, Dhruva et al., 1997, Grossmann et al., 1997, Shen and Warhaft, 2002]. Whether these effects are artifacts of finite Reynolds number is an open question.

An important use of surrogates is to predict the statistics of the dissipation rate for use in modeling. The classical model is the two-parameter lognormal distribution. For

it to be effective using surrogate measurements then the mean and standard deviation of the dissipation rate and the surrogate would have to be comparable. The surrogates are defined so that their mean values are exact. The p.d.f.s of the longitudinal and transverse surrogates are so much different from that of the dissipation rate, however, that the two-parameter lognormal model is not effective. It is not straightforward to accurately estimate the probability distribution of the dissipation rate given either the longitudinal or transverse surrogate.

Several methods are used to quantify intermittency from the dissipation rate and from the surrogates. Since the surrogates have more frequent extreme events, it is perhaps not surprising that the results show the longitudinal surrogate yields a higher value of μ than does the dissipation rate, and the transverse surrogate a higher value yet when a one-for-one substitution is made of the dissipation rate with the surrogate. Importantly, while all the methods yield similar values of μ based on the dissipation rate, the values of μ based on the surrogates are inconsistent. This might be an artifact of the moderate Reynolds number of the simulations affecting the different methods for quantifying intermittency to different degrees. However, while the new results are more comprehensive than those in the literature they are in complete agreement with high Reynolds number results where comparisons can be made [e.g. Cleve et al., 2003, Hao et al., 2008, Praskovsky and Oncley, 1997, Zhou et al., 2006]. This suggests that while the numerical values for μ reported here may be influenced by Reynolds number, the tendency for the surrogates to overestimate μ, and for the estimates to depend on the method used to compute it, require further study.

A further step in understanding the behavior of the surrogates is to examine contribution of each component on energy dissipation rate. To do so, we examine conditional statistics of the surrogates on the dissipation rate. One might expect that the average of a surrogate at all the spatial locations having a particular value of the dissipation rate would average to that dissipation rate. This is the case for

the longitudinal surrogate, but not for the transverse or asymmetric surrogate. Even averaging locally in space and then conditionally averaging the transverse surrogate does not result in fortuitous cancellation of extreme values and cause the statistics of the surrogate to be comparable to those of the dissipation rate.

8.2 Stratified Turbulence

To investigate characteristics of the small scale turbulence in complex flows, *i.e.,* the flows dominated by the large scale anisotropy, stably stratified turbulence is studied. Understanding behavior of turbulence when the effects of buoyancy are strong is important in its own right. Here, buoyancy is used simply as a convenient way to create a homogeneous but anisotropic flow. Direct numerical simulations of forced, homogeneous and axisymmetric flow with a range of density gradients in the vertical direction were computed to understand aspects of small scale turbulence in stratified flows. There is no mean shear, and no internal waves were intentionally introduced into the simulations so that the turbulence in the flows results primarily from instabilities in horizontal layers that spontaneously form. Numerical forcing was used to represent persistent motions at large horizontal length scales. Numerical grids with up to $4096 * 4096 * 2048$ grid points provide more than three decades of scale separation between the length scale of the forcing and the smallest length scales in the flows. As a result, the direct numerical simulations of stratified flows with horizontal Froude numbers of $\mathcal{O}(1)$ or smaller include buoyancy Reynolds numbers well above the often-accepted threshold value of 30, necessary for the flows to be strongly turbulent [Gibson, 1980, Gregg, 1987, Imberger and Boashash, 1986, Smyth and Moum, 2000].

The overview of the flow is provided in terms of local velocity, one-dimensional energy spectra, and structure functions. The flows exhibit a patchy nature with a layered structure. The characteristic length scale of the turbulent patches are much

smaller in the vertical direction than the horizontal direction and the aspect ratio of these layers increases by the stratification level. As a result, the statistics are directional. Note that unlike isotropic homogeneous turbulence, there are not many well-established theories and models for stratified turbulence, and the statistics are investigated qualitatively and quantitatively with limited comparison to the theory and models.

There is a net downscale energy transfer in both horizontal and vertical directions. The one-dimensional spectra of horizontal and vertical velocities show a power law scaling over an extensive range of scales. The vertical component of the velocity field in stratified turbulence is affected strongly by the stabilizing effect of stratification, and as a result its dynamics are very similar to the velocity field in the three-dimensional isotropic turbulence. The spectra of vertical velocity in both horizontal and vertical directions exhibit a $-5/3$ slope over an extensive range of scales. In other words, the vertical velocity develops mostly inside the turbulent patches in stratified turbulence. Horizontal velocity, however, is affected by both turbulence and stratification and has many different characteristics than the vertical component. The spectra of horizontal velocity in horizontal direction show a $-5/3$ slope over a broad range of scales. The vertical spectra of the horizontal velocity exhibit a much steeper slope. The slope is a function of stratification level and approaches -3 for the strongest stratification.

The scaling range corresponding to the $-5/3$ slope in the stratified turbulence is much wider compared with the scaling range of isotropic turbulence. This can be explained perhaps due to the multiple mechanisms resulting in the same power law scaling. The $-5/3$ scaling extends over two wave number bands: the range of scales smaller than Ozmidov length scale, which corresponds to the three-dimensional turbulence, and the range between the Ozmidov and buoyancy scales, which corresponds to the stratified turbulence. The scaling of the second-order structure functions sup-

ports this hypothesis by showing two different power law scalings over this range of scales. At smaller scales of this range, the $-5/3$ scaling of spectra corresponds to $2/3$ scaling of the structure functions, as it is expected in the isotropic turbulence (Kolmogorov-Obukhov scaling). However at larger scales of this range, the $-5/3$ scaling of the spectra corresponds to the scaling of structure functions much higher than $2/3$. This region most likely represents the inertial range of stratified turbulence.

At this point we are unable to identify a consistent scaling range of spectra and structure functions in terms of characteristic length scales of stratified turbulence for all the cases, most likely due to the limited dynamic range provided by DNS and effects of buoyancy Reynolds number. More research is required, with flows having broader scaling ranges and higher resolutions, to determine a self similar scaling in terms of characteristic length scales.

The statistical analysis of the energy dissipation rate suggests a general picture for the stratified turbulence as a superposition of two different flow regimes: a dominant stratified flow with patches of three-dimensional turbulence superimposed on this background flow. The background stratified flow is dominated by the large scale anisotropy and is almost two-dimensional. This qualitative picture is supported by visualizing the local energy dissipation field, its distribution, and scale dependency of the moments of locally averaged energy dissipation rate.

The shape of the probability density functions of energy dissipation rate changes by increasing stratification to reveal these two flow regimes. The probability density functions show two peaks or local modes, which are the representatives of the patches of turbulence and patches of quiescent flow with much smaller mean value compared with the turbulent patches. The separation between these two local modes and changes in the shape of distributions increase with stratification level.

The scale dependency of the moments of locally averaged energy dissipation rate not only reveals these two regimes, but also quantifies the intermittency related to

each of them. In general moments of locally averaged energy dissipation rate show power law scaling as predicted by the theory for the isotropic turbulence. Two distinct scaling ranges are observed.

At small and medium scales the power law is in a very good agreement with the theory of small scale intermittency and reveals an intermittency exponent in the range of reported value of $\mu = 0.25 \pm 0.05$. This occurs in all three directions, indicating the three-dimensional and isotropic nature of the intermittency of the turbulent patches. Note that such an extensive scaling range has not been observed for the isotropic turbulence at least within the range of Reynolds numbers that has been studied. Whether this is an artifact of the simulation or a property of turbulent flows can not be answered with the current simulations and requires further investigations.

A power law scaling is also observed at larger scales but with much higher exponent that is changing with stratification level. This scaling represents intermittency at larger scales or the so-called external intermittency, which is a strong function of large scale anisotropies and only occurs in the horizontal direction. The autocorrelation function of the local energy dissipation rate also reveals internal and external intermittency qualitatively by exhibiting power law scaling with two separate scaling exponents. Spectra of the dissipation rate also reveal small scale intermittency exponent comparable with the reported value in the literature.

The key conclusions from this research are summarized below:

- Direct numerical simulations of isotropic turbulence with extraordinary resolution and range of Reynolds number and stratified turbulence with an extensive dynamic range and range of Froude numbers are designed to investigate small scale universality in turbulent flows.

- Statistical analysis of locally averaged energy dissipation rate is applied as a powerful tool in investigating scale dependency of the flow dynamics.

- Small scale intermittency manifested in energy dissipation rate is independent of large scale anisotropies and can be quantified consistently using different methods.

- The general shape of the p.d.f. of energy dissipation rate is a function of large scale flow and, therefore, is not universal. The distribution of the extreme and intermittent events, which corresponds to the tails of p.d.f.s, however, is not changing with the large scale anisotropies.

- The surrogates of energy dissipation rate are fundamentally different than energy dissipation rate and their p.d.f.s. differ from those of energy dissipation rate, drastically.

- The discrepancy between different surrogates indicates geometry dependency of intermittency, at least in the range of Reynolds numbers considered here.

- The longitudinal surrogate is the best representative for the energy dissipation rate in estimating intermittency exponent .

- It is proposed that stratified turbulence is a combination of two dominant flow regimes including isotropic turbulent patches superimposed on the background anisotropic stratified flow. Each of these regimes dominate flow dynamics over a specific range of scales.

- Power law scaling range for stratified turbulence extends for a greater range of length scales than can be explained by theory for isotropic turbulence.

8.3 Future Work

Stratified turbulence is a complex flow dominated by multiple dynamics. Unlike isotropic homogeneous turbulence, there are not many well-established theories and models for the stratified turbulence, thus so many different aspects of this flow regime

can be investigated using current simulations. The unique advantage of these simulations is the extensive dynamic range. An interesting subject that can be considered as future work is to study the surrogates of energy dissipation rate in stratified turbulence. The identification of the surrogates and their efficiency in predicting energy dissipation rate is essential in geophysical measurements and observations.

Since the flow is dominated by multiple dynamics, modeling of different aspects will be considered separately. One can focus on the modeling of small scale intermittency, which is related to the turbulent patches. Another approach is to model the general shape of the distributions, which reflects large scale anisotropies in the flow. To identify the best surrogates for each approach, it is essential to investigate the contribution of different components of the velocity gradient tensor on the energy dissipation rate over a range of scales as a function of buoyancy Reynolds number.

APPENDIX A

GOVERNING EQUATIONS OF DENSITY STRATIFIED TURBULENCE

The governing equations of the density stratified turbulence, which consists of the conservation of mass (the continuity equation), conservation of momentum (the Navier-Stokes equations), conservation of thermal energy (enthalpy equation), and equation of state, are derived in this section . These equations describe all the related variables in the flow, i.e., longitudinal component of velocity, u, transverse component of velocity, v, vertical component of velocity, w, density, ρ, absolute temperature, T, and pressure, p, completely in three spatial direction, x, y, z, and time ,t.

A.1 Continuity Equation: Conservation of Mass

The full compressible form of conservation of mass is given by [Panton, 1984]:

$$\frac{\partial \rho}{\partial t} + \frac{\partial \rho u_j}{\partial x_j} = 0, \tag{A.1}$$

where $u_i(x_i, t) = (u, v, w)$, represents the instantaneous i^{th} component of velocity at point $x_i = (x, y, z)$ and time t. In terms of material derivative, $D/Dt = \frac{\partial}{\partial t} + u_j \frac{\partial}{\partial x_j}$, the continuity equation can be written as:

$$\frac{D\rho}{Dt} = -\rho \frac{\partial u_j}{\partial x_j}. \tag{A.2}$$

A.2 Navier-Stokes Equations: Conservation of Momentum

The conservation of momentum with rotating frame of reference has the general form of [Panton, 1984]:

$$\frac{\partial(\rho u_i)}{\partial t} + \frac{\partial(\rho u_i u_j)}{\partial x_j} = \frac{\partial T_{ji}}{\partial x_j} + \rho F_i - 2\rho\Omega\epsilon_{ijk}\eta_j u_k, \tag{A.3}$$

where $\Omega\boldsymbol{\eta} = (0, \Omega\cos\phi, \Omega\sin\phi)$ is the angular velocity vector of the Earth's rotation with ϕ as latitude. The term $2\Omega\eta_3 = 2\Omega\sin\phi$ is defined as the Coriolis parameter, which is positive in the northern hemisphere and negative in the southern. T_{ij} is the total stress tensor and represents the surface forces, and F_i represents the body forces. For the stratified turbulence, it is assumed that the only body force is the gravity force and it acts on the vertical direction, x_3 or z. Therefore $F_i = -g\delta_{i3}$. In ordinary pressure and temperature, all the gases and many of the simple liquids obey Newton's viscosity law. Under this assumption, the stress tensor, $T_{ij}(\rho, e, \partial u_l/\partial x_k)$, is a linear function of the local velocity gradients with the coefficients that depend on the local thermodynamic state [see e.g. Panton, 1984]. The stress tensor can be written in terms of thermodynamic pressure, p, and viscous stress tensor, τ_{ij}:

$$T_{ij} = -p\delta_{ij} + \tau_{ij}. \tag{A.4}$$

τ_{ij} is a symmetric tensor and is given by:

$$\tau_{ij} = \lambda\frac{\partial u_k}{\partial x_k}\delta_{ij} + 2\mu S_{ij}, \tag{A.5}$$

where μ and λ are commonly known as the first and second coefficients of viscosity, respectively and S_{ij} is the strain rate tensor:

$$S_{ij} = \frac{1}{2}\left(\frac{\partial u_i}{\partial x_j} + \frac{\partial u_j}{\partial x_i}\right). \tag{A.6}$$

Further simplification is made by assuming Stokes' hypothesis, which states that the thermodynamic and mechanical pressure are equal, consequently $\lambda = -\frac{2}{3}\mu$. Stokes' assumption is reasonably accurate for almost all the Newtonian fluids. The final equation for the total stress tensor assuming constant μ can be written as below:

$$T_{ij} = -p\delta ij - \frac{2}{3}\mu\frac{\partial u_k}{\partial x_k}\delta_{ij} + \mu\left(\frac{\partial u_i}{\partial x_j} + \frac{\partial u_j}{\partial x_i}\right). \tag{A.7}$$

The momentum equation (A.3) under the assumptions described above, are known as the Navier-Stokes equation. By combining the continuity equation, (A.29), and Eq.(A.3), the final Navier-Stokes equation is:

$$\rho\left(\frac{\partial u_i}{\partial t} + u_j\frac{\partial u_i}{\partial x_j}\right) = -\frac{\partial p}{\partial x_i} + \mu\frac{\partial^2 u_i}{\partial x_j^2} + \frac{1}{3}\mu\frac{\partial}{\partial x_i}\left(\frac{\partial u_k}{\partial x_k}\right) - \rho g\delta_{i3} - 2\rho\Omega\epsilon_{ijk}\eta_j u_k. \tag{A.8}$$

A.3 Thermodynamic Equation: Conservation of Enthalpy

The total energy equation that contains both mechanical and thermal energies, is given by [Panton, 1984]:

$$\frac{\partial}{\partial t}[\rho\left(e + \frac{1}{2}u^2\right)] + \frac{\partial}{\partial x_i}[\rho u_i\left(e + \frac{1}{2}u^2\right)] = -\frac{\partial q_i}{\partial x_i} + \frac{\partial}{\partial x_i}(T_{ij}u_j) + \rho u_i F_i, \tag{A.9}$$

where q_i represents the heat flux vector including both radiation and conduction, and e represents the internal energy per unit mass. Assuming Fourier's heat-conduction law, $q_i = -K\partial T/\partial x_i + R_j$, with K as the thermal conductivity and R_j as the radiative heat flux. The thermal-energy equation can be obtained by subtracting the mechanical energy equation

$$\frac{\partial}{\partial t}\left(\rho\frac{1}{2}u^2\right) + \frac{\partial}{\partial x_i}\left(\rho u_i\frac{1}{2}u^2\right) = -u_i\frac{\partial p}{\partial x_i} + u_i\frac{\partial \tau_{ji}}{\partial x_j} + \rho u_i F_i, \tag{A.10}$$

from the total energy equation, Eq.(A.9) as below:

$$\rho\frac{De}{Dt} = \frac{\partial}{\partial t}(\rho e) + \frac{\partial}{\partial x_i}(\rho u_i e) = -p\frac{\partial u_i}{\partial x_i} + \tau_{ji}\frac{\partial u_i}{\partial x_j} - \frac{\partial q_i}{\partial x_i}. \tag{A.11}$$

The thermal-energy equation can be written in terms of temperature using enthalpy $h \equiv e + p/\rho$ and the following thermodynamic relations [e.g. Panton, 1984]:

$$de = dh - \frac{dp}{\rho} + \frac{p}{\rho^2}d\rho, \tag{A.12}$$

$$de = c_v(\rho, T)dT + \frac{1}{\rho^2}\left[p - T\frac{\partial p}{\partial T}|_\rho\right]d\rho, \tag{A.13}$$

and

$$\begin{aligned} dh &= c_p(p,T)dT + \frac{1}{\rho^2}\left[\rho + T\frac{\partial \rho}{\partial T}|_p\right]dp \\ &= c_p(p,T)dT + \frac{1}{\rho}\left[1 - T\beta\right]dp, \end{aligned} \tag{A.14}$$

where c_v and c_p are the specific heat at constant volume and constant pressure, respectively. β is the thermal expansion coefficient, defined as:

$$\beta = -\frac{1}{\rho}\frac{\partial \rho}{\partial T}|_p. \tag{A.15}$$

The equation for the internal energy can be obtained by substituting Eqs.(A.13) and (A.14) in Eq.(A.12) as below:

$$\frac{De}{Dt} = c_p\frac{DT}{Dt} - \frac{T\beta}{\rho}\frac{Dp}{Dt} + \frac{p}{\rho^2}\frac{D\rho}{Dt}. \tag{A.16}$$

By combining the above equation with Eq.(A.11), the thermal energy equation reduces to:

$$\rho c_p\frac{DT}{Dt} = -p\frac{\partial u_i}{\partial x_i} - \frac{\partial q_i}{\partial x_i} + \tau_{ji}\frac{\partial u_i}{\partial x_j} + \beta T\frac{Dp}{Dt} - \frac{p}{\rho}\frac{D\rho}{Dt}. \tag{A.17}$$

This equation can be simplified further by assuming ideal gas law as a general form of state equation, $p = \rho \Re T$. As a result, the bracket terms in Eqs.(A.13) and (A.14) are negligible, e, h, c_v, and c_p are functions of temperature only, and β is:

$$\beta = -\frac{1}{\rho}\frac{\partial \rho}{\partial T}|_p = \frac{1}{T}. \tag{A.18}$$

Therefore,

$$de = c_v dT, \quad dh = c_p dT. \tag{A.19}$$

Dimensional analysis shows that the viscous term is negligible compare to the other terms [Panton, 1984]. The timescales of the radiative flux is usually large compared with the turbulent timescales [Wyngaard, 1992]. Therefore, the effects of radiative flux divergence on the temperature fluctuations can also be neglected. Assuming constant K, the thermal energy equation has the final form of:

$$\rho c_p \frac{DT}{Dt} = K\frac{\partial^2 T}{\partial x_i^2} + \frac{Dp}{Dt}, \tag{A.20}$$

or in terms of c_v,

$$\rho c_v \frac{DT}{Dt} = -p\frac{\partial u_i}{\partial x_i} + K\frac{\partial^2 T}{\partial x_i^2}. \tag{A.21}$$

A.4 Buoyancy Force and Boussinesq Approximation

Further simplification can be made to the Navier-Stokes and energy equations by applying the so-called Boussinesq approximation. This approximation is introduced by J. Boussinesq (1903) and consists of two assumptions: 1) density fluctuations resulting from pressure changes are negligible, 2) density fluctuations resulting from temperature changes are important only as they directly affect buoyancy. There are two conditions under which the Boussinesq approximation is applicable: 1) the

vertical dimension of the fluid is much less than any scale height, 2) the motion-induced fluctuations in density, pressure, and temperature do not exceed (in order of magnitude) the total static variation of these quantities.

Density, pressure, and temperature are coupled quantities and can be divided into three components: the fluctuation due to the motion, variation in the absence of motion, and the space average or the reference value [see e.g. Spiegel and Veronis, 1960]. Thus, the equation for quantity f can be written as below:

$$f(x, y, z, t) = f_m + f_0(z) + f'(x, y, z, t). \tag{A.22}$$

where f_m, is the constant reference value, f_0 is the variation due to the height, and f' is the fluctuations due to the fluid motion. In stratified turbulence $f_0(z)$ is a linear function of elevation and is not affected by the motion. The first assumption of Boussinesq approximation implies that the maximum change of the quantity f due to the height is much smaller than the reference value:

$$\frac{\Delta f_0}{f_m} \sim \varepsilon \ll 1. \tag{A.23}$$

Under Boussinesq approximation the thickness or maximum height of the flow d is much smaller than the scale height D_f:

$$D_f = |\frac{1}{f_m}\frac{df_0}{dz}|^{-1}. \tag{A.24}$$

The second assumption can be written as:

$$|\frac{f'}{f_m}| \sim \varepsilon. \tag{A.25}$$

Starting with the ideal gas law and applying assumptions above, we can derive the linearized perturbation ideal gas law as below [see e.g. Garratt, 1994, Stull, 1988]:

$$\frac{p - p_m}{p_m} = \frac{\rho - \rho_m}{\rho_m} + \frac{T - T_m}{T_m}. \tag{A.26}$$

Consequently,

$$\frac{\rho_0}{\rho_m} = \frac{p_0}{p_m} - \frac{T_0}{T_m}, \tag{A.27}$$

and,

$$\frac{\rho'}{\rho_m} = \frac{p'}{p_m} - \frac{T'}{T_m}. \tag{A.28}$$

By applying these assumptions and the order of magnitude comparison in the conservation of mass and momentum equations , the equations reduce to:

$$\frac{\partial u_j}{\partial x_j} = 0, \tag{A.29}$$

and

$$\frac{\partial u_i}{\partial t} + u_j \frac{\partial u_i}{\partial x_j} = -\frac{1}{\rho_m}\frac{\partial p}{\partial x_i} + \nu \frac{\partial^2 u_i}{\partial x_j^2} - \frac{\rho}{\rho_m} g \delta_{i3} - 2\Omega \epsilon_{ijk} \eta_j u_k, \tag{A.30}$$

with $\nu = \mu/\rho$ as the kinematic viscosity. The momentum equation can be simplified further more. Consider the vertical component of this equation in the absence of motion:

$$\frac{\partial p_0}{\partial z} = -g\left(\rho_m + \rho_0(z)\right). \tag{A.31}$$

Substituting Eq.(A.31) in Eq.(A.30) and neglecting the rotational effects, the equation can be written as below:

$$\frac{\partial w}{\partial t} + u_j \frac{\partial w}{\partial x_j} = -\frac{1}{\rho_m}\frac{\partial p'}{\partial z} - g\frac{\rho'}{\rho_m} + \nu \frac{\partial^2 u_i}{\partial x_j^2}. \tag{A.32}$$

The motion is driven by fluctuations, thus the term ρ'/ρ_m can not be neglected although it is in the order of ε. substituting ρ' by Eq.(A.28) results in:

$$-\frac{1}{\rho_m}\frac{\partial p'}{\partial z} - g\frac{\rho'}{\rho_m} = -\frac{1}{\rho_m}\frac{\partial p'}{\partial z} + g\frac{p'}{p_m} - g\frac{T'}{T_m} \tag{A.33}$$

$$= -\frac{1}{\rho_m}\left(\frac{\partial p'}{\partial z} - \frac{p'}{H}\right) + g\frac{T'}{T_m}, \tag{A.34}$$

where $H = p_m/g\rho_m$, is the thickness of the flow with uniform density in which pressure varies from p_m at the bottom to zero at the top. Thus $d < D_p < H$, $p'/H < p'/d < \partial p'/\partial z$, and the term p'/H is negligible compared with $\partial p'/\partial z$. Therefore, (to the order of $O(d/H)$ $\rho'/\rho_m = T'/T_m$) the density fluctuations are replaced by the temperature fluctuations only and the momentum equation is reduced to:

$$\frac{\partial u_i}{\partial t} + u_j\frac{\partial u_i}{\partial x_j} = -\frac{1}{\rho_m}\frac{\partial p'}{\partial x_i} + \nu\frac{\partial^2 u_i}{\partial x_j^2} + \frac{T'}{T_m}g\delta_{i3} - 2\Omega\epsilon_{ijk}\eta_j u_k. \tag{A.35}$$

To simplify the energy equation

$$\rho c_v\frac{DT}{Dt} = -p\frac{\partial u_i}{\partial x_i} + K\frac{\partial^2 T}{\partial x_i^2}, \tag{A.36}$$

further consideration is required. The term $p\partial u_i/\partial x_i$ can not be neglected since it has the same order of magnitude as the other terms in the equation. We can simplify this term by recalling Eq.(A.29) and Eq.(A.26) and neglecting the terms in the order of (d/H) and smaller:

$$-p\frac{\partial u_i}{\partial x_i} = \frac{p}{\rho}\frac{D\rho}{Dt}$$

$$= p_m\frac{D}{Dt}\left(\frac{T_0 + T'}{T_m} - \frac{p_0}{p_m}\right)$$

$$= \frac{p_m}{T_m}\frac{D}{Dt}(T_0 + T') + \rho_m g u_i\delta_{i3}. \tag{A.37}$$

Finally by substituting Eq.(A.37) in Eq.(A.36), the energy equation under Boussinessq assumption reduces to:

$$\rho_m c_p \frac{DT}{Dt} = -\rho_m g u_i \delta_{i3} + K \frac{\partial^2 T}{\partial x_i^2}, \tag{A.38}$$

The final set of governing equations after applying all the simplifications described above, *i.e.*, constant dynamic viscosity and molecular diffusivity, Newtonian fluid and Stokes hypothesis, Boussinesq approximation, and negligible viscous stress heat generation and radiative heat transfer compared with other heat sources in thermodynamic equations, can be summarized as:

$$\rho = \rho_m[1 - \beta(T - T_m)], \tag{A.39a}$$

$$\frac{\partial u_i}{\partial x_i} = 0, \tag{A.39b}$$

$$\frac{\partial u_i}{\partial t} + u_j \frac{\partial u_i}{\partial x_j} = -\frac{1}{\rho_m}\frac{\partial p}{\partial x_i} + \nu \frac{\partial^2 u_i}{\partial x_j^2} - \frac{\rho}{\rho_m} g \delta_{i3} - 2\Omega \epsilon_{ijk} \eta_j u_k, \tag{A.39c}$$

$$c_p \left(\frac{\partial T}{\partial t} + u_j \frac{\partial T}{\partial x_j} \right) = \frac{K}{\rho_m} \frac{\partial^2 T}{\partial x_i^2} - g u_i \delta_{i3}. \tag{A.39d}$$

APPENDIX B

CALCULATING LOCALLY AVERAGED VALUES

Equations (5.2) and (5.3) are, to our knowledge attributable to Sykora [2007] and published only online. The derivations are provided here for reference. Consider scalar ξ with mean $\bar{\xi}$ and fluctuating ξ' terms. The local volume average of ξ on a volume of linear dimension r is defined as:

$$\begin{aligned} \xi_r(\boldsymbol{x}) &\equiv \bar{\xi} + \xi'_r(\boldsymbol{x}) \\ &= \bar{\xi} + \frac{1}{V_r}\int_{V_r} \xi'(\boldsymbol{x}+\boldsymbol{x'})\, d\boldsymbol{x'}. \end{aligned} \tag{B.1}$$

Introducing the operators $\mathcal{F}$ and $\mathcal{F}^{-1}$ as the forward and backward Fourier transforms, and $\hat{\xi}'(\boldsymbol{\kappa})$ and $\hat{\xi}'_r(\boldsymbol{\kappa})$ as the Fourier transform of $\xi'(\boldsymbol{x})$ and $\xi'_r(\boldsymbol{x})$:

$$\begin{aligned} \hat{\xi}'_r(\boldsymbol{\kappa}) &\equiv \mathcal{F}\{\xi'_r(\boldsymbol{x})\} \\ &= \iiint_{-\infty}^{\infty} \xi'_r(x) e^{-i\boldsymbol{\kappa}\cdot\boldsymbol{x}}\, d\boldsymbol{x}. \end{aligned} \tag{B.2}$$

The Fourier coefficients of ξ'_r can be written as:

$$\hat{\xi}'_r(\boldsymbol{\kappa}) = \frac{1}{V_r}\iiint_{-\infty}^{\infty} e^{-i\boldsymbol{\kappa}\cdot\boldsymbol{x}} \left[\int_{V_r} \xi'(\boldsymbol{x}+\boldsymbol{x'})\, d\boldsymbol{x'}\right] d\boldsymbol{x}. \tag{B.3}$$

The above equation can be simplified by changing the order of the integrals and introducing the new variable $\boldsymbol{v} = \boldsymbol{x} + \boldsymbol{x'}$, as below:

$$\hat{\xi}'_r(\boldsymbol{\kappa}) = \frac{1}{V_r}\int_{V_r} e^{i\boldsymbol{\kappa}\cdot\boldsymbol{x'}} \left(\iiint_{-\infty}^{\infty} e^{-i\boldsymbol{\kappa}\cdot\boldsymbol{v}} \xi'(\boldsymbol{v})\, d\boldsymbol{v}\right) d\boldsymbol{x'}. \tag{B.4}$$

The inner integral is the Fourier transform of $\xi'(\boldsymbol{x})$. Hence, Eq.(B.4) can be written as:

$$\hat{\xi'}_r(\boldsymbol{\kappa}) = \frac{\hat{\xi'}(\boldsymbol{\kappa})}{V_r} \int_{V_r} e^{i\boldsymbol{\kappa}\cdot\boldsymbol{x'}}\, d\boldsymbol{x'} \tag{B.5}$$

This integral can be interpreted as the wave number space images of n-dimensional spheres. Sykora [2007] discusses the solution as the nth-order sinc function. Here we derive the results for the one- and three-dimensional cases. In one-dimension, integration is over a line with length h. With $h' \equiv h/2$ and κ_i the wave number in the direction of the averaging,

$$\frac{1}{2h'} \int_{-h'}^{h'} e^{i\kappa_i x}\, dx = \frac{\sin(\kappa_i h')}{\kappa_i h'}. \tag{B.6}$$

The local average of ξ' is the inverse Fourier transform of $\hat{\xi'}_h(\kappa_i)$,

$$\begin{aligned} \xi'_h(x) &= \mathcal{F}^{-1}\left\{\hat{\xi'}(\kappa)\frac{\sin(\kappa_i h/2)}{\kappa_i h/2}\right\} \\ &= \int_{-\infty}^{\infty} e^{i\kappa_i x}\hat{\xi'}(\kappa_i)\frac{\sin(\kappa_i h/2)}{\kappa_i h/2}\, d\kappa_i, \end{aligned} \tag{B.7}$$

and the one-dimensional local average is obtained by substituting Eq.(B.7) back into Eq.(B.1),

$$\xi_h(x) = \bar{\xi} + \int_{-\infty}^{\infty} e^{i\kappa_i x}\hat{\xi'}(\kappa_i)\frac{\sin(\kappa_i h/2)}{\kappa_i h/2}\, d\kappa_i. \tag{B.8}$$

To derive the spherical average, it is observed that the integral in Eq.(B.5) does not depend upon the choice of the coordinate system and so we rewrite the equation in spherical coordinates using the notation $\boldsymbol{x} = (r, \theta, \phi)$ and $\boldsymbol{\kappa} = (\rho, \psi, \chi)$ with

$$x = r\cos(\theta)\sin(\phi),$$

$$y = r\sin(\theta)\sin(\phi),$$

$$z = r\cos(\phi),$$

and,

$$\kappa_x = \rho\cos(\psi)\sin(\chi),$$

$$\kappa_y = \rho\sin(\psi)\sin(\chi),$$

$$\kappa_z = \rho\cos(\chi).$$

In spherical coordinate system, Eq.(B.5) can be written as:

$$\begin{aligned}\int_{V_r} e^{i(xk_x+yk_y+zk_z)}\,dx\,dy\,dz &= \int_{V_r} e^{ir\rho\cos(\psi)\sin(\chi)\cos(\theta)\sin(\phi)}r^2\sin(\phi)\,dr\,d\phi\,d\theta \\ &+ \int_{V_r} e^{ir\rho\sin(\psi)\sin(\chi)\sin(\theta)\sin(\phi)}r^2\sin(\phi)\,dr\,d\phi\,d\theta \\ &+ \int_{V_r} e^{ir\rho\cos(\chi)\cos(\phi)}r^2\sin(\phi)\,dr\,d\phi\,d\theta. \qquad \text{(B.9)}\end{aligned}$$

Upon applying trigonometric simplifications, the integral becomes

$$\frac{1}{V_r}\int_{V_r}\exp\left[ir\rho\left(\cos(\psi-\theta)\sin(\chi)\sin(\phi)+\cos(\chi)\cos(\phi)\right)\right]r^2\sin(\phi)\,dr\,d\phi\,d\theta. \quad \text{(B.10)}$$

Noting that the orientation of the coordinate system is arbitrary, we rotate it so that $\chi = 0$:

$$\frac{1}{V_r}\int_0^{\pi}\int_0^{2\pi}\int_0^{r'} e^{ir\rho\cos(\phi)}r^2\sin(\phi)\,dr\,d\phi\,d\theta = \frac{2\pi}{V_r}\int_0^{r'}\left(\int_0^{\pi} e^{ir\rho\cos(\phi)}\sin(\phi)\,d\phi\right)r^2\,dr, \qquad \text{(B.11)}$$

The inner integral can be solved by changing the variables:

$$\begin{aligned}\int_0^{\pi} e^{ir\rho\cos(\phi)}\sin(\phi)\,d\phi &= \int_{-1}^{1} e^{ir\rho u}\,du \\ &= 2\frac{\sin(r\rho)}{r\rho}, \qquad \text{(B.12)}\end{aligned}$$

an the final integral further reduces to:

$$\frac{4\pi}{V_r}\int_0^{r'} r^2\frac{\sin(r\rho)}{r\rho}\,dr. \qquad \text{(B.13)}$$

The integral is solved using integration by parts. Aligning the Cartesian coordinate system so that $\kappa = \rho$ and noting that the volume of a sphere with linear size of r is $V_r = 4\pi r'^3/3$, then Eq.(B.13) simplifies to

$$\frac{4\pi}{V_r}\left(\frac{\sin(\kappa r')}{\kappa^3} - r'\frac{\cos(\kappa r')}{\kappa^2}\right) = 3\frac{\sin(\kappa r')}{\kappa^3 r'^3} - 3\frac{\cos(\kappa r')}{\kappa^2 r'^2}. \tag{B.14}$$

Finally, $\xi_r(\boldsymbol{x})$ is obtained by substituting Eq.(B.14) back into Eq.(B.5), inverse Fourier transforming, and substituting $r' \equiv r/2$:

$$\xi'_r(\boldsymbol{x}) = 3\iiint_{-\infty}^{\infty} e^{i\boldsymbol{\kappa}\cdot\boldsymbol{x}}\hat{\xi}'(\boldsymbol{\kappa})\left(\frac{\sin(\kappa r/2)}{\kappa^3(r/2)^3} - \frac{\cos(\kappa r/2)}{\kappa^2(r/2)^2}\right) d\boldsymbol{\kappa}. \tag{B.15}$$

The three-dimensional local average is obtained by substituting Eq.(B.15) back into Eq.(B.1),

$$\xi_r(\boldsymbol{x}) = \bar{\xi} + 3\iiint_{-\infty}^{\infty} e^{i\boldsymbol{\kappa}\cdot\boldsymbol{x}}\hat{\xi}'(\boldsymbol{\kappa})\left(\frac{\sin(\kappa r/2)}{\kappa^3(r/2)^3} - \frac{\cos(\kappa r/2)}{\kappa^2(r/2)^2}\right) d\boldsymbol{\kappa}. \tag{B.16}$$

BIBLIOGRAPHY

S. Almalkie and S. M. de Bruyn Kops. Kinetic energy dynamics in forced, horizontally homogeneous and isotropic, stably stratified turbulence. *J. Turbulence*, submitted.

F. Anselmet, Y. Gagne, E. J. Hopfinger, and R. A. Antonia. High-order velocity structure functions in turbulent shear flows. *J. Fluid Mech.*, 140:63–89, 1984.

R. A. Antonia, A. J. Chambers, and B. R. Satyaprakash. Reynolds number dependence of high order moments of the streamwise turbulent velocity derivative. *Bound.-Lay. Meteorol.*, 21:159–171, 1981.

R. A. Antonia, B. R. Satyaprakash, and A. K. M. F. Hussain. Statistics of fine-scale velocity in turbulent plane and circular jets. *J. Fluid Mech.*, 119:55–89, 1982.

E. Arobone and S. Sarkar. The statistical evolution of a stratified mixing layer with horizontal shear invoking feature extraction. *Phys. Fluids*, 22(11), 2010.

S. Basak and S. Sarkar. Dynamics of a stratified shear layer with horizontal shear. *J. Fluid Mech.*, 568:19–54, 2006.

S. Basu, E. Foufoula-Georgiou, B. Lashermes, and A. Arnéodo. Estimating intermittency exponent in neutrally stratified atmospheric surface layer flows: A robust framework based on magnitude cumulant and surrogate analyses. *Phys. Fluids*, 19 (11):115102, 2007.

G. K. Batchelor and A. A. Townsend. The nature of turbulent motion at large wavenumbers. *P. Roy. Soc. Lond. A. Mat.*, 199:238–255, 1949.

M. Beckers, R. Verzicco, H. J. H. Clercx, and G. J. F. van Heijst. Dynamics of pancake-like vortices in a stratified fluid: experiments, model and numerical simulations. *J. Fluid Mech.*, 433:1–27, 2001.

M. Beckers, H. J. H. Clerx, G. J. F. van Heijst, and R. Verzicco. Dipole formation by two interacting shielded monopoles in a stratified fluid. *Phys. Fluids*, 14:704, 2002.

R. Benzi, L. Biferale, G. Paladin, A. Vulpiani, and M. Vergassola. Multifractality in the statistics of the velocity-gradients in turbulence. *Phys. Rev. Lett.*, 67(17): 2299–2302, 1991.

R. Benzi, S. Ciliberto, R. Tripiccione, C. Baudet, F. Massaioli, and S. Succi. Extended self-similarity in turbulent flows. *Phys. Rev. E*, 48(1):R29–R32, 1993.

R. Benzi, L. Biferale, R. Fisher, D. Q. Lamb, and F. Toschi. Inertial range Eulerian and Lagrangian statistics from numerical simulations of isotropic turbulence. *J. Fluid Mech.*, 653:221–244, 2010.

J. Berg, S. Ott, J. Mann, and B. Luthi. Experimental investigation of Lagrangian structure functions in turbulence. *Phys. Rev. E*, 80(2, Part 2), 2009.

A. Bershadskii and A. Tsinober. Local anisotropic effects on multifractality of turbulence. *Phys. Rev. E*, 48(1):282–287, 1993.

A. Bershadskii, E. Kit, and A. Tsinober. On universality of geometrical invariants in turbulence - Experimental results. *Phys. Fluids*, 5(7):1523–1525, 1993.

L. Biferale. A note on the fluctuation of dissipative scale in turbulence. *Phys. Fluids*, 20(3):031703, 2008. doi: 10.1063/1.2898658.

L. Biferale and I. Procaccia. Anisotropy in turbulent flows and in turbulent transport. *Phys. Rep.*, 414(2-3):43–164, 2005.

L. Biferale and M. Vergassola. Isotropy vs anisotropy in small-scale turbulence. *Phys. Fluids*, 13(8):2139–2141, 2001.

L. Biferale, I. Daumont, A. Lanotte, and F. Toschi. Anomalous and dimensional scaling in anisotropic turbulence. *Phys. Rev. E*, 66(5), 2002.

L. Biferale, I. Daumont, A. Lanotte, and F. Toschi. Theoretical and numerical study of highly anisotropic turbulent flows. *Eur. J. Mech. B.-Fluid*, 23(3):401–414, 2004.

L. Biferale, E. Bodenschatz, M. Cencini, A. S. Lanotte, N. T. Ouellette, F. Toschi, and H. Xu. Lagrangian structure functions in turbulence: A quantitative comparison between experiment and direct numerical simulation. *Phys. Fluids*, 20(6), 2008a.

L. Biferale, A. S. Lanotte, and F. Toschi. Statistical behaviour of isotropic and anisotropic fluctuations in homogeneous turbulence. *Physica D*, 237(14-17):1969–1975, 2008b.

P. Billant and J.-M. Chomaz. Three-dimensional stability of a vertical columnar vortex pair in a stratified fluid. *J. Fluid Mech.*, 419:65–91, 2000a.

P. Billant and J.-M. Chomaz. Experimental evidence for a new instability of a vertical columnar vortex pair in a strongly stratified fluid. *J. Fluid Mech.*, 418:167–188, 2000b.

P. Billant and J.-M. Chomaz. Self-similarity of strongly stratified inviscid flows. *Phys. Fluids*, 13:1645–1651, 2001.

P. Billant, A. Deloncle, J. M. Chomaz, and P. Otheguy. Zigzag instability of vortex pairs in stratified and rotating fluids. part 2. analytical and numerical analyses. *J. Fluid Mech.*, 660:396–429, 2010.

F. Boettcher, C. Renner, H. P. Waldl, and J. Peinke. On the statistics of wind gusts. *Bound.-Lay. Meteorol.*, 108:163–173, 2003.

M. Bonnier and O. Eiff. Experimental investigation of the collapse of a turbulent wake in a stably stratified fluid. *Phys. Fluids*, 14:791, 2002.

M. Bonnier, O. Eiff, and P. Bonneton. On the density structure of far-wake vortices in a stratified fluid. *Dynamics Of Atmospheres And Oceans*, 31:117–137, 2000.

O. N. Boratav and R. B. Pelz. Structures and structure functions in the inertial range of turbulence. *Phys. Fluids*, 9(5):1400–1415, 1997.

W. J. T. Bos, L. Liechtenstein, and K. Schneider. Small-scale intermittency in anisotropic turbulence. *Phys. Rev. E*, 76(4, Part 2), 2007.

J. Boussinesq. *Théorie analytique de la chaleur*, volume 2, p. 172. Gauthier-Villars, Paris, 1903.

M. E. Brachet. Direct simulation of three-dimensional turbulence in the Taylor-Green vortex. *Fluid Dyn. Res.*, 8:1–8, 1991.

M. E. Brachet, D. I. Meiron, S. A. Orszag, B. G. Nickel, R. H. Morf, and U. Frisch. Small-scale structure of the Taylor-Green vortex. *J. Fluid Mech.*, 130:411–452, 1983.

G. Brethouwer and E. Lindborg. Numerical study of vertical dispersion by stratified turbulence. *J. Fluid Mech.*, 631:149–163, 2009.

K. A. Brucker and S. Sarkar. Evolution of an initially turbulent stratified shear layer. *Phys. Fluids*, 19(10), 2007.

K. A. Brucker and S. Sarkar. A comparative study of self-propelled and towed wakes in a stratified fluid. *J. Fluid Mech.*, 652:373–404, 2010.

G. F. Carnevale, M. Briscolini, and M. Orlandi. Buoyancy-to-inertial-range transition in forced stratified turbulence. *J. Fluid Mech.*, 427:205–239, 2001.

C. M. Casciola, P. Gualtieri, B. Jacob, and R. Piva. The residual anisotropy at small scales in high shear turbulence. *Phys. Fluids*, 19(10), 2007.

A. J. Chambers and R. A. Antonia. Atmospheric estimates of power-law exponents μ and μ_θ. *Bound.-Lay. Meteorol.*, 28:343–52, 1984.

S. Chen, G. D. Doolen, R. H. Kraichnan, and Z. She. On statistical correlation between velocity increments and locally averaged dissipation in homogeneous turbulence. *Phys. Fluids A*, 5(2):458–463, 1993.

S. Chen, K. R. Sreenivasan, M. Nelkin, and N. Z. Cao. Refined similarity hypothesis for transverse structure functions in fluid turbulence. *Phys. Rev. Lett.*, 79(12): 2253–2256, 1997a.

S. Y. Chen, G. D. Doolen, R. H. Kraichnan, and L. P. Wang. Is the Kolmogorov refined similarity relation dynamic or kinematic? *Phys. Rev. Lett.*, 74(10):1755–1758, 1995.

S. Y. Chen, K. R. Sreenivasan, and M. Nelkin. Inertial range scalings of dissipation and enstrophy in isotropic turbulence. *Phys. Rev. Lett.*, 79(7):1253–1256, 1997b.

J. Cleve, M. Greiner, and K. R. Sreenivasan. On the effects of surrogacy of energy dissipation in determining the intermittency exponent in fully developed turbulence. *Europhys. Lett*, 61:756, 2003.

J. Cleve, M. Greiner, B. R. Pearson, and K. R. Sreenivasan. Intermittency exponent of the turbulent energy cascade. *Phys. Rev. E*, 69:066316, 2004.

S. M. de Bruyn Kops and J. J. Riley. Direct numerical simulation of laboratory experiments in isotropic turbulence. *Phys. Fluids*, 10(9):2125–2127, 1998.

Matthew B. de Stadler, Sutanu Sarkar, and Kyle A. Brucker. Effect of the prandtl number on a stratified turbulent wake. *Phys. Fluids*, 22(9), SEP 2010.

A. Deloncle, P. Billant, and J.-M. Chomaz. Nonlinear evolution of the zigzag instability in stratified fluids: a shortcut on the route to dissipation. *J. Fluid Mech.*, 599:229–239, 2008.

A. Deloncle, P. Billant, and J.-M. Chomaz. Three-dimensional stability of vortex arrays in a stratified and rotating fluid. *J. Fluid Mech.*, 678:482–510, 2011.

E. M. Dewan. Stratospheric wave spectra resembling turbulence. *Science*, 204(4395): 832–835, 1979.

E. M. Dewan and R. E. Good. Saturation and the universal spectrum for vertical profiles of horizontal scalar winds in the atmosphere. *J. Geophys. Res.-Atmos.*, 91: 2742–2748, 1986.

B. Dhruva, Y. Tsuji, and K. R. Sreenivasan. Transverse structure functions in high-Reynolds-number turbulence. *Phys. Rev. E*, 56(5, Part a):R4928–R4930, 1997.

P. J. Diamessis, G. R. Spedding, and J. A. Domaradzki. Similarity scaling and vorticity structure in high-reynolds-number stably stratified turbulent wakes. *J. Fluid Mech.*, 671:52–95, 2011.

W. Dobler, N. E. L. Haugen, T. A. Yousef, and A. Brandenburg. Bottleneck effect in three-dimensional turbulence simulations. *Phys. Rev. E*, 68(2):026304, 2003.

D. A. Donzis and K. R. Sreenivasan. The bottleneck effect and the Kolmogorov constant in isotropic turbulence. *J. Fluid Mech.*, 657:171–188, 2010.

D. A. Donzis, P. K. Yeung, and K. R. Sreenivasan. Dissipation and enstrophy in isotropic turbulence: Resolution effects and scaling in direct numerical simulations. *Phys. Fluids*, 20(4):045108, 2008.

S. Douady, Y. Couder, and M. E. Brachet. Direct observation of the intermittency of intense vorticity filaments in turbulence. *Phys. Rev. Lett.*, 67(8):983–986, 1991.

V. Eswaran and S. B. Pope. Direct numerical simulations of the turbulent mixing of a passive scalar. *Phys. Fluids*, 31:506–520, 1988.

A. M. Fincham, T. Maxworthy, and G. R. Spedding. Energy dissipation and vortex structure in freely decaying, stratified grid turbulence. *Dyn. Atmos. Oceans*, 23: 155–169, 1996.

J. B. Flór and G. J. F. van Heijst. Experimental study of dipolar vortex structures in a stratified fluid. *J. Fluid Mech.*, 279:101, 1994.

R. Frehlich, Y. Meillier, M. L. Jensen, and B. Balsley. A statistical description of small-scale turbulence in the low-level nocturnal jet. *J. Atmos. Sci.*, 61(9):1079–1085, 2004.

U. Frisch. *Turbulence: The Legacy of A. N. Kolmogorov*. Cambridge University Press, 1995.

U. Frisch and R. Morf. Intermittency in nonlinear dynamics and singularities at complex times. *Phys. Rev. A*, 23(5):2673–2705, 1981.

U. Frisch, P. L. Sulem, and M. Nelkin. A simple dynamical model of intermittent fully developed turbulence. *J. Fluid Mech.*, 87:719–736, 1987.

A. Gargett, T. Osborn, and P. Nasmyth. Local isotropy and the decay of turbulence in a stratified fluid. *J. Fluid Mech.*, 144:231, 1984.

J. R. Garratt. *The Atmospheric Boundary Layer*. Cambridge University Press, 1994.

C. H. Gibson. Fossil turbulence, salinity, and vorticity turbulence in the ocean. In J. C.J. Nihous, editor, *Marine Turbulence*, pages 221–257. Elsevier, 1980.

C. H. Gibson, G. R. Stegen, and S. McConnell. Measurements of the universal constant in Kolmogorov's third hypothesis for high Reynolds number turbulence. *Phys. Fluids*, 13:2448–2451, 1970.

R. Godoy-Diana and J.-M. Chomaz. Effect of the Schmidt number on the diffusion of axisymmetric pancake vortices in a stratified fluid. *Phys. Fluids*, 15:1058–1064, 2003.

R. Godoy-Diana, J.-M. Chomaz, and P. Billant. Vertical length scale selection for pancake vorticies in strongly stratified viscous fluids. *J. Fluid Mech.*, 504:229–238, 2004.

T. Gotoh, D. Fukayama, and T. Nakano. Velocity field statistics in homogeneous steady turbulence obtained using a high-resolution direct numerical simulation. *Phys. Fluids*, 14(3):1065–1081, 2002.

M. C. Gregg. Diapycnal mixing in the thermocline – a review. *J. Geophys. Res.–Oceans*, 92:5249–5286, 1987.

S. Grossmann, D. Lohse, and A. Reeh. Different intermittency for longitudinal and transversal turbulent fluctuations. *Phys. Fluids*, 9(12):3817–3825, 1997.

G. Gulitski, M. Kholmyansky, W. Kinzelbach, B. Lüthi, A. Tsinober, and S. Yorish. Velocity and temperature derivatives in high-Reynolds-number turbulent flows in the atmospheric surface layer. Part 2. Accelerations and related matters. *J. Fluid Mech.*, 589:83–102, 2007a.

G. Gulitski, M. Kholmyansky, W. Kinzelbach, B. Lüthi, A. Tsinober, and S. Yorish. Velocity and temperature derivatives in high-Reynolds-number turbulent flows in the atmospheric surface layer. Part 3. Temperature and joint statistics of temperature and velocity derivatives. *J. Fluid Mech.*, 589:103–123, 2007b.

P. E. Hamlington, D. Krasnov, T. Boeck, and J. Schumacher. Statistics of the energy dissipation rate and local enstrophy in turbulent channel flow. *Physica D*, 241: 169–177, 2012.

Z. Hao, T. Zhou, Y. Zhou, and J. Mi. Reynolds number dependence of the inertial range scaling of energy dissipation rate and enstrophy in a cylinder wake. *Exp. Fluids*, 44(2):279–289, 2008.

D. A. Hebert and S. M. de Bruyn Kops. Predicting turbulence in flows with strong stable stratification. *Phys. Fluids*, 18(6):1–10, 2006.

J. A. Herring. Approach of axisymmetric turbulence to isotropy. *Phys. Fluids*, 17: 859–872, 1974.

J. R. Herring and O. Métais. Numerical experiments in forced stably stratified turbulence. *J. Fluid Mech.*, 202:97, 1989.

Jackson R. Herring and Yoshifumi Kimura. Structure formation in stratified turbulence. In Y Kaneda, editor, *IUTAM symposium on computational physics and new perspectives in turbulence*, volume 4 of *IUTAM Bookseries*, pages 355–360, 2008. IUTAM Symposium on Computational Physics and New Perspectives in Turbulence, Nagoya Univ, Nagoya, JAPAN, SEP 11, 2006-SEP 14, 2009.

J. Hierro and C. Dopazo. Fourth-order statistical moments of the velocity gradient tensor in homogeneous, isotropic turbulence. *Phys. Fluids*, 15(11):3434–3442, 2003.

J. O. Hinze. *Turbulence*. McGraw-Hill, New York, 2nd edition, 1975.

M. Holzer and E. D. Siggia. Turbulent mixing of a passive scalar. *Phys. Fluids*, 6: 1820–1837, 1994.

I. Hosokawa. A paradox of the 1D surrogate of dissipation rate in isotropic turbulence. *J. Phys. Soc. Jpn*, 64(9):3141–3144, 1995.

I. Hosokawa, S. Oide, and K. Yamamoto. Isotropic turbulence: Important differences between true dissipation rate and its one-dimensional surrogate. *Phys. Rev. Lett.*, 77(22):4548–4551, 1996.

Jörg Imberger and Boualem Boashash. Application of the Winger-Ville distribution to temperature gradient microstructure: A new technique to study small-scale variations. *J. Phys. Oceanogr.*, 16:1997–2012, 1986.

T. Ishihara, Y. Kaneda, M. Yokokawa, K. Itakura, and A. Uno. Small-scale statistics in high-resolution direct numerical simulation of turbulence: Reynolds number dependence of one-point velocity gradient statistics. *J. Fluid Mech.*, 592:335–366, 2007.

T. Ishihara, T. Gotoh, and Y. Kaneda. Study of high-Reynolds number isotropic turbulence by direct numerical simulation. *Annu. Rev. Fluid Mech.*, 41:165–180, 2009.

F. G. Jacobitz, S. Sarkar, and C. W. VanAtta. Direct numerical simulations of the turbulence evolution in a uniformly sheared and stably stratified flow. *J. Fluid Mech.*, 342:231–261, 1997.

Y. Jang and S. M. de Bruyn Kops. Pseudo-spectral numerical simulation of miscible fluids with a high density ratio. *Comput. Fluids*, 36:238–247, 2007.

Javier Jiménez, Alan A. Wray, Philip G. Saffman, and Robert S. Rogallo. The structure of intense vorticity in isotropic turbulence. *J. Fluid Mech.*, 255:65–90, 1993.

Y. Kaneda and K. Yoshida. Small-scale anisotropy in stably stratified turbulence. *New J. Phys.*, 6, 2004.

Y. Kitamura and Y. Matsuda. The k_h^{-3} and $k_h^{-5/3}$ energy spectra in stratified turbulence. *Geophys. Res. Let.*, 33(5):L05809, 2006. doi: 10.1029/2005GL024996.

J. C. Klewicki, M. M. Metzger, J. F. Foss, D. G. Bohl, J. M. Wallance, L. Ong, and A. Folz. High Reynolds number boundary layer turbulence in the atmospheric surface layer above Western Utah's salt flats. In R. J. Donnelly and K. R. Sreenivasan, editors, *Flow at Ultra-High Reynolds and Rayleigh Numbers*, page 450. Springer, Berlin Heidelberg: Springer-Verlag, 1998.

A. N. Kolmogorov. Local structure of turbulence in an incompressible fluid at very high Reynolds numbers. *Dokl. Akad. Nauk SSSR*, 30:299–303, 1941.

A. N. Kolmogorov. A refinement of previous hypotheses concerning the local structure of turbulence in a viscous incompressible fluid at high Reynolds number. *J. Fluid Mech.*, 13:82–85, 1962.

R. H. Kraichnan. Intermittency in the very small scales of turbulence. *Phys. Fluids*, 10:2080–2082, 1967.

R. H. Kraichnan. On Kolmogorov's inertial-range theories. *J. Fluid Mech.*, 62:305–330, 1974.

A. Y. Kuo and S. Corrsin. Experiments on internal intermittency and fine-structure distribution function in fully turbulent fluid. *J. Fluid Mech.*, 50:285–320, 1971.

S. Kurien, V. S. L'vov, I. Procaccia, and K. R. Sreenivasan. Scaling structure of the velocity statistics in atmospheric boundary layers. *Phys. Rev. E*, 61:407–421, 2000.

D. K. Lilly. Stratified turbulence and the mesoscale variability of the atmosphere. *J. Atmos. Sci.*, 40:749–761, 1983.

J.-T. Lin and Y.-H. Pao. Wakes in stratified fluids: a review. *Annu. Rev. Fluid Mech.*, 11:317, 1979.

E. Lindborg. The effect of rotation on the mesoscale energy cascade in the free atmosphere. *Geophys. Res. Let.*, 32:L01809, 2005.

E. Lindborg. The energy cascade in a strongly stratified fluid. *J. Fluid Mech.*, 550: 207–242, 2006.

D. Lohse and A. Mullergroeling. Bottleneck effects in turbulence - scaling phenomena in R-space versus P-space. *Phys. Rev. Lett.*, 74(10):1747–1750, 1995.

J. L. Lumley. The spectrum of nearly inertial turbulence in a stably stratified fluid. *J. Atmos. Sci.*, 21(99-102), 1964.

J. L. Lumley and H. A. Panofsky. *The Structure of Atmospheric Turbulence*. Interscience Publishers, New York, 1964.

L. Mahrt. Intermittency of atmospheric turbulence. *J. Atmos. Sci.*, 46(1):79–95, 1989.

B. B. Mandelbrot. Intermittent turbulence in self-similar cascades - divergence of high moments and dimension of carrier. *J. Fluid Mech.*, 62:331–358, 1974.

C. Meneveau and T. Poinsot. Stretching and quenching of flamelets in premixed turbulent combustion. *Combust. Flame*, 86:311–332, 1991.

C. Meneveau and K. R. Sreenivasan. The multifractal nature of turbulent energy dissipation. *J. Fluid Mech.*, 224:429–484, 1991.

O. Métais and J. R. Herring. Numerical simulations of freely evolving turbulence in stably stratified fluids. *J. Fluid Mech.*, 202:117, 1989.

M. M. Metzger and J. C. Klewicki. A comparative study of near-wall turbulence in high and low Reynolds number boundary layers. *Phys. Fluids*, 13(3):692–701, 2001.

Patrice Meunier, Peter J. Diamessis, and Geoffrey R. Spedding. Self-preservation in stratified momentum wakes. *Phys. Fluids*, 18(10), 2006.

P. L. Miller and P. E. Dimotakis. Stochastic geometric-properties of scalar interfaces in turbulent jets. *Phys. Fluids*, 3(1):168–177, 1991.

A. S. Monin and A. M. Yaglom. *Statistical Fluid Mechanics: Mechanics of Turbulence–Volume 2*. M.I.T. Press, Cambridge, 1975.

A. Muschinski. Local and global statistics of clear-air Doppler radar signals. *Radio Sci.*, 39:RS1008, 2004.

A. Muschinski, R. G. Frehlich, and B. B. Balsley. Small-scale and large-scale intermittency in the nocturnal boundary layer and the residual layer. *J. Fluid Mech.*, 515:319–351, 2004.

G. D. Nastrom and K. S. Gage. A climatology of atmospheric wavenumber spectra of wind and temperature observed by commercial aircraft. *J. Atmos. Sci.*, 42:950–960, 1985.

E. A. Novikov and R. W. Stewart. The intermittency of turbulence and the spectrum of energy dissipation. *Izv., Akad. Nauk. SSSR, Ser. Geoffiz*, 3:408–413, 1964.

A. M. Obukhov. Spectral energy distribution in a turbulent flow. *Dokl. Akad. Nauk. SSSR*, 32:22–24, 1941a.

A. M. Obukhov. Spectral energy distribution in a turbulent flow. *Izv. Akad. Nauk. SSSR, Ser. Geogr. i. Geofiz*, 5:453–466, 1941b.

A. M. Obukhov. Some specific features of atmospheric turbulence. *J. Fluid Mech.*, 13:77–81, 1962.

S. A. Orszag and G. S. Patterson. Numerical simulation of turbulence. In M. Rosenblatt and C. Van Atta, editors, *Statistical Models and Turbulence*, volume 12 of *Lecture Notes in Physics*, pages 127–147. Springer, New York, 1972.

M. R. Overholt and S. B. Pope. A deterministic forcing scheme for direct numerical simulations of turbulence. *Comput. Fluids*, 27:11–28, 1998.

R. V. Ozmidov. On the turbulent exchange in a stable stratified ocean. *Izv. Atmospheric and Oceanic Physics*, 1:493–497, 1965.

R. L. Panton. *Incompressible Flow*. John Wiley & Sons, New York, 1984.

H. T. Pham and S. Sarkar. Transport and mixing of density in a continuously stratified shear layer. *J. Turbulence*, 11(24):1–23, 2010.

S. B. Pope. *Turbulent Flows*. Cambridge University Press, Cambridge, 2000.

S. B. Pope and Y. L. Chen. The velocity-dissipation probability density-function model for turbulent flows. *Phys. Fluids*, 2(8):1437–1449, 1990.

A. Praskovsky and S. Oncley. Comprehensive measurements of the intermittency exponent in high Reynolds number turbulent flows. *Fluid Dyn. Res.*, 21(5):331–358, 1997.

O. Praud, A. M. Fincham, and J. Sommeria. Decaying grid turbulence in a strongly stratified fluid. *J. Fluid Mech.*, 522:1–33, 2005.

K. J. Rao and S. M. de Bruyn Kops. A mathematical framework for forcing turbulence applied to horizontally homogeneous stratified flow. *Phys. Fluids*, 23:065110, 2011. doi:10.1063/1.3599704.

L. F. Richardson. *Weather Prediction by Numerical Process*. Cambridge University Press, 1922.

J. J. Riley and S. M. de Bruyn Kops. Dynamics of turbulence strongly influenced by buoyancy. *Phys. of Fluids*, 15(7):2047–2059, 2003a.

J. J. Riley and S. M. de Bruyn Kops. Dynamics of turbulence strongly influenced by buoyancy. *Phys. Fluids*, 15(7):2047–2059, 2003b.

J. J. Riley and M. -P. Lelong. Fluid motions in the presence of strong stable stratification. *Annu. Rev. Fluid Mech.*, 32:613–657, 2000.

J. J. Riley and E. Lindborg. Stratified turbulence: A possible interpretation of some geophysical turbulence measurements. *J. Atmos. Sci.*, 65(7):2416–2424, 2008.

J. J. Riley and R. W. Metcalfe. Direct numerical simulations of the turbulent wake of an axisymmetric body. In J-C. Andre, J. Cousteix, F. Durst, B. Launder, F. Schmidt, and J. Whitelaw, editors, *Turbulent Shear Flows 2*, page 78. Springer, 1980.

J. J. Riley, R. W. Metcalfe, and M. A. Weissman. Direct numerical simulations of homogeneous turbulence in density stratified flows. In B. J. West, editor, *Proc. AIP Conf. Nonlinear Properties of Internal Waves*, pages 79–112. American Institute of Physics, New York, 1981.

S. G. Saddoughi and S. V. Veeravalli. Local isotropy in turbulence boundary layers at high Reynolds number. *J. Fluid Mech.*, 268:333–372, 1994.

P. G. Saffman. *Vortex Dynamics*. Cambridge University Press, Cambridge, 1992.

D. Schertzer, S. Lovejoy, F. Schmitt, Y. Chigirinskaya, and D. Marsan. Multifractal cascade dynamics and turbulent intermittency. *Fractals*, 5(3):427–471, 1997.

J. Schumacher. Sub-Kolmogorov-scale fluctuations in fluid turbulence. *Europhys. Lett*, 80(5):54001, 2007.

J. Schumacher, K. R. Sreenivasan, and P. K. Yeung. Very fine structures in scalar mixing. *J. Fluid Mech.*, 531:113–122, 2005.

J. Schumacher, K. R. Sreenivasan, and V. Yakhot. Asymptotic exponents from low-Reynolds-number flows. *New J. Phys.*, 9:89, 2007.

Z. S. She, E. Jackson, and S. A. Orszag. Intermittent vortex structures in homogeneous isotropic turbulence. *Nature*, 344:226–228, 1990.

X. Shen and Z. Warhaft. Longitudinal and transverse structure functions in sheared and unsheared wind-tunnel turbulence. *Phys. Fluids*, 14(1):370–381, 2002.

E. D. Siggia. Numerical study of small-scale intermittency in three-dimensional turbulence. *J. Fluid Mech.*, 107:375–406, 1981a.

E. D. Siggia. Invariants for the one-point vorticity and strain rate correlation functions. *Phys. Fluids*, 24:1934–1936, 1981b.

W. D. Smyth and J. N. Moum. Length scales of turbulence in stably stratified mixing layers. *Phys. Fluids*, 12:1327–1342, 2000.

G. R. Spedding. Vertical structure in stratified wakes at high initial Froude number. *J. Fluid Mech.*, 454:71, 2002.

G. R. Spedding, F. K. Browand, and A. M. Fincham. The long-time evolution of the initially-turbulent wake of a sphere in a stable stratification. *Dyn. Atmos. Ocean.*, 23:171–182, 1996a.

G. R. Spedding, F. K. Browand, and A. M. Fincham. Turbulence, similarity scaling and vortex geometry in the wake of a towed sphere in a stably stratified fluid. *J. Fluid Mech.*, 314:53, 1996b.

E. A. Spiegel and G. Veronis. On the Boussinesq approximation for a compressible fluid. *Astrophys J.*, 131:442–447, 1960.

K. R. Sreenivasan. On the universality of the Kolmogorov constant. *Phys. Fluids*, 7: 2778–84, 1995.

K. R. Sreenivasan. Fluid turbulence. *Rev. Mod. Phys.*, 71:383–395, 1999.

K. R. Sreenivasan and R. A. Antonia. The phenomenology of small-scale turbulence. *Annu. Rev. Fluid Mech.*, 29:435–472, 1997.

K. R. Sreenivasan and P. Kailasnath. An update on the intermittency exponent in turbulence. *Phys. Fluids*, 5:512, 1993.

G. Stolovitzky and K. R. Sreenivasan. Kolmogorov refined similarity hypotheses for turbulence and general stochastic-processes. *Rev. Mod. Phys.*, 66(1):229–240, 1994.

G. Stolovitzky, P. Kailasnath, and K. R. Sreenivasan. Kolmogorov refined similarity hypotheses. *Phys. Rev. Lett.*, 69(8):1178–1181, 1992.

R. B. Stull. *An introduction to boundary layer meteorology.* Kluwer Academic Publishers, 1988.

S. Sykora. K-space images of n-dimensional spheres and generalized sinc functions. *Stan's Library Volume II*, April 2007. DOI:10.3247/SL2Math07.002.

G. I. Taylor. Statistical theory of turbulence. *P. Roy. Soc. Lond. A. Mat.*, A 151: 421–478, 1935.

G. I. Taylor. The spectrum of turbulence. *P. Roy. Soc. Lond. A. Mat.*, 1938.

H. Tennekes. Eulerian and Lagrangian time microscales in isotropic turbulence. *J. Fluid Mech.*, 67:561–567, 1975.

H. Tennekes and J. L. Lumley. *A First Course in Turbulence.* MIT Press, Cambridge, 1972.

S. T. Thoroddsen. Reevaluation of the experimental support for the Kolmogorov refined similarity hypothesis. *Phys. Fluids*, 7(4):691–693, 1995.

F. Toschi, G. Amati, S. Succi, R. Benzi, and R. Piva. Intermittency and structure functions in channel flow turbulence. *Phys. Rev. E*, 82(25):5044–5047, 1999.

R. R. Trieling and G. J. F. van Heijst. Decay of monopolar vortices in a stratified fluid. *Fluid Dyn. Res.*, 23:735, 1998.

Yu-heng Tseng and J. H. Ferziger. Mixing and available potential energy in stratified flows. *Phys. Fluids*, 13(5):1281–1293, 2001.

A. Tsinober, P. Vedula, and P. K. Teung. Random Taylor hypothesis and the behavior of local convective accelerations in isotropic turbulence. *Phys. Fluids*, 13:1974–1984, 2001.

S. I. Vainshtein. Dissipation field asymmetry and intermittency in fully developed turbulence. *Phys. Rev. E*, 61(5):5228–5240, 2000.

L. Vervisch and T. Poinsot. Direct numerical simulation of non-premixed turbulent flames. *Annu. Rev. Fluid Mech.*, 30:655–691, 1998.

J. M. Vindel, C. Yague, and J. M. Redondo. Structure function analysis and intermittency in the atmospheric boundary layer. *Nonlinear Process Geophys.*, 15(6): 915–929, 2008.

S. I. Voropayev, Y. D. Afanasyev, and I. A. Filippov. Horizontal jet and vortex dipoles in a stratified medium. *J. Fluid Mech.*, 227:543, 1991.

S. I. Voropayev, D. L. Boyer Z. Zhang, H. J. S. Fernando, and C. W. Pok. Horizontal jets in a rotating stratified fluid. *Phys. Fluid.*, 9:115, 1997.

S. I. Voropayev, S. A. Smirnov, and A. Brandt. Dipolar eddies in a stratified shear flow. *Phys. Fluids*, 13:3820, 2001.

L. Waite, M. Stratified turbulence at the buoyancy scale. *Phys. Fluids*, 23(6):066602, JUN 2011. ISSN 1070-6631. doi: 10.1063/1.3599699.

M. Waite and P. Bartello. Stratified turbulence dominated by vortical motion. *J. Fluid Mech.*, 517:281–308, 2004.

M. L. Waite and P. Bartello. Stratified turbulence generated by internal gravity waves. *J. Fluid Mech.*, 546:313–339, 2006.

M. Wan, S. Oughton, S. Servidio, and W. H. Matthaeus. On the accuracy of simulations of turbulence. *Phys. Plasmas*, 17(8):082308, 2010.

L. P. Wang, S. Y. Chen, J. G. Brasseur, and J. C. Wyngaard. Examination of hypotheses in the Kolmogorov refined turbulence theory through high-resolution simulations. Part 1. Velocity field. *J. Fluid Mech.*, 309:113–156, 1996.

Z. Warhaft. Passive scalar in turbulent flows. *Annu. Rev. Fluid Mech.*, 32:203–240, 2000.

T. Watanabe and T. Gotoh. Inertial-range intermittency and accuracy of direct numerical simulation for turbulence and passive scalar turbulence. *J. Fluid Mech.*, 590:117–146, 2007.

J. C. Wyngaard. Atmospheric turbulence. *Annu. Rev. Fluid Mech.*, 24:205–233, 1992.

J. C. Wyngaard, N. Seaman, S. J. Kimmel, M. Otte, X. Di, and K. E. Gilbert. Concepts, observations, and simulation of refractive index turbulence in the lower atmosphere. *Radio Sci.*, 36(4):643–669, 2001.

V. Yakhot. Probability densities in strong turbulence. *Physica D*, 215(2):166–174, 2006.

V. Yakhot and K. R. Sreenivasan. Anomalous scaling of structure functions and dynamic constraints on turbulence simulations. *J. Stat. Phys.*, 121:823–841, 2005.

P. K. Yeung and S. B. Pope. Lagrangian statistics from direct numerical simulations of isotropic turbulence. *J. Fluid Mech.*, 207:531–586, 1989.

P. K. Yeung, D. A. Donzis, and K. R. Sreenivasan. High-Reynolds-number simulation of turbulent mixing. *Phys. Fluids*, 17:081703, 2005.

P. K. Yeung, S. B. Pope, A. G. Lamorgese, and D. A. Donzis. Acceleration and dissipation statistics of numerically simulated isotropic turbulence. *Phys. Fluids*, 18:1–14, 2006a.

P. K. Yeung, S. B. Pope, and B. L. Sawford. Reynolds number dependence of Lagrangian statistics in large numerical simulations of isotropic turbulence. *J. Turbulence*, 7:1–12, 2006b.

K. Yoshimatsu, N. Okamoto, K. Schneider, Y. Kaneda, and M. Farge. Intermittency and scale-dependent statistics in fully developed turbulence. *Phys. Rev. E*, 79(2, Part 2), 2009.

T. Zhou and R. A. Antonia. Approximations for turbulent energy and temperature variance dissipation rates in grid turbulence. *Phys. Fluids*, 12(2):335–344, 2000a.

T. Zhou and R. A. Antonia. Reynolds number dependence of the small-scale structure of grid turbulence. *J. Fluid Mech.*, 406:81–107, 2000b.

T. Zhou, Z. Hao, L. P. Chua, and Y. Zhou. Comparisons between different approximations to energy dissipation rate in a self-preserving far wake. *Phys. Rev. E*, 74 (5, Part 2):056308, 2006.